FARUSIL NAJEEB MULLAVEETTIL

ADDITIVE MANUFACTURING AND EXPERIMENTAL RESEARCH OF POLYVINYLIDENE FLUORIDE CELLULAR STRUCTURES AND TRANSDUCERS

DOCTORAL DISSERTATION

Kaunas
2021

KAUNAS UNIVERSITY OF TECHNOLOGY

FARUSIL NAJEEB MULLAVEETTIL

ADDITIVE MANUFACTURING AND EXPERIMENTAL RESEARCH OF POLYVINYLIDENE FLUORIDE CELLULAR STRUCTURES AND TRANSDUCERS

Doctoral Dissertation
Technological Sciences, Mechanical Engineering (T 009)

Kaunas, 2021

This doctoral dissertation was prepared at Kaunas University of Technology, Institute of Mechatronics during the period of 2016–2021. The studies were supported by the Research Council of Lithuania.

Scientific Supervisor:

Dr. Rolanas DAUKŠEVIČIUS, (Kaunas University of Technology, Technological Sciences, Mechanical Engineering, T 009).

Doctoral dissertation has been published in:
http://ktu.edu

Editor:

Kornelija Šalnaitė

KAUNO TECHNOLOGIJOS UNIVERSITETAS

FARUSIL NAJEEB MULLAVEETTIL

POLIVINILIDENFLUORIDO GARDELINIŲ KONSTRUKCIJŲ BEI KEITIKLIŲ ADITYVI GAMYBA IR EKSPERIMENTINIAI TYRIMAI

Daktaro disertacija
Technologiniai mokslai, mechanikos inžinerija (T 009)

Kaunas, 2021

Disertacija rengta 2016–2021 metais Kauno technologijos universiteto Mechatronikos institute. Mokslinius tyrimus rėmė Lietuvos mokslo taryba.

Mokslinis vadovas:

Dr. Rolanas DAUKŠEVIČIUS (Kauno technologijos universitetas, technologiniai mokslai, mechanikos inžinerija, T 009).

Interneto svetainės, kurioje skelbiama disertacija, adresas:
http://ktu.edu

Redagavo:

Kornelija Šalnaitė

CONTENTS

NOMENCLATURE

ABS – Acrylonitrile butadiene styrene
AM – Additive manufacturing
AMF – AM File
ASTM – American Standard for Testing and Materials
CAD – Computer-aided design
CTE – Coefficient of thermal expansion
DE – Deferential evolution
DLP – Digital light processing
EBM – Electron beam melting process
EPO – European Patent Office
FDM – Fused deposition modelling
FFF – Fused filament fabrication
FLM – Fused layer manufacturing
FTIR – Fourier-transform infrared spectroscopy
ISO – International Organization of Standards
LOM – Laminated object manufacturing
ME – Modelling extrusion
PA – Polyamide
PC – Polycarbonate
PC – Polycarbonate
PEEK – Polyether ether ketone
PEI – Polyetherimide
PI – Polyimide
PLA – Polylactic acid
PPS – Polyphenylene sulfide
PSU – Polysulfone
PTFE – Polytetrafluoroethylene
PVDF – Polyvinylidene fluoride or Polyvinylidene difluoride
PVDF-C – PVDF-co-hexafluoropropylene (PVDF-HFP copolymer)
PVDF-C-ESD – Graphene-filled PVDF-HFP composite
PVDF-H – PVDF homopolymer
SLA – Stereolithography
SLS – Selective laser sintering
STL – Stereo Lithography Language (file format)
TPMS – Triply periodic minimal surface
XRD – X-ray diffraction analysis

LIST OF FIGURES

LIST OF TABLES

INTRODUCTION

Research relevance, aim and objectives

Additive manufacturing (AM) is one of the transformational technologies within Industry 4.0, enabling cost-effective rapid fabrication of highly customizable products in smaller batches with better use of resources and lower waste. Advancements in AM gradually transform the processes of design, manufacturing, and maintenance of mechanical parts [1–4]. Specifically, extrusion-based AM (3D printing) has drawn more interest from industrial and research communities because it is more affordable and versatile in comparison to other AM methods. New printable materials, including speciality and high-performance polymers, are continuously entering the 3D printing market to cater for more specialized product uses. Therefore, it is important to optimize printability and evaluate the mechanical performance of printed parts under relevant load conditions in order to ensure their durability, particularly in the case of higher value-added functional components used in aerospace, automotive, biomedical, and healthcare fields [5]. Fused filament fabrication (FFF) is among the most widespread 3D printing technologies [6] which is used for the rapid fabrication of prototypes and functional parts using various thermoplastic polymers and composites [7]. However, FFF often comes with printability issues, particularly when using common open-chamber 3D printers (i.e. not industrial-grade printers with heated chambers). This makes it difficult to achieve print quality with acceptable consistency (similar to injection moulding or other well-established technology), especially in the case of semi-crystalline polymers that are prone to geometric distortions.

3D printability and mechanical properties of a well-known commodity or engineering thermoplastics (e.g. ABS, PLA, PETG, PA) are extensively covered in the scientific literature [8]. However, they are not always suitable for more functionally demanding exploitation cases, e.g. in specific biomedical applications or in harsher chemical or thermal conditions that are common in (bio)chemical, aerospace, automotive or electronics industries. Such applications often require the use of lightweight parts, including load-bearing structures made of speciality or high-performance thermoplastics (e.g. PEI, PEEK, PSU, PPS, fluoropolymers). Apart from Teflon™, polyvinylidene fluoride (PVDF) is a very well-known fluoropolymer with a special set of properties, e.g. it is highly resistant to many chemicals and UV, flame retardant with low permeability to most fluids and gases, sterilizable, potentially biocompatible and delivers adequate strength in a broader temperature range (up to ~150°C). In addition, PVDF may be processed to have piezoelectric properties, which means that it is a promising material to enable 3D printing of flexible multi-functional structures with integrated mechanical sensing or energy harvesting as well as biocompatible piezoelectric structures relevant for advanced biomedical devices, such as electro-stimulating bioscaffolds, smart prostheses, orthoses or implants. In real service conditions, such 3D printed smart devices may experience not only uniaxial tension or compression but also may be acted by bending loads, hence it is important to determine strength characteristics under different deformation modes.

PVDF-based FFF filaments were commercially introduced only several years ago, hence it is relevant to dedicate research efforts to PVDF printing, mechanical characterization and FFF application for rapid fabrication of piezoelectric devices. In particular, there are few research reports regarding problematic printability of semi-crystalline and hydrophobic PVDF in open-chamber FFF machines, regarding mechanical properties of lightweight PVDF parts with standard and novel cellular internal fillings (lattice infills) subjected to diverse loading regimes, and regarding FFF adaptations for printing conventional thin-layered and bioinspired cellular 3D piezoelectric transducers with and without electrical poling.

The aim of this research is to determine the mechanical properties of 3D printed lightweight PVDF structures with cellular infills and experimentally verify a technological concept of printable thin-layered and bioinspired 3D piezopolymeric transducers. In order to achieve the aim, the following objectives are addressed:

1. To analyse and identify relevant research questions regarding PVDF printability, mechanical properties and the possibility to adapt FFF technology for fabrication of piezopolymeric transducers.
2. To determine suitable FFF process conditions and parameters for obtaining complete prints with PVDF homopolymer, PVDF-HFP copolymer, and PVDF-HFP/graphene composite filaments.
3. To create CAD models and calibrate slicing parameters for successful 3D printing of test specimens, designed with standard infill patterns (strut-based lattices) and bioinspired patterns with sheet-based lattice topologies of triply periodic minimal surfaces (TPMS).
4. To perform a comprehensive characterization of tensile, compressive and flexural properties of printed PVDF homopolymer, copolymer and graphene-based composite lightweight structures with cellular infills and establish dependences of strength-elastic characteristics on infill density, pattern type and layer orientation.
5. To verify experimentally the feasibility of FFF-based poling-assisted and poling-free rapid prototyping of biocompatible piezopolymeric transducers, designed as conventional 2D structures (thin films) or bioinspired cellular TPMS 3D structures (scaffolds) and to perform piezoelectric measurements.

Research methods

Theoretical and experimental analysis methods have been applied in the study. CAD work, 3D printability and investigation of various characterizations were assessed using techniques of experimental mechanics. Employed software tools included SolidWorks for the design of various PVDF samples and test specimens, Ultimaker Cura and Simplify3D – for performing print slicing procedures and Tinius Olsen software Horizon – for the force and deformation data acquisition and postprocessing during mechanical testing in tension, compression, and three-point bending regimes. The latter was performed using Tinius Olsen H25KT double-column

universal testing machine with video extensometer VEM 300. In addition, cyclic testing machine Instron E10000 was used for periodic mechanical loading of printed 2D and 3D PVDF samples during piezoelectric measurements by using PICO USB oscilloscope and a transimpedance amplifier circuit, which was custom designed at the Institute of Mechatronics. A high-voltage power supply Spellman SL100P600 was used for the electrical poling of printed PVDF samples. Dimensional deviations of the printed samples were evaluated using coordinate measuring machine Mitutoyo CRYSTA-Apex S 9106.

The research work was conducted in various labs of KTU Institute of Mechatronics and Faculty of Mechanical Engineering and Design.

Scientific novelty

1. Effective FFF process parameters suitable for affordable open-chamber 3D printers which enable sufficiently consistent rapid prototyping of biocompatible PVDF-HFP copolymer and static-dissipative PVDF-HFP/graphene composite parts with acceptable levels of geometric distortions.
2. Experimentally established relationships that reveal the influence of strut-based and bioinspired sheet-based lightweight infills on strength and elastic performance under three main mechanical loading regimes for three recently introduced PVDF-based filaments with specialized functional characteristics (biocompatibility, static build-up prevention, etc.) that are relevant for high-tech industrial applications.
3. FFF-based technological concept for poling-free rapid prototyping of bioinspired cellular piezopolymeric 3D structures (piezoelectric TPMS scaffolds) using biocompatible PVDF-HFP copolymer filament.

Defended statements

1. The use of lower extrusion speed and wider brims in open-chamber 3D printers increase the chances of fabricating less distorted complete prints with PVDF homopolymer, PVDF-HFP copolymer, and PVDF-HFP/graphene composite parts.
2. The determined tension-compression strength asymmetry in the 3D printed PVDF-based specimens is larger compared to the conventional (non-printed) solid thermoplastics but the asymmetry decreases with lower infill density.
3. The proposed poling-free FFF printing of biocompatible and bioinspired TPMS scaffold structures with PVDF-HFP is a feasible concept for rapid prototyping of geometrically complex piezo polymeric 3D transducers that exhibit comparatively weak but practically usable direct piezo-effect.

Practical value

1. The implemented ISO standards-based mechanical testing methodology is suitable for evaluating the mechanical properties of various lightweight 3D printed cellular structures subjected to different mechanical loading regimes.
2. The reported recommendations for effective PVDF printing are useful for more successful additive manufacturing of other difficult-to-print thermoplastics, especially semi-crystalline and hydrophobic as PVDF.
3. The measured comprehensive strength and elastic characteristics of PVDF-based materials printed with various infill densities and patterns serve as design guidelines for the FFF community dealing with 3D printing of lightweight cellular parts designed for different loading regimes and harsh operating conditions requiring the use of such fluoropolymers as PVDF.
4. The proposed concept of poling-free 3D printing of piezopolymeric 3D transducers can be potentially applied for rapid prototyping of high-flexibility lead-free pressure or deformation sensors or mechanical energy harvesters, or for printing electro-stimulatory bioscaffolds in bone tissue engineering applications or for other biomedical devices that require in-vitro noncytotoxic materials such as PVDF-HFP used in this research work.

Research approbation

Research results were reported in: 2 articles of international journals with Impact Factor indexed in the Web of Science database, 2 articles in peer-reviewed conference proceedings and 1 abstract of an international conference. The results were presented at 3 international conferences: International Conference on 3D Printing Technologies and Materials (ICPTM) 2020 (Amsterdam, the Netherlands), Mechanika 2018 (Kaunas, Lithuania) and Mechanika 2017 (Kaunas, Lithuania).

The research was partly funded by the Research Council of Lithuania via the project “3D-printable flexible electroactive transducers for soft mechatronics systems (FLEXYMECH-3DP)” (contract No. S-MIP-17-89).

Structure of the dissertation

The doctoral thesis contains the introduction, 3 chapters, general conclusions, a list of literature sources featuring 228 references and a list of the author’s scientific publications. The doctoral thesis is composed of 100 pages, 66 figures, and 2 tables.

1. LITERATURE REVIEW

In recent times, low cost and less time-consuming AM techniques have been developed that could achieve high printing characteristics. Polymer products are printed with a broader range of properties and the innovations are constantly changing depending on how goods are produced and manufactured and how consumers use them [1, 9–11]. AM general benefits include the elimination of tooling costs. Manufacturing of single parts or small batches is feasible and cost-effective, has lower waste of materials and use less energy, which means amore "green" production, increasing the versatility of production, decreasing lead time, higher design freedom, and potential optimization of the performance of the pieces. As AM significantly reduces the complexity of prototype manufacturing, innovators can easily define prototypes of their ideas. In practice, designing and manufacturing techniques have reduced its time consumption to a few hours [12]. AM reduces the cost of production and increases the manufacturing industries efficiency [13]. Furthermore, AM offers solutions with shorter production time and limited batch sizes where complex designs are required [14], ranging its application from the aerospace industry to the medical one. According to [15], AM techniques were implemented to design useful devices for astronauts in the International Space Station.

In 2018, more than 4,000 applications of a patent for innovations relating to AM were recorded at the European Patent Office (EPO), which indicates that progress in AM has increased in recent years (Fig. 1). AM patent applications have increased by an average of 36%, which is more than the EPO's average annual growth of patent applications in the same timeframe. The largest share of AM patent applications so far accounts for modern industrial applications of AM technologies.

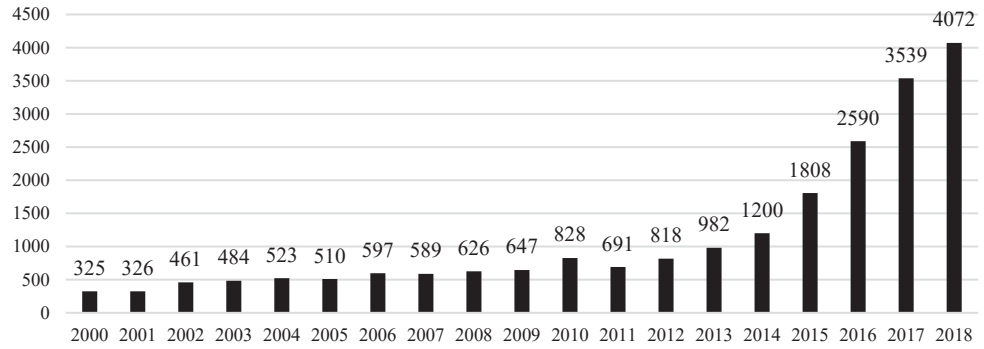

Fig. 1. Patent applications in AM technologies from 2000-2018 [16]

Global demand in 2020 amounted to over $12.8 billion for AM systems, printing products, components (Fig. 2), software, and services. Even though the pandemic impacted the growth of AM industry, global investment on AM projected a yearly expansion rate of 7.5%, to sales of $12.8 billion in 2020. Established producers of AM systems showed a decline in sales whereas multiple start-ups and less established manufactures grew in sales by 7.1% resulting in almost $5.3 billion in 2020 [17].

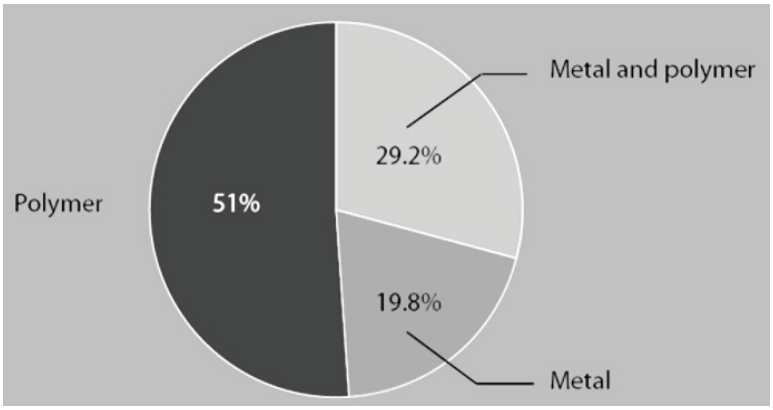

Fig. 2. Components produced by AM industry [18]

1.1. Additive Manufacturing

The word '3D-printing' has become part of the routine language nowadays and is also known to individuals outside the industry and research community. However, when referring to a number of different technologies, the same word '3D-printing' is used. It would also be helpful to incorporate the nomenclature adopted by the ASTM and ISO committee and to use the word 'additive manufacturing' to include all of these technologies. Specifically, ISO/ASTM 52900 coins AM as the 'process of joining materials to make parts from 3D model data, usually layer upon layer, as opposed to subtractive manufacturing and formative manufacturing methodologies' [19]. AM constructs the piece, usually layer by layer, using powders or liquid, as opposed to milling or cutting a portion from a block of material, and in the case of polymers, filament form is the most widely used [20]. In addition, AM generates much less waste as compared to subtractive manufacturing [21]. According to the standard, seven groups have been categorized into AM processes: vat photo polymerization, material extrusion, powder bed fusion, sheet lamination, binder jetting, directed energy deposition, and material jetting [22–24]. Generally, the process is initiated with the creation of a 3D computer-aided design (CAD) model. The created design is then generated into a Stereo Lithography Language (STL) form. Manufacturers of printers usually have software created by them which are compatible to slice the model into individual layers in the STL file. The printer executes the generated file and begins depositing heated filament one layer (2D) on top of the other, eventually forming a 3D model in the process and the printed part is then subjected to desired post-processing for achieving the targeted application. Depending upon the component complexity and efficiency, various AM techniques, like stereolithography (SLA), digital light processing (DLP), selective laser sintering (SLS), laminated object manufacturing (LOM), Polyjet technology and fused filament fabrication (FFF) are being used.

1.2. Fused Filament Fabrication

Fused Filament Fabrication (FFF), also referred to as Fused deposition modelling (FDM), Modelling extrusion (ME), Fused Layer Manufacturing (FLM) or 3D printing, is an AM technique based on extrusion (Fig. 3), where the material is selectively dispensed through a nozzle or orifice [19]. FFF is currently used not only for the development of prototypes but also for the production of usable parts in the aerospace industry, such as drilling grids [25]. It lowers the cost of assembly, able to form complex design and versatile functional parts, generated through an STL file, that generates 2D layers on a heated platform. Researchers are progressing in creating new materials used in FFF components in diverse fields like biomedical, aerospace and several other industries. Nonetheless, various drawbacks such as low accuracy, uneven surface, low mechanical properties, and the role of the FFF process is limited in manufacturing functional components. Some prototypes do not require high accuracy, therefore, the low accuracy is relative for certain applications.

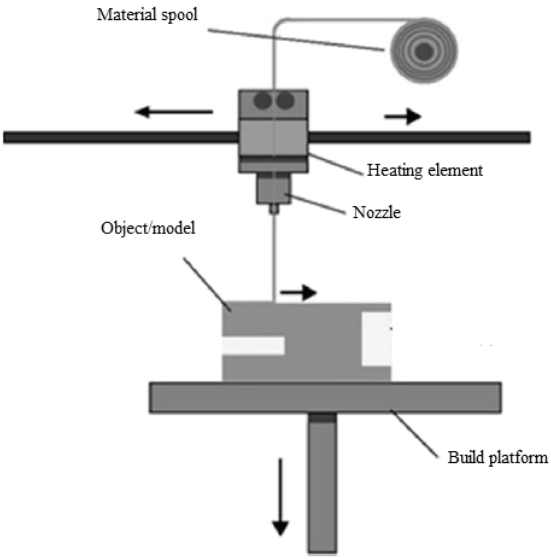

Fig. 3. FFF printing process [26]

FFF is considered as one of the stable AM technologies and is widely used in office and home environments by thousands of groups worldwide to build personalized and low-cost 3D printers that are useful. Since the early 2000s, the most widely used AM technique worldwide has been FFF. For FFF to be considered as a suitable candidate in the industry for mass production of printed materials, efficiency and robustness of the components is fundamental condition that is being pursued. Therefore, it is vital to manufacture parts aiming for stable qualities for satisfying unique conditions and specifications that could lead to an increase in the influence of the market share of FFF parts. There are many parameters of the FFF mechanism that could have a direct effect on the designed parts. These parameters influence the

bonding within the layers and between the layers that have been deposited. The mechanism of fusion in the FFF process depends on the solidification time. Initially, fibres merge with each other during the molten state leading to a strong bond between fibres. Immediate freezing of the fibre in the molten stage may lead to fusion with other fibres earlier in solidification. This produces voids between the fibres and the bonds thus produced would not show mechanical properties that are similar to a traditional. The implementation of the FFF is increasing day by day as a production method but due to the discontinuous nature of the process, one of the greatest tasks in the production of FFF parts as a final application is to forecast the mechanical behaviour of the parts [27]. A component with the desired characteristics could be developed by choosing optimal process parameter combinations and the desired thermoplastic polymer considering the mechanical characteristics, for the proposed application of the component plays a vital role [28]. To achieve desirable properties of components, many researchers studied different controllable parameters [29–33] and further works have been focused on process parameter optimization [34, 35]. Multiple studies are aimed at process parameter optimization for maximizing the quality of a single component. Rayegani experimented with a Deferential Evolution (DE) approach to maximize tensile strength [36]. In addition, a more sophisticated approach is to consider and simultaneously optimize the characteristics of two or more components to achieve a set of optimum parameter combinations [37].

Every 3D printer has components designed on the precept that a computerized model is converted into a physical 3D model by stacking layer on layer of material. A digital model is created using distinct software, such as CATIA, SOLIDWORKS. The models are either generated by modelling software or by 3D scanner-generated data. The modelling platform generates the prototype into slices of 100 or 1000 layers until the object is done, one over the other (Fig. 4.). The created objects could be of various geometry and are generated from a computerized model, 3D model or other sources, such as an AM File (AMF) electronic data source. A variety of processes for 3D printing produce complicated parts and among these, FFF printers are commonly utilized due to numerous advantages. The software for the 3D printer is used to model, slice and direct the machines to production. There are various slicing software types based on complexity levels, like CURA, Slic3r, Blender, Free CAD, 3D slash, Simplify3D and so on [38].

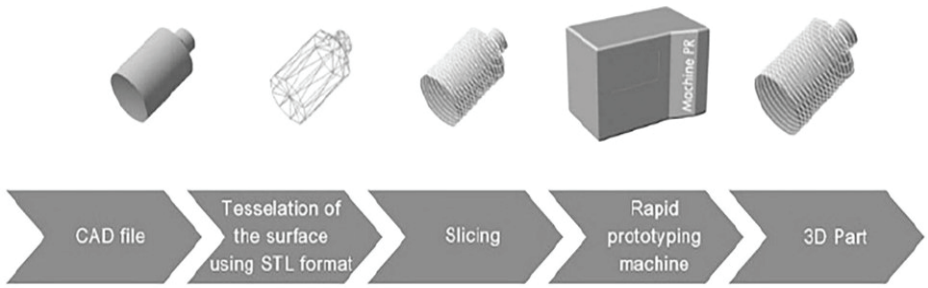

Fig. 4. Additive manufacturing process steps [39]

CURA is very imperative, sharp, robust and efficient for converting designs into 3D printing instructions or codes for ULTIMAKER 2+. Different research teams use different FFF printers for their research purposes. The following is description of commonly used FFF machines by different research groups: Fortus FFF 400 mc machine [36], Fortus 360 mc machine [40], FFF 200 mc machine [41], FFF 1650 machine [42], FFF Vantage machine [43], Ultimaker 2 [44], Prusa, MakerBot Replicator 2 [45], MEM-300 machine [46], Raise3D N2plus machine [47], Makerbot Replicator 2X [25], Julia 3D printer [48], FFF Maxum Machine [49], Prodigy Plus, WitBox desktop 3D printer [50], and HP Design jet 3D CQ656A [32].

The above list depicts widely used FFF printers. Each FFF machine has its perks and drawbacks. Every consumer can have a varied choice of equipment, depending on the printing parameters that could be controlled and altered. The benefits and drawbacks of each FFF machine are therefore not the aim of this research and are not further discussed in this work.

1.2.1. FFF Process Parameters

Multiple process domains in the FFF technique have a major effect on output, efficiency, and component functionality. Build orientation specifies the orientation of specimens, i.e. if the specimens are aligned vertically, horizontally, or laterally (X, Y, Z axes). The Layer height or thickness represents the height along the Z-axis of the deposited materials (Fig. 5), which is usually an FFF machines vertical axis. It is usually maintained lower to the extruder nozzle diameter. The distance between the adjoining raster tool paths in the same layer is defined as air gap and the width and orientation of these rasters determine the processing time and amount of material that will be required. The outer layer, which is often referred to as the shell or wall layer, describes the width of the path that encapsulates the infill layers. The amount of these shell layers improves the perimeter stability. The Nozzle diameter calculates the among of materials extruded from the 3D printer. It conducts the thermal energy supplied to the filament by the heating cartridge and blocks and melts it. The inner diameter of the nozzle impacts the volume of extruded plastic per second. Generally, nozzle diameters vary from 0.1 mm up to 1.0 mm. This offers the user of a 3D printer a great deal of versatility. The widely used nozzle diameters are 0.8 mm, 0.6 mm, 0.4 mm, and 0.25 mm. These nozzles are manufactured by different materials, like brass (max temp 300°C), stainless steel (500°C), and hardened steel (500°C), which widely depends upon the type of material being printed [51]. The amount of time required to print a part depends on the speed set for the print layers, which is defined as the distance per unit time travelled along the XY plane by the extruder. The print time confides on the printing speed, which is measured in mm/s. The outer layer of the 3D printed parts is solid and the structure internally, usually referred to as infill layers, is the inner portion hidden by the external layers or the shell layer and has shapes, sizes, and distinct patterns. Various infill patterns are utilized to build a robust internal structure. The most commonly used patterns are triangles, cubic, octet, honeycomb, zigzag. The extrusion temperature depends on all the parameters defined so far and it is understood as the heating of the material during the printing process.

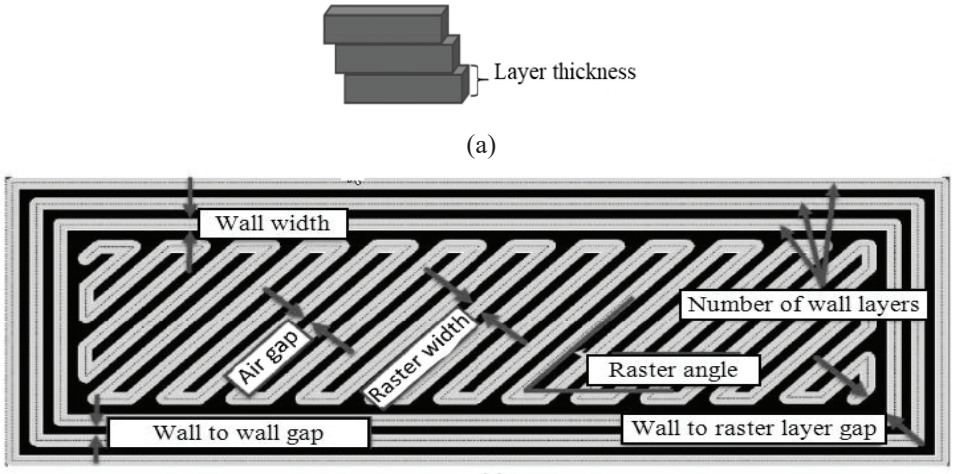

Fig. 5. (a) Layer thickness [52] (b) Slicing parameters [53]

1.2.2. FFF Materials

The most common polymers used in FFF are acrylonitrile butadiene styrene (ABS) and polylactic acid (PLA) [8] as well as polycarbonate (PC) and nylons. Reports on the mechanical properties of these polymers are widely available [6, 26, 54]. ABS is used in application that requires high impact resistance and toughness [55]. PLA, being a biodegradable thermoplastic, which requires less energy and processing temperature, is widely used for high-quality prototypes and usable components. The majority of the printers favours PLA as it does not require a heated platform [56]. PC thermoplastics are used for applications that are oriented towards high toughness, strength and durability. They are translucent in appearance and have good surface quality. Polyether ether ketone (PEEK) has shown recently to be an excellent candidate for heat resistant and chemical stable applications. PEEK is a biomaterial that is being widely used in bone repair by forming prosthetics. Polyetherimide (PI) is used widely in the transportation industry due to low pollution formation. PI demands higher bed and extrusion temperatures and they are used in aircraft cabins due to low-density features. Nylons are printed for applications that aim for flexible and durable parts. Nylons tend to warp while printing as it retains hygroscopic properties [57]. Strict and/or complex conditions from various demanding industries, such as chemical manufacturing, automotive, biomedical, oil and gas, aerospace, electronics, etc., are not generally complied with by the most common printable polymers (e.g. ABS, PLA, PC, PET). Specifically, PLA, PCL, PGA, PE, PUs, PEEK [58], and PEI [54] are the most commonly studied polymers in the biomedical field. Due to the demand for complex and more advanced bioengineering applications, high-performance fluoropolymers have recently started to be incorporated into the AM sector [59].

1.3. Polyvinylidene Fluoride

In many applications, polymers that retain electroactivity are used in smart material applications [60]. These polymers show ferroelectric, pyroelectric or piezoelectric behaviour. The most stable electroactive properties, large frequency response characteristics, high electromechanical coupling, etc. are shown by PVDF and its copolymers that are chemically stable fluoropolymers formed by the polymerization of vinylidene difluoride. At present, the production of PVDF depends on pressing the polymer into sheets and then stretching them in the vicinity of a strong electric field. Under straining condition, the polymer molecules are aligned and convert the PVDF to a polarized phase. For the production of PVDF, different fabrication methods have been recognized and implemented, like electrospinning, cryogenic ball spinning, and AM [61]. PVDF material is characterized by multiple distinctive properties and is also known as a biocompatible material that has exceptional resistance to corrosive acids [62]. PVDF is a toxic substance that has high thermal and hydrolytic stability, and under UV radiation indicates strong immunity to/insensitivity to degradation [63]. In addition, PVDF is considered among rare piezoelectric polymers when structured in the suitable semi-crystalline process to establish a sufficiently major piezoelectric effect for use in the processes of sensing [64], actuation [65] and applications for energy collection[66]. PVDF's glass transition is about -37°C as a thermoplastic material and a melting point is 179°C [67].

Due to the electronegativity of fluorine atoms relative to those of hydrogen and carbon atoms, for PVDF monomer the strong electric dipole moment is correlated with many of the interesting properties of PVDF. The dipole moment perpendicular to the polymer chain is present in each chain. The monomer units are then packaged in a morphology that can reveal an overall dipolar contribution per unit cell [68]. PVDF show excellent resistance to creep and fatigue, and resistance to nuclear radiation and low coefficient of friction. PVDF resins are chemically resistant to a wide range of chemicals. At ambient temperatures, PVDF homopolymers are resistant to chemicals with a pH value up to 12 and copolymers are generally resistant to chemicals with a pH up to 13.5 [69]. PVDF also shows high mechanical strength at elevated temperature range (-50°C to 150°C) and excellent thermal and dimensional stability. Low permeability to most gases and fluids makes PVDF a favourable candidate as insulation cover in chemical applications [59].

There are very diverse applications of PVDF-based polymers, including structural components suitable for harsh conditions (e.g. coatings, pipes, liners, cables, fittings, etc.) [59], porous filtration and separation membranes [63]; biomedical devices such as surgical sutures and meshes, catheters, syringes, biocontainment vessels, drug reservoirs, vascular prostheses, cochlear implants, etc. [69]; electroactive bio-scaffolds in tissue engineering [70, 71], piezoelectric sensing, energy harvesting and actuation [72, 73], microfluidics [74], electrically conductive [75] or insulating [76] layers, energy storage [77, 78], structural energetics [79], etc. New technology for the manufacture of piezoelectric PVDF (sheet stretching with poling, electrospinning, etc. [73]) primarily enables structures to be manufactured in 1D (fibres) or 2D only (thin films). AM of PVDF-based polymers and composites has

recently been attracting growing research efforts through FFF [80–82], direct-write [83] and stereolithographic [84] methods. They are motivated by the prospect of continuous production of free-form lead-free piezoelectric structures with large electroactive areas or volumes, involving advanced functionality in smart bioscaffolds, such as multi-directional mechanical energy harvesting, tracking, actuation or electrical stimulation. To customize dielectric, mechanical, tribological, thermal or processability properties, 3D printing of PVDF-based composites is also studied [85, 86].

1.3.1. Piezoelectricity of Polyvinylidene Fluoride

In 1969, Dr Heiji Kawai first discovered the piezoelectric activity of PVDF [87] and since the discovery, PVDF has been seen in application in optics [88], vibration control [89], sensing [90], energy harvesting [91], space use[92], and other exploitations [93]. At present, commercial processing of PVDF is based on compressing sheets of the polymer, then stretching the sheets as the material cools with the use of a strong electric field. When a piezoelectric polymer is exposed to physical loading, positive and negative charges are formed on the surface of the substance. The direct piezoelectric effect is defined as the capacity of a material to transform the mechanical form of energy to an electrical form of energy. Conversely, under an applied electric field, a piezoelectric polymer can deform. The opposite piezoelectric effect, therefore, is the material's ability to transform the electrical form of energy into the mechanical form of energy. The piezoelectric effect is often applied for sensors and the converse effect is utilized in actuator applications.

Several techniques are used to promote the β-phase in PVDF [94], for example, stretching (uniaxial/biaxial), usage of a high electric field, annealing (thermal), and mechanical rolling. Currently, the transformation of α -phase into β-phase in PVDF thin films is done by stretching of a formed PVDF in solid-state. However, the introduction of lattice defects during the tension process is very simple, degrading the product quality [95]. Polarization at high temperature and quenching prepare the β-phase [96] by regulating the annealing temperature. The temperature range, however, may be a limiting factor where the generation of higher β-phase is prevented either by high or too low temperature. For the complex preparation process, for converting into the β-phase, traditional methods are implemented, and for the manufacture of PVDF, materials usually include some post-production steps, like onward sewing or manual components assembling.

3D printing employs a versatile way of letting various designs to be printed and it could create ideal shapes and patterned objects. In addition, the preparation stage can be easily performed in a multi-physical field that could promote chemical changes and phase changes during material preparation, leading the way for the easy development of high-β-phase and complex geometry PVDF. Tarbuttona et al. [97] revealed the possibility to produce electroactive PVDF by an adapted FFF printer. Their work investigates the phase change while printing and using FTIR and DSC measurements. The findings prove an ultimate phase change while printing and indicated that the α phase of the PVDF was essentially altered whereas the FTIR

results did not demonstrate a considerable change during the dominant electroactive beta phase. The printed poled PVDF demonstrated piezoelectric behaviour, highlighting the possible application of the adapted printing method to create sensors.

1.3.2. Polyvinylidene Fluoride Poling

The method of reorienting the crystallites (molecular dipoles) by the implementation of an electric field at higher temperatures in the polymer bulk medium is poling. The poled specimen is lowered down in temperature in the vicinity of the electric field to maintain the orientation condition of the molecular dipoles. The two methods widely used in poling polymers are electrode poling and corona poling [98]. Conductive electrodes are located on both sides of the polymer during electrode poling and high voltage is applied through the sample [92] (Fig. 6). A breakdown of polymer molecules [60] can be caused by the presence of a strong electric field. The magnitude and uniformity degree of the temperature applied and the contamination degree or voids at the electrode and the polymer surface are dependent on the strength and duration of the electrical field applied and the magnitude and uniformity degree of temperature applied to the polymer. The consistency of the crystalline alignment increases during the stretching (mechanical) of the polymer during the poling process [99] for polymers, such as PVDF.

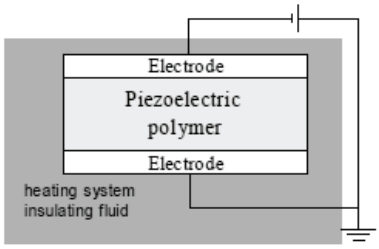

Fig. 6. Schematic of the electrode poling system [92]

An electrode is positioned on one side of the polymer film in the corona poling process [92] (Fig. 7). A high-voltage conductive needle is positioned in a dry air or argon medium on a much lower DC voltage grid that is on top of the polymer. The molecules of gas near the tip are elevated and ionized towards the piezoelectric polymer surface. A number of charges gathered on the polymer surface depend on the location of the grid and the voltage applied which will regulate the electrical field applied across the polymer. In all cases found in the literature [100], the appropriate temperature in the two methods is set up to 300°C. The benefits of corona poling are that film imperfections are more susceptible, do not require electrodes, and a wider region of the samples can be exposed to poling. The downside is that setup and optimization is significantly more complex than the direct electrode technique [92].

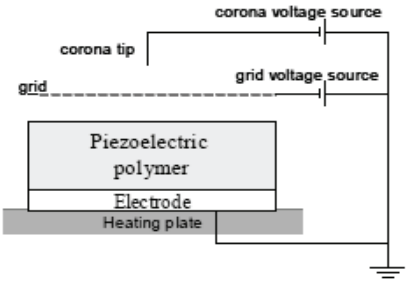

Fig. 7. Schematic of the corona poling system [92]

Relevant parameters in the poling phase are the magnitude of the electrical field and temperature. The more the electric field is applied, the more the polarization is induced, provided that the normal thumb law is maintained, i.e. the field of poling is greater than the coercive field of the material [101]. Poling at elevated temperature enhances the moveableness of the dipole and thus leading to an increase in the polarizability of the material. The shift of volume during the dipole orientation causes warpage of the films and the polymer relaxation during poling can help reduce warpage at elevated temperatures and could lead to conforming to the poled volume. The average ideal poling temperatures are between 85°C and 130°C [102, 103].

1.4. Mechanical Properties

The mechanical properties of the FFF component are different from the mechanical properties of the filament due to various printing parameters (e.g. the temperature of printing and height of layer). The effect of process parameters on mechanical properties has been explored in several research efforts. Tension, flexural and compression strengths are the widely researched mechanical properties of 3D printed parts [54].

1.4.1. Tensile Properties

The tensile test parts were developed in most of the research according to the ASTM D638 standard and ISO 527 of the International standard organization. This standard is used for measuring the tensile properties of thermoplastics. The specimens from the test were dumbbell-shaped.

Various printing parameters (width of raster, temperature of extrusion, and orientation of raster) were investigated by Montero et al. [104] and their experiment was planned according to fractional factorial design. Using a Stratasys FFF 1650 printer, the printed specimens were formed using ABS material. The experimental results showed that two major parameters for tensile strength were the air gap and raster orientation, and for optimum tensile strength, a negative air gap and 0° raster orientation were preferred. Wang et al. [105] also evaluated the effect on tensile strength of different parameters and found that the most critical specification influencing the tensile strength is the orientation in the upward direction (Z-Axis). The effect of the orientation of the raster and its influence on the tensile strength in

ABS parts was investigated by Fatimatuzahraa et al. [106]. The results depict that for the cross (0°/90°) and crisscross (45°/-45°) orientations, tensile strength was optimum and almost the same.

Croccolo et al. [107] evaluated the strength in the tensile regime based on the number of shells and found that the strength increased with the increase in the number of shells. Nidagundi et al. [48] evaluated the influence on the ultimate strength by layer thickness, construct orientation, and orientation of raster while evaluating roughness of surface and accuracy of dimensions. For the evaluation of these 3 parameters, the Taguchi orthogonal array method was chosen for determining the iteration of experimental runs. The Taguchi method is a method of process/product optimization focused on 8 stages of preparation, performing, and analyzing experiment results to determine the best levels of control factors. The most critical parameter that influences the strength property in the tensile testing is the build orientation, according to Torres et al. [108] who evaluated the effect of temperature of extrusion, speed of printing, orientation of raster, density of infill, layer thickness, and perimeter (number of shells).

The influence of the orientation of the part, the thickness of the layer and the speed of print under the tension loading is investigated by Chacon et al. [109]. The results indicated that at an upright built orientation (90°), tensile strength was marginal and is almost similar to the other two construction orientations (on-edge and flat). Furthermore, the layer thickness and speed of the print depends on the orientation of the construction. Layer thickness, the orientation of a part (60°), and raster orientation (-45°/45°) are critical for the investigation of tensile strength and defining an optimal combination of process parameters for analysing the tensile properties is vital. The optimum levels of important parameters differ based on the material used [110].

Cross-sectional area of the printed sample, the amount of infill density set and the number of shell layers implemented has a direct impact on the tensile strength of the ABS components, according to Mahmood et al. [111]. The property is observed to be proportional to the density of infill and number of shells. It was, however, inversely proportional to the cross-sectional area. The effect of density of infill and the pattern in the infill, on the tensile regime when printed with ABS/ZnO were determined by Aw et al. [112]. Their analysis showed that tensile strength was maximized by 100% infill density, even when printed with line patterns. Kung et al. [113] showed, close to Mahmood et al. [111], that the cross-sectional area and the number of shells are important for the tensile regime. In addition, they observed that at -45°/45° raster orientation, tensile strength was the highest.

Compared to other part features, especially tensile strength, the orientation of the part was observed to be the most important printing parameter from established research and the strength was higher at 0° orientation as the path of extrusion is in line with the applied load. The thickness of the layer depends on factors, such as part orientation, and at 0° orientation it is optimum. For a better tensile regime, low layer thickness could be recommended. It is fair to infer from current studies that at high density on infill and higher number of shells, tensile strength is maximum. Interlayer bonds become effective at high density. For tensile strength, elevated temperature of

extrusion is preferable as the filament fluidity increases at a high temperature and the bond between the interlayer becomes stronger. The ideal orientation of raster is still not conclusive and it could be inferred that the raster orientation of 0°/90° or -45°/45° is the most favourable [114].

1.4.2. Compression Properties

Nearly all papers complied with the ASTM 695 and ISO 604 standards for rigid thermoplastics for the compressive test. The commonly used designs that are implemented in the FFF process from this standard are as follows: (1) right cylinder with a diameter of 12.7 mm and a height of 25.4 mm or (2) rectangular prism with a dimension of 25.4 mm, 12.7 mm, and 12.7 mm. The loading speed for compressive property testing is within the 1.3 ± 0.3 mm/min range [28].

Implementing the FFF method, the ABS tissue engineering scaffold structure was constructed and analysed as well as the impact of various process parameters. The two relevant compression strength parameters were air gap and raster distance. The lower air gap and higher distance of raster tend to show excellent compression properties [42]. Hernandez et al. studied, along with other mechanical properties, the significance of construct orientation for optimizing compressive properties. The parts were manufactured using the uPrint SE Plus 3D with ABS P430 material. Experiments concluded that the compressive strength, yield strength, and modulus were increased by 0° build orientation. Moreover, compressive strength was found to be lower at 45° [115]. Zaman et al. developed components aiming for application in the aerospace industry. The study was focused on determining the influence of the thickness of layer, pattern and density of the infill for the compressive regime. In the paper, following the Taguchi orthogonal array (L8), the experimental study was planned and specimens were generated by a Makerbot Replicator2X from PLA and PETG. The results of the experiment and statistical analysis (ANOVA and S/N ratio) showed that the compressive strength of parts constructed by PETG was marginally higher than that of parts constructed by PLA [25].

The works performed in determining the effects of the compressive regime in FFF is minimum and various combination of process parameters has been used in various studies. Further research is required to form a conclusion as to the effect of process parameters or parameter combinations on the compressive regime. Moreover, it can initially be inferred from established research that a high number of layer thickness enhances compressive regime. Furthermore, compression strength and the orientation of the part are vital as they influence the anisotropic properties of FFF components. It is also safe to infer from experimental findings that high density of infill, patterns of infill, and a high amount of shell layers are preferred to improve the compression regime of the printed pieces [114].

1.4.3. Flexural Properties

For checking the flexural properties of thermoplastics, ASTM D790 and ISO 178 are the widely used international standards. Usually, a 3-point bending device is used for analysing the flexural regime. The load is applied to the sample, making the

sample act as a beam supported by it. The current research on the determination of the effects of FFF printing parameters on the flexural regime is outlined in this section. Panda et al. evaluated the effect of thickness of the layer, orientation of the part, raster distance and raster orientation on flexural strength. The observation from their statistical analysis was that all parameters played a vital role in influencing the flexural strength, as well as the various combinations of parameters [116]. Fatimatuzahraa et al. investigated the ideal orientation of raster in flexural regime with ABS parts, printing with 4 different orientations. It was found that at a 45°/-45° raster orientation, the flexural strength was maximum [106].

The parameters that maximize the flexural regime of ABS components, such as the orientation of the part and orientation or raster, was investigated by Durgun et al. Their finding was that surface roughness and flexural strength were maximized at 0° orientation of part and raster [30]. Moreover, according to Lužanin et al., the interaction between build orientation and density of infill seemed to be important for flexural regime, based on the experimental results and statistical analysis [117].

Wu et al. printed PEEK and ABS filaments and contrasted bending properties with compression and tensile properties. The experimental results showed that flexural properties for both materials were almost identical and the tensile and compression results showed varied differences [118]. Chacon et al. investigated the influence of quantitative parameters, like the thickness of layer and print velocity, and a categorical variable, like the orientation of the part on flexural strength. For flexural strength, for each build orientation, they built a quadratic model. At on-edge orientation, the strength at flexural regime was found to be higher and optimum thickness of layer and print velocity depended on part orientation [50].

Compared to tensile and compression strength, flexural strength is the least evaluated property. It could be inferred that the relation between printing parameters and the flexural regime is more complex when compared to compression and tensile regime. This is because a part undergoes tensile and compressive loading during flexural testing. At 0° orientation of the part, flexural strength is maximum as the orientation is perpendicular to the direction of the loading in this built orientation. Multiple research is needed in understanding the effect of various printing parameters and their combinations on the flexural regime, including the thickness of the layer, the orientation of part and raster, print velocity, and air gap [114].

1.5. Infill Analysis

The FFF technology enables users to monitor the density of models by means of infill parameters [119]. The use of a variety of infill densities to minimize printing time and material consumption is very common in the manufacture of parts using FFF printing technologies [120]. A substantial number of documented research works has tried to analyse FFF printing-related parameters by varying infill densities. Sood et al. [121] analysed the effects of density of infill on the mechanical properties of printed ABS parts. Their results indicate that the influence of infill density affects the tensile regime of the formed parts. Nunez et al. analysed dimensional accuracy and surface properties of ABS structures. They report that it is evident that the density of the infill

influences the surface properties and dimensional stability of the parts. The results indicate that the higher density and the higher surface finish and improve the dimensional accuracy [122]. Baich et al. studied the influence of infill properties and time in printing on the mechanical behaviour of the printed parts from ABS. The lower the amount of material used i.e.; Low infill density leads to low cost but this would result in deteriorated mechanical properties. Moreover, infill properties are directly related to the time of printing [123]. The strength of PLA samples was tested by printing with 4 distinct patterns by Harpool et al. with density set at 15% and the hexagonal pattern reported the maximum strength, whereas at 100% infill density the solid pattern resulted in behaving close to a brittle material [124]. Works initiated by Cristian and Dudescu observed the variation of infill density (20%–100%) in FFF printing. The findings indicated that an increase in modulus of elasticity increase in infill density [125]. Variations in the density of infill could lead to changes in the meso and macro structures of 3D printed parts [126].

Tanveer et al. calculated the impact strength of the PLA sample at 3 different infill densities (50%, 70%, and 100%) and found the impact force to be proportional to the density of the infill. The research predicted that the variations in impact resistance were observed due to the variations in material packing density in the component, thereby reducing the stress strength factor. The impact resistance of the FFF structures depends greatly on the alignment of the mesostructure. In each element, the mesostructure is a function of the density and the pattern of infills, and the geometry can control the crack propagation and the stress strength factor in terms of impact loading which in turn affect the component's impact power [127]. The combined effect of various patterns and densities on the impact strength of printed PLA was investigated by Mishra et al. Their investigation concluded that the energy absorption is maximum when infill density is set at 85% for each pattern [128]. Gopsill et al. analysed samples with honeycomb patterns under multiple loading conditions using FEA and for complex goods, this technique is useful for achieving the maximum strength with the ideal density of infill [129].

1.6. Infill Pattern

The investigation of stronger and lighter materials is one of the main objectives in materials development. These materials have gained their desirability in many industries, ranging from automobile to aerospace. The properties of cellular structures have been investigated by many researchers to attain this goal of lighter and stronger materials. The properties by mass or volume unit or specific properties are more desirable of cellular structures than the bulk materials. The path of deposition of layers is a crucial factor in FFF printing. The filling pattern criterion shows the way the deposition is performed in the print. The pattern intends to produce a strong, durable, reliable structure inside the part. It is possible to use different filling patterns from the slicing software, each with advantages and trade-offs with printing time [125]. Some of the most common patterns used are grid, triangles, lines, cubic, Hilbert curve, honeycomb, Archimedean chords, octagram spiral, cross, concentric, octet, rectilinear [130]. For this study, the patterns were chosen based on their intended applications.

Lines, zigzag patterns for models and figurines, standard 3D printing patterns, like triangles, functional 3D prints, like cubic, octet and flexible 3D prints, like concentric and cross are used in this study. The mechanical strength of the printed parts depends on the pattern orientation and heat distribution, keeping other conditions unchanged. Higher mechanical strength is obtained when the loading and pattern formation are in the same direction. If the direction of the print or pattern direction is assumed the main factor for the mechanical strength, the pattern in the form of straight lines or line pattern expects to report maximum tensile strength. If the relation in the aspect ratio of the geometry is assumed as the main factor, the highest tensile strength would be reported by concentric pattern. If thermal background were the main factor in consideration, at the layers, the pattern with the shorter deposition length or with lower layer printing time would show the highest resistance [130].

Line pattern

Printing parallel lines form the pattern line by alternating the direction to perpendicular as the layer progresses (Fig. 8). This is one of the most commonly used patterns in different printers. Since the distance between the print layers is small, these types of patterns portray a smooth surface. The components printed with this pattern showed low strength in the Z-direction as the connection between the layers is minute. From the literature, Line patterns are the most printed pattern in FFF printing [131]. This pattern tends to print without many complications and is predicted to show higher strength. This pattern is highly researched for print orientation influence on mechanical strength [53].

(a) (b)

Fig. 8. 3D printed structure of line pattern: (a) illustrative, (b) actual

Cubic pattern

To date, various works were done with cubic pattern structures. A cubic pattern is a stack of tilted cubes that are placed adjacent to each other (Fig. 9). A number of studies have been conducted connecting cubic patterns and AM. A study was presented that dealt with properties of different metals and alloys which were fabricated with a selective laser melting technique [132]. There are multiple works reported in the formation of cubic structures through the Electron beam melting process (EBM). Zhang Lai-Chang et al. [133] conducted a review on titanium allows that are additively manufactured by EBM. The titanium was formed into different porous structures, like cubic, diamond, rhombic, honeycomb and its mechanical,

fatigue and corrosion resistance properties were analysed. Similar works have been done in the formation of titanium alloys with cubic lattice structures through the same EBM manufacturing technique where the compression response, effect of heat treatments above and below β transition temperature on microstructure were investigated [134]. For the application in biomedical implants, cubic porous titanium alloys were printed using the EBM technique and the mechanical study was performed to find the modulus of elasticity and stress shielding effect for bone density variation [135]. Additionally, in the field of prostheses, a study was done in analyzing the surface to volume and strength to stiffness ratios of different lattice structures [136]. Murr Lawrence E published their work on cubic lattice structure formed through EBM for lightweight applications and also commented on the process optimization issues [137]. Furthermore, titanium polymer was manufactured by AM technique through an efficient design structure with periodic cubic and octet geometries for the development of solar water disinfection devices. The author demonstrated that the AM technique could be used to create efficient, cost-effective, and safe household water disinfectant devices [138]. Another study focused on testing curves of cubic cellular structure for pillow brackets and studied its mechanical properties [139].

The primary motive for using voided structures is to consume less material and time for production. Vaidya Rohan and Sam Anand presented an approach to reduce the support structures by using cellular structures for generating optimized support structures [140]. The cubic structure was also used in other AM processes, like ink-extrusion [141], powder feed [142], bed-based [143], subtractive hybrid manufacturing [144], Binder jetting [145], and selective laser melting [146]. Liverani Erica et al. [147] conducted tensile and compression tests on cubic lattice structures formed by the SLM process and observed significant differences in the strength and stiffness between different unit cells. Shiva S et al. [148] investigated the transformation in phase and mechanical properties of cubic shape memory alloy structure formed by laser AM.

(a) (b)

Fig. 9. 3D printed structure of cubic pattern: (a) illustrative, (b) actual

Octet pattern

The octet pattern in 3D printing is categorized under functional print part designs, where higher strength in several directions is required. It is a combination of regular tetrahedra and cubes, along with multiple lines aligned adjacent to each other (Fig. 10). These adjacent lines result in the formation of strong internal frames where

the load is dissipated instantly. These patterns also showed a less pillowing effect. Octet pattern was used to print gear parts using PLA, ABS, and PETG material by FFF technique [149]. K.I Giannakopoulos et al. stated a nonlinear behaviour in PLA octet pattern when subjected to mechanical loading and showed lower stiffness to honeycomb structure [150]. In the field of tissue engineering, scaffolds can be fabricated using FFF printing. Ali Bagheri et al. used an octet pattern for porous prosthesis implants and determined its modulus of elasticity [151].

(a) (b)

Fig. 10. 3D printed structure of octet pattern: (a) illustrative; (b) actual

Cross pattern

The cross infill gives a space-filling curve that looks like crosses along the volume (Fig. 11). This pattern is chosen for printing soft and flexible parts. Since there are no straight lines in the X or Y direction, these patterns tend to be weaker in all horizontal directions. They have no strong spots and produces no retractions, therefore, these patterns would be ideal for flexible filaments. There is very limited literature available for FFF printed cross patterns. Horvath Anca Simona et al. performed an analysis on infill influences on tensile strength where the cross pattern was used along with other widely used patterns [152]. Cross pattern is considered to be similar to other flexible patterns, like the Hilbert curve, which is widely used [130].

(a) (b)

Fig. 11. 3D printed structure of cross pattern: (a) illustrative, (b) actual

Zigzag pattern

The pattern Zigzag causes the print head to produce lines in a zigzag fashion (Fig. 12) and the pattern show resemblance to normal lines pattern. The print lines are connected in a single long line which results in an uninterrupted flow. This is one of the most common patterns used in FFF printing for various applications. Emma

Polonio Alcala et al. 3D printed PLA zigzag scaffolds for breast cancer stem cells enrichment [153].

(a) (b)

Fig. 12. 3D printed structure of zigzag pattern: (a) illustrative; (b) actual

Concentric pattern

With the concentric pattern, rings parallel to the shell/wall is created (Fig. 13). This pattern is used in applications where higher strength is required due to the formation of non-intersecting lines in its lattice. With the formation of concentric rings, this pattern could be used for flexible prints with uniform strength in horizontal directions. A. Tsouknidas et al. used a concentric pattern to study the impact absorption capacity in FFF printed components [154] and Wanvisa Talataisong et al. FFF printed PETG concentric preform hollow core for Mid-infrared optical fibres [155]. Concentric patterns can also be seen used in 3D printing of bioinspired structures with metal reinforced thermoplastic stretchable elastomers where an inexpensive 3D printer is developed for printing bioinspired joint systems with dissimilar materials [156].

(a) (b)

Fig. 13. 3D printed structure of concentric pattern: (a) illustrative, (b) actual

Triangle pattern

The triangles pattern forms a group of lines that are aligned in three different directions forming a triangle-shaped lattice (Fig. 14). These patterns show uniform strength in all horizontal directions. K Vigneshwaran and N Venkateshwaran performed a statistical analysis of mechanical properties of wood-PLA composites with triangle pattern varying layer height and infill densities [157]. It is observed that the triangle pattern is used in topology optimization for improved buckling load [158].

Sumair F Sunny used a triangle pattern to mimic the nature of compressive failure related to macro-structure and loading direction in FFF with Nylon polymer [159].

(a) (b)

Fig. 14. 3D printed structure of triangle pattern: (a) illustrative, (b) actual

1.7. Triply Periodic Minimal Surfaces

The integration of AM and biomedical scaffolds led to the investigation into 3D printing of bioinspired structures based on triply periodic minimal surface (TPMS). TPMS was first mentioned in literature in 1865 by a German mathematician Schwarz by introducing diamond and primitive surfaces. A century later, Alan H. Schoen discovered a gyroid surface that was widely investigated in-depth for its topology dependent properties in various fields [160]. Minimal surfaces are local area-minimizing. The smallest unit implies the smallest area possible for a surface covering the borders of that unit. Porous TPMS architectures are built by iterative elements with the lowest unit cells area possible. TPMS is characterized by implicit functions that could be differentiated even at the junction of struts by curved surfaces. It is possible to express each sort of TPMS architecture in a strict mathematical equation [161, 162]. These surfaces have zero mean curvature, which means the sum of the principal curvatures at each point is zero. In particular, a crystalline structure with minimal surfaces is fascinating as these structures repeat themselves in three dimensions leading to triply periodic. TPMS geometries (Fig. 15) are bound by a strict mathematical equation which could be altered to control the properties of the structures [163, 164]:

$$\textit{Gyroid}: \cos(x)\sin(y) + \cos(y)\sin(z) + \cos(z)\sin(x) + a \tag{1}$$

$$\textit{Schwartz Diamond}: \sin(x)\sin(y)\sin(z) + \sin(x)\cos(y)\cos(z) + \cos(E)\sin(y)\cos(z) + \cos(x)\cos(y)\sin(z) + a \tag{2}$$

$$\textit{Schwartz Primitive}: \cos x + \cos y + \cos z + a \tag{3}$$

The cartesian coordinates are x, y and z [165] and the variant *a* is the offset value that determines the configured solid fraction [166]. If the offset value is positive, the layer builds in a positive region (upwards) and vice versa [167].

Fig. 15. Illustrative TPMS patterns

Mathmod software was developed for structural analysis of TPMS and provides support for manipulation and visualization in multiple dimensions of various TPMS models by a mathematical equation. This software application has been implemented in recent years and the design of models has attracted wide interest. Initially, Mathmod was used to produce the unit cells of TPMS models. It is possible to import studies and the created models could be exported into various platforms [168–170].

The mechanical properties of TPMS have been studied in previous studies [166, 171], in which the fabrication techniques SLS, SLM, and EBM have been used in building metallic TPMS structures. Such AM approaches resolve the challenges of traditional development and processes, enabling dynamic open-cellular manufacturing. The porous structures of TPMS have great bio-mimicking characteristics and outstanding mechanical properties that boost the feasibility and the durability of implants. TPMS geometries portray excellent biomorphic characteristics with continuous smooth surfaces The surfaces share the pattern/design/frame into two disjoint areas. In relation to the straight edges or sharp turns of geometrically primitive forms, for instance, cubes and cylinders, TPMS structures can ensure stronger biomorphic structures for activities of cells, like cell attachment, penetration, proliferation, and migration [172, 173]. Moreover, because of the curvature of the struts, TPMS structures exhibit good fatigue properties as stress concentrations induced by defects were removed at the nodal points [168, 174, 175]. A TMPS structure has greater manufacturing capacity during the manufacturing process than a geometry with sharp turns or straight-edged pores and struts, avoiding the problem of thermal alteration due to long overhangs [176].

According to the reported deformation mechanism of TPMS, Schwarz primitive surface is dominated by stretching and Gyroid, and diamond surfaces are bending dominated. The mechanical properties of stretching primitive structure and bending diamond structure were analysed and the results indicate that the stretching structure performed better under mechanical loading [177, 178].

TPMS are favourable porous structures that could be applied to fabricate polyfunctional materials for a wide range of technological applications [163]. Recently, studies have been reported on electrical and thermal conductivity, thermal expansion coefficient and mechanical properties of TPMS structures. Due to the interconnectivity and continuity phases of TPMS-IPCs, they show higher and robust properties compared to other types of composites, according to Abueidda et al. [179].

Moreover, elastic moduli, anisotropy of conductivity and elasticity of TPMS composites were also investigated. Further investigation was also done in strength, ductile properties and energy dissipation of TPMS geometries [180]. TPMS has also been reported to originate novel cellular materials with diverse relative densities (ratio between TPMS and solid base densities) [181, 182].

The gyroid structure is the most common TPMS structure for biomedical applications [183, 184]. It could be observed experimentally. The gyroid architecture in tissue engineering is ideal for biomorphic scaffold construction [162]. Extensive research on the study of the mechanical properties of open-cellular gyroid structures has recently been performed. The mechanical properties of skeletal-TPMS and porous sheet TPMS were investigated by Ketan et al. and concluded that higher mechanical behaviour regarding stress and strain response is reported by sheet-TPMS structures. In contrast to skeletal gyroid structures, sheet-based gyroid structures often show a comparatively greater modulus of elasticity, peak stress, and resilience [185].

In terms of rate of porosity, modulus of elasticity, permeability property, and compression loading, TPMS aligns to the behaviour of natural bones, making TPMS an excellent choice for scaffolds in orthopaedics [186]. In theory, TPMS possess favourable geometry for cell proliferation [177]. Investigation on skeleton TPMS for orthopaedic scaffolds is very limited. Three types of TPMS for its mechanical properties, producibility, and bone ingrowth was studied and the research concluded that gyroid TPMS skeletal recorded the most flexible design space [187]. The Gyroid patterned surfaces show lower stress concentration effects within the structure and portray powerful mechanical properties. Shi et al. performed an FEA that showed the mechanical properties of TPMS simulated scaffolds were similar to the bone's properties [188]. TPMS fabricated at higher porosity reported Young's modulus close to that of cancellous bones and at lower porosity, Primitive and Diamond scaffolds showed modulus resembling cortical bones [189]. Scaffolds designed with primitive and diamond lattices with low porosity (5%–10%) indicated the same young's modulus as that of cortical bone [189]. The mechanical properties of Gyroid surfaces with porosities 50% and 75% was assessed by Castro et al. The results concluded that the gyroid surface was a compatible design for bone tissue engineering [190]. Reports on FFF printed TPMS structures are very few. Gyroid pattern was introduced to FFF slicing software in the last 2 years. However, gyroid was investigated using other AM techniques. 3D printed Ti-6Al-4V scaffolds were designed using Schwarz primitive lattices and was fabricated by SLM for investigating its mechanical properties [191]. In view of mechanical performance, periodic porous structures are found to be very promising.

1.8. Chapter Conclusions

This chapter presented a comprehensive review of recent publications related to the dissertation topic. The main findings of the review are as follows:

1. AM significantly reduced the complexity of prototype manufacturing including the elimination of tooling costs, cost-effective fabrication of single parts or small batches, lower waste of materials and less use of energy.
2. Build orientation, raster orientation, infill density and layer thickness are very widely analysed 3D printing parameters in terms of their influence on mechanical properties of the prints. The influence of infill pattern is investigated to a lesser extent. Well-known commodity and engineering thermoplastics (e.g. PLA, ABS, PC, PA) are very widely used and studied within FFF community. Published research work on specialty and high-performance thermoplastic prints is relatively scarce, especially in the case of fluoropolymers that are required in various functionally demanding cases such as aircrafts, automobiles, (bio)chemical components and biomedical devices (e.g. prostheses, orthoses, implants, bioscaffolds, etc.).
3. PVDF is a "newcomer" thermoplastic in FFF field and there are few published works dedicated to its printability and mechanical properties. Detailed studies on strength and elastic characteristics of lightweight load-bearing PVDF structures with varying infills are not available, especially as concerns mechanical properties under various deformation regimes such as tension, compression and bending.
4. Reports on mechanical properties of FFF printed bioinspired TPMS polymeric structures (e.g. scaffolds) are limited in comparison to the additively manufactured metal structures. Studies in compression regime predominate and there is obvious lack of research data on tensile and flexural properties for TPMS structures printed with specialty and high-performance thermoplastics such as PVDF. Gyroid, Schwarz Primitive and Schwarz Diamond are among the most widely investigated TPMS structures. Their smooth and highly porous topology with large specific area is very attractive for biomedical implants and scaffolds. TPMS lattices are also very relevant as lightweight infills for various durable load-bearing structures since smooth minimal surfaces have less stress concentrations.
5. Only several years ago scientists started research on adapting FFF process for fabrication of piezoelectric transducers, especially using pure PVDF or PVDF-HFP. Contact poling (applied after printing process) and corona poling (applied during printing process) are used to make piezopolymeric structures using FFF. Limited published works on 3D printed PVDF-based piezoelectric sensors or energy harvesters suggests that it is difficult to adapt the FFF process for fabricating PVDF having strong piezoelectric properties.

2. MATERIALS AND METHODS

FFF printing of PVDF is aggravated by complications associated with its larger thermal expansion coefficient and higher crystallinity degree (warping tendency) as well as low surface energy (low surface adhesion), leading to an accumulation of stress and causing part distortions. Therefore, different aspects of PVDF printing that were investigated are addressed in this study by means of a traditional semi-open FFF printer. Various FFF parameters have a dominating influence on the PVDF printed part characteristics and printing efficiencies. Extrusion temperature and build platform temperature, layer thickness, build orientation, printing speed, raster orientation, nozzle diameter, shell values, etc. are some of the most significant factors. Three commercially available PVDF-based filaments (∅ 2.85 mm) produced by Nile Polymers, Inc. were employed in this work: i) PVDF-H (Fluorinar-H™) based on Kynar® PVDF homopolymer, ii) PVDF-C (Fluorinar-C™) based on Kynar Flex® PVDF-HFP copolymer, iii) PVDF-C-ESD (Fluorinar-ESD™) based on graphene-filled Kynar Flex®. Copolymerizing PVDF with hexafluoropropylene (HFP) produces lower crystallinity degree [192], which makes printing easier and allows more versatile parts to be produced, including those with in vitro cytocompatibility (ISO-10993-5:2009 compliant for Fluorinar-C™). PVDF is less hygroscopic in contrast to PLA, ABS, and nylon [67]. To avoid moisture-induced filament degradation, PVDF filaments are dried for 60 minutes at 40°C before printing. Using the Ultimaker 2+ (Fig. 16) fitted with a 0.4 mm nozzle, test specimens were printed. The Ultimaker 2+ specifications and requirements of CURA software are mentioned in Table 1.

Table 1. Ultimaker 2+ specifications

External dimensions and weight	342 × 493 × 588 mm. Weight: 11.3 kg
Build volume	223 × 223 × 205 mm
OS supported	MacOS, Linux, windows
File types supported	STL, AMF
Operating ambient temperature	15 °C–32 °C
Transfer file	Standalone 3D printing from SD card
Output	24 V DC, 9.2 A
Input	100–240 V, 4A, 50–60 Hz

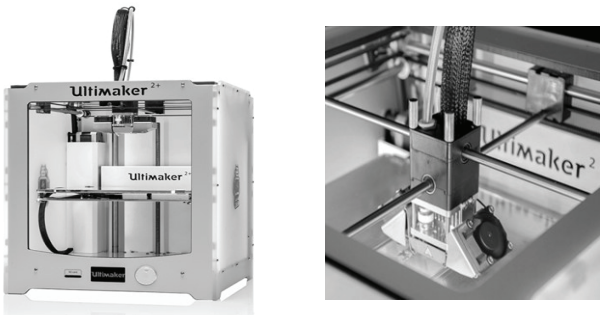

(a) (b)

Fig. 16. (a) Ultimaker FFF printer (b) extruder head unit

2.1. Quasi-static Mechanical Testing[1]

At present, there are no established standardized mechanical test methods that are specifically developed to FFF printed parts. Therefore, in the field of AM, mechanical tests are conducted using American Society for Testing and Materials (ASTM) or International Organization of Standards (ISO) standards that are applicable to conventionally processed plastics [193]. The most widely used standard include ASTM D638 for testing tensile properties, where dumbbell-shaped specimens are used to evaluate tensile and yield strength, Young's modulus, elongation at yield and at break [194]. The ISO developed ISO 527 for the characterization of plastics under tensile loading [195].

For determining the flexural properties, ASTM formulated D790 which calculates the flexural modulus and strength of plastics. The standard has two divisions: division A for materials that break at lower deflections and division B for larger deflections [196]. ISO 178 covers the procedure for determining the flexural strength and modulus for rigid and semi-rigid plastics [197]. ISO 604 is intended for compression testing of rigid plastics. Compressive strength, yield stress and modulus are determined by following this standard [198]. D695 is the corresponding test standard by ASTM [199].

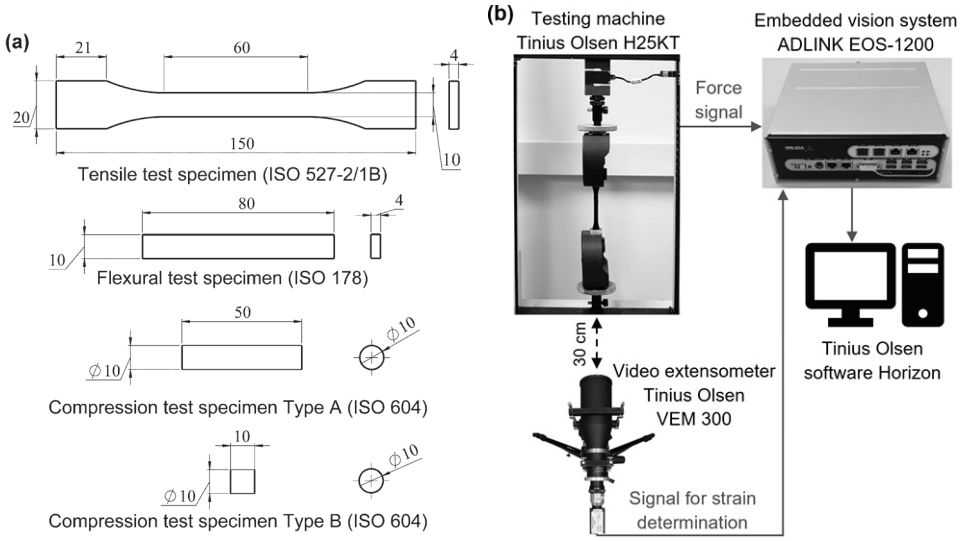

Fig. 17. (a) Geometry of test specimens, (b) the schematic diagram of the test setup [200] (Reproduced with permission from Springer Nature)

The tensile, flexural and compression tests in this work were carried out in compliance with ISO 527/2, ISO 178 and ISO 604 standards under quasi-static loading conditions, respectively. 5 samples were printed for each test case for derivation of mean values of elastic and strength characteristics. CAD models of the

[1] Material in this chapter was first published in [200] by Springer Nature

specimens were prepared in SolidWorks and then exported as STL files to the Ultimaker software Cura 3.6.0 for pre-processing, slicing, generation of G-codes and control of FFF process. Fig. 17(a) shows the dimensions and geometry of the specimens fabricated in Ultimaker 2+. Before testing all the specimens were subjected to control measurements of width and thickness.

The tests were conducted at room temperature employing the Tinius Olsen H25KT universal testing machine (Fig. 17(b)). The machine was equipped with 1 kN and 25 kN load cells during flexural and compressive/tensile tests, respectively. Strain values were measured by integrating the Tinius Olsen VEM 300 video extensometer, which comprises CCD camera Allied Vision Manta G-146B and lens Sill Optics Correctal T85/0.097. Tinius Olsen software Horizon 10.2.1.0 was used for the machine control as well as data acquisition and analysis via built-in pattern recognition algorithms. The recorded nominal stress-strain diagrams were used to determine tensile, flexural and compressive strengths and moduli so as to establish of their dependency on varying infill density.

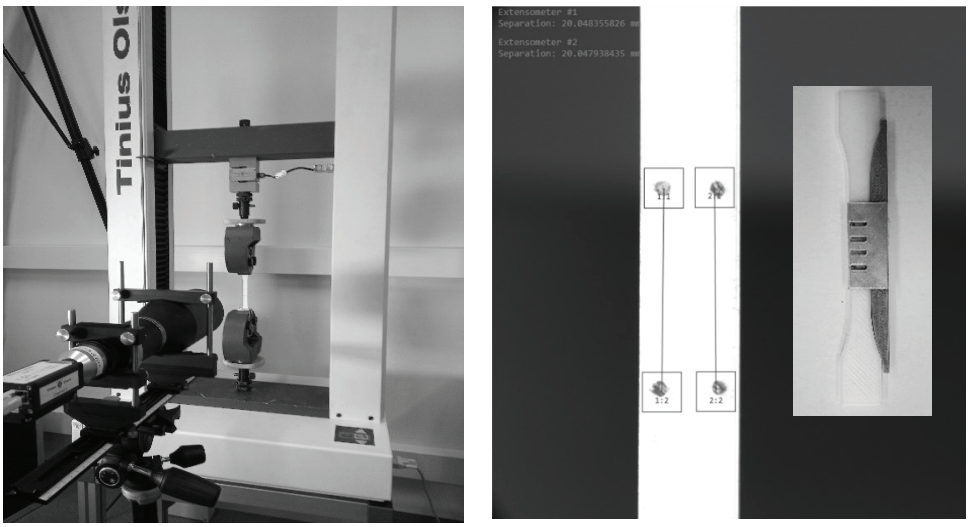

(a) (b)

Fig. 18. Experimental setup: (a) tensile testing specimen mounted on the universal testing machine with video extensometer focused on the points for strain measurement, (b) extensometer reading

Specimens for the tensile test were clamped in manual wedge action grips with serrated jaw surface (Fig. 18(a)). With the aid of a custom-made 3D printed guide, accurate alignment of the clamped specimens in the longitudinal direction with the vertical axis of the machine was achieved. Extensometric measurements were performed by utilizing two- and four-gauge marks (i.e. one- and two-gauge length references) for compression and tensile tests, respectively. These marks served as target points for the deformation-tracking CCD camera. 3D printed fixture was used

during marking to ensure identical positions of the gauge marks on the specimens (Fig. 18(b)). Four-gauge marks for the tensile specimens were positioned on the front sides of the specimen 3 mm from the longitudinal axis. A gauge length of 20 mm was used for tensile and compressive tests. Until the specimen failure stage, the force was applied and the displacement of cross head and strains were measured.

Tensile Type 1B samples were subjected to tensile loading as defined in ISO 527-2 (loading rate – 1 mm/min). The strength in the tensile regime was determined by calculating the ratio between the maximum force measured and the initial cross-sectional area of the sample. Young's modulus is calculated as $(\sigma_2 - \sigma_1) / (\varepsilon_2 - \varepsilon_1)$, where stress values σ_1 and σ_2 are taken at the corresponding strains of $\varepsilon_1 = 0.0005$ and $\varepsilon_2 = 0.0025$.

Following the ISO standard 604, cylinder type specimens were printed for the compression testing (Fig. 19). Specimens of constant diameter and two different lengths were used. Type A specimens with the length of 50 mm were printed for the formulation of compression modulus, whereas type B specimen with the length of 10 mm was required to calculate the compressive strength. In both cases, the rate of loading was kept constant at 1 mm/min. The compression strength and modulus were evaluated analogously to the tensile test.

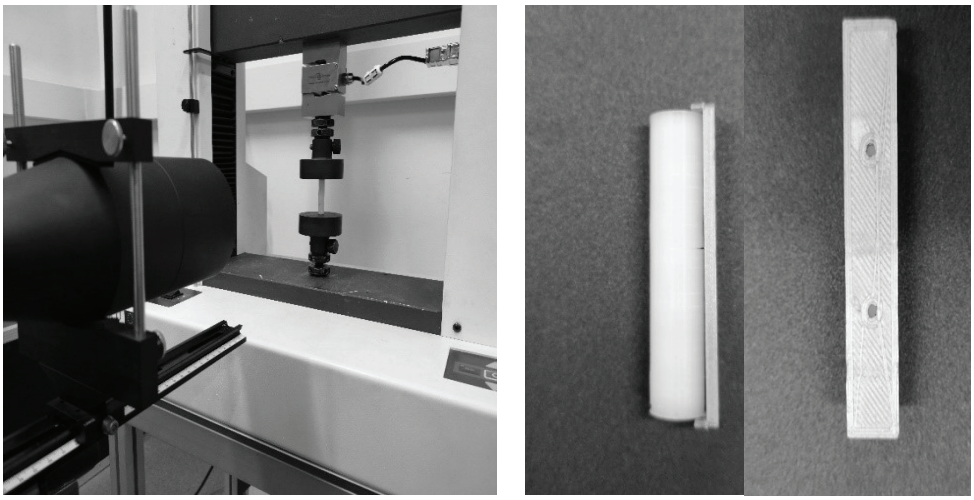

(a) (b)

Fig. 19. (a) Compression testing specimen mounted on the universal testing machine with video extensometer recording the strain, b) compression specimen with 3d printed marking fixture

Implementing the ISO standard 178, rectangular bar specimens were printed for the three-point bending test. A uniform loading rate of 2 mm/min was set for recording stress-strain diagrams, by following method A in the standard. Flexural strain was calculated as ratio $600st / L^2$ by using recorded deflection s, span length L = 64 mm and specimen thickness t = 4 mm.

Flexural modulus of elasticity was calculated as previously. The flexural strength was calculated as ratio $(3F_bL) / (2wh^2)$ by taking measured bending force F_b and specimen width w = 10 mm.

During three-point flexural testing the printed PVDF bar of rectangular cross-chapter is rested on 2 supports of ∅ 10 mm and loaded by a circular edge of ∅ 10 mm midway between the supports. 64 mm span length was set by moving the distance between the specimen supports (Fig. 20). Until the specimen failure, the force applied, and displacement of crosshead were measured.

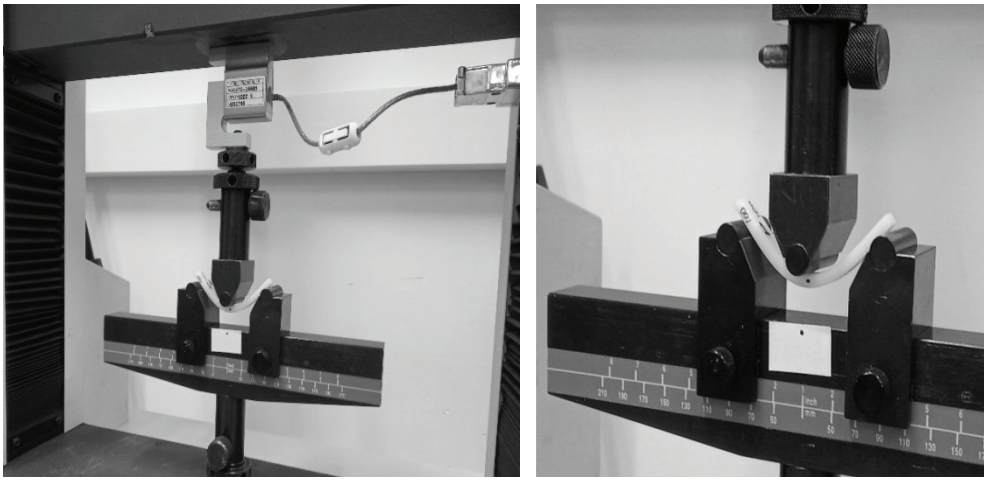

Fig. 20. Flexural testing specimen under flexural loading

2.2. Electromechanical Testing of Printed Piezopolymeric Transducers

The test setup for measuring the piezoelectric signals in FFF printed PVDF sample was implemented. The samples were designed in the form of films and 3D cellular structures (scaffolds) in cubic shape. Using the Spellman SL600, which consists of a high-voltage source connected to 2 electrodes mounted on both sides of the printed film, the printed PVDF parts are subjected to contact poling. The samples were self-suspended, 60 mm apart, between 2 fixtures, and both ends were fixed. The voltage was determined when the poled sample was deflected/compressed on a cyclic testing machine Instron E10000. Transimpedance amplifier designed at the Institute of Mechatronics was included to filter out unwanted noise signals and for obtaining reliable voltage output signals since piezoelectric transducers (sensors) act as current generators.

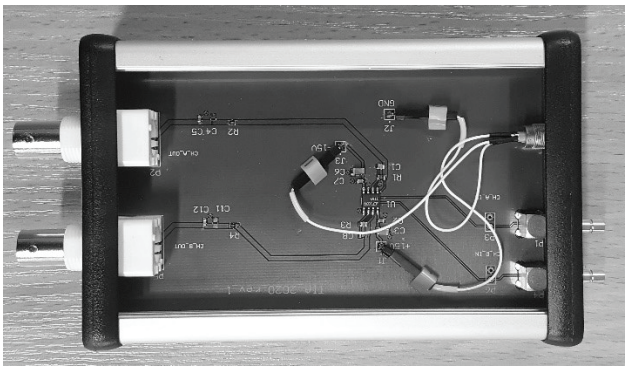

Fig. 21. In-house built assembled transimpedance amplifier in the aluminium casing

The developed amplifier (Fig. 21) is supplied with ±15 V from external power supply (RIGOL DP831A) and three pulses are triggered from source meter of 50 nA (KEYTHLEY 2614B). The response is measured with the oscilloscope (YOKOGAWA DLM2034) and in such way current to voltage coefficient is determined. The output of amplifier is 50 mV when generating current is 50 nA. Implementing the transimpedance amplifier leads to a less possible influence on the signal. The PVDF sample was deflected during mechanical testing so that the deformation is induced perpendicular to the direction in which the PVDF is polarized, i.e. the transverse operating mode of the PVDF transducer ("d31 mode"). The electrodes are linked to a digital oscilloscope that records the electrical response. A shielding layer is implemented to the part and connected to the ground of the coaxial cable for avoiding unwanted noise signals.

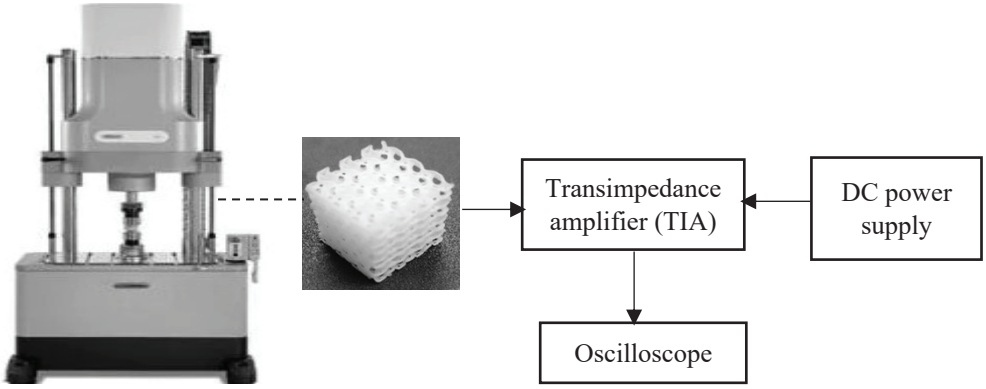

Fig. 22. Schematic of piezoelectric test setup

2.3. Chapter Conclusions

This chapter presented the materials used and the experimental methodology implemented in this research work. The main conclusions are:

1. Three forms of commercially available PVDF-based filaments with diameter of 2.85 mm from Nile Polymers, Inc. were employed in this work:
   - PVDF-H homopolymer filament (Fluorinar-H™).
   - PVDF-C copolymer filament (Fluorinar-C™).
   - PVDF-C-ESD graphene-filled composite (Fluorinar-ESD™).
2. There are no established standardized mechanical test methods that are specifically dedicated to FFF printed parts. Therefore, ISO standards for conventionally processed plastics are adopted for the mechanical testing. ISO 527-2, ISO 178 and ISO 604 standards are used for tensile, flexural and compression testing, respectively.
3. The piezoelectric response of FFF printed PVDF is evaluated by subjecting the samples to mechanical deformation using the cyclic testing machine Instron E10000. A custom 2-channel transimpedance amplifier was developed to accurately measure via digital oscilloscope the low-amplitude piezo-voltage signals generated by the printed thin-layer piezopolymeric transducers fabricated using contact-poled PVDF films and signals generated by unpoled biocompatible PVDF-HFP bioinspired (TPMS) 3D scaffolds.

3. EXPERIMENTAL RESEARCH RESULTS

The way a given part is adapted with respect to the 3 main axes X, Y, and Z of the given machine on the building platform is the build orientation (Fig. 23). Tensile and flexural specimens were printed at flat construction orientation. The layers are heated and stacked in the longitudinal direction of the applied tensile load in the flat orientation. As the maximum tensile strength and flexural strength also lowers printing time, it is widely adopted in FFF [6, 28]. In addition, the study opted for the flat orientation due to the severity of adhesion problems and warpage formation in PVDF-H which is more useful for making good prints.

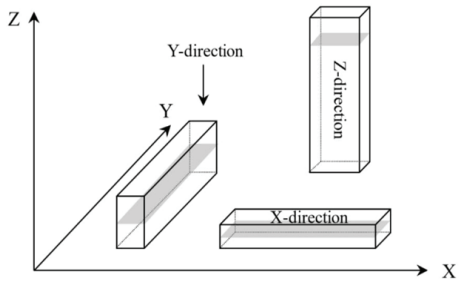

Fig. 23. Notation of build orientations in 3D printing [201]

Compression specimens were printed in an upright (Z) direction as higher compressive strength was reported [202]. In FFF, raster orientation is a key factor as it affects how an applied load is transferred within the component. The completely filled parts (100% infill) were printed using a raster angle of 0° (longitudinal orientation)since the literature reported that the tensile strength along the extrusion direction exceeds that of other orientations [6, 202]. Flexural strength is often preferred by longitudinal orientation, mainly determined by the tensile strength (flexural specimens will first undergo failure at the side that is under tension). The air gap was set to zero for 100% filled prints. Depending on the nozzle size used (0.4 mm), the width of the raster (infill line) is automatically fixed by the Cura program and is equal to ~0.35 mm. Test samples were printed with layer thickness set to 0.1 mm which is mostly used in FFF because of a fair trade-off between printing time and the consistency and strength of the resulting component. The infill was surrounded by a shell of 0.8 mm of thickness.

With a micrometre screw gauge, the dimensions of printed samples were inspected and the weight was measured with precision laboratory scales. Measurement results in Fig. 24 indicate a linear reduction of specimen weights and printing times with lower infill density. For example, it takes from 1.5 to 3 hours to print the largest tensile test specimens with different infills which is at least twice as long as for the flexural and compressive test specimens. PVDF-C-ESD and PVDF-C specimens are slightly heavier than PVDF-H ones. Overall, compared to 100% infill, the print times and sample weights are reduced on average by a factor of 1/2, 1/3, and 1/6, while using 25%, 50% and 75% infills, respectively.

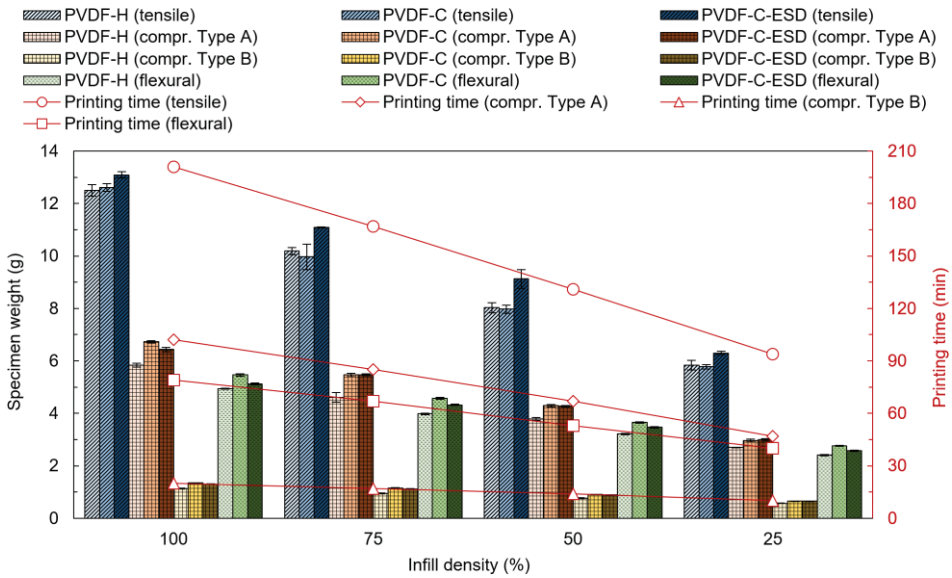

Fig. 24. Weight and printing time of completely and partially filled test specimens: tensile (ISO 527-2/1B), flexural (ISO 178) and compressive (ISO 604)

3.2. Identification of FFF Process Temperatures and Speed[2]

The fluidity of the material that is being printed is directly influenced by the extrusion temperature. The most suitable temperature needs to be determined as the fluidity of the filament material will increase or decrease, which could affect the part being manufactured. While printing, the stresses induced internally arise when the filament is extruded and cools down to ambient temperature from its initially set extrusion temperature, and the variation in deposition speed, the induced stress can lead to the formation of inter/intra-layer deformation, which can lead to failure of the fabricated part [203]. PVDF-based fluoroplastics possess wide temperature window for melt processing (from ~200°C to ~260°C), that is attributable to the significant disparity to the temperatures of melting and thermal decomposition (~155–170°C and 375°C, respectively for Kynar®) [67]. Lower extrusion temperatures tend to benefit dimensional accuracy and surface finishing [54]. In addition, lower extrusion temperatures within the stated temperature range is recommended for better adhesion [204] is recommended for better adhesion. In comparison, higher extrusion temperature leads to higher fluidity of the melt, which is beneficial for thermoplastic inter/intra-layer bonding and can increase part strength [6, 28, 202]. In order to avoid the release of dangerous by-products (e.g., carbonyl/hydrogen fluoride, etc.), it is noted that PVDF temperature of extrusion should not exceed ~290 °C.

In an effort to determine the most favourable extrusion temperature in terms of printability, adhesion and susceptibility to warping, a series of PVDF printing tests were performed using different extrusion temperatures (from 200°C to 240°C). The

[2] Material in this chapter was first published in [200] by Springer Nature

building platform temperature was maintained at 90°C for all printing tasks. It was noted that the PVDF extrudate tends to concentrate near the nozzle while printing above 240°C due to excessive flow rate, i.e., melt burrs are produced due to over-extrusion (Fig. 25(a)). Print quality deteriorates since the melt burrs normally detach from the nozzle during the extrusion phase and contaminate the printed layers, causing surface finish degradation and/or dimensional accuracy (e.g. print layers become uneven). Occasionally, during printing, the burrs can remain cemented to the nozzle tip for a prolonged period, partially obstructing the nozzle, disrupting the continuous extrusion process, and degrading the quality of printing. The printing temperature was gradually reduced to 230°C to avoid over-extrusion which was found to provide a sufficient melt flow rate to ensure a stable extrusion operation. In addition, PVDF printing in the lower temperature range has been observed to minimize warpage problems caused by temperature gradients during the cooling process. In the meantime, printing at an even lower temperature of 220°C resulted in under-extrusion which was reflected in the deposited layers as different discontinuities, e.g. holes, non-uniform layer thickness, delamination, etc. (Fig. 25(b)). The PVDF filament producer's recommended extrusion temperature range is 240°C–260°C [205] but the tests showed that the specimens could be printed more effectively at a lower temperature of 230°C.

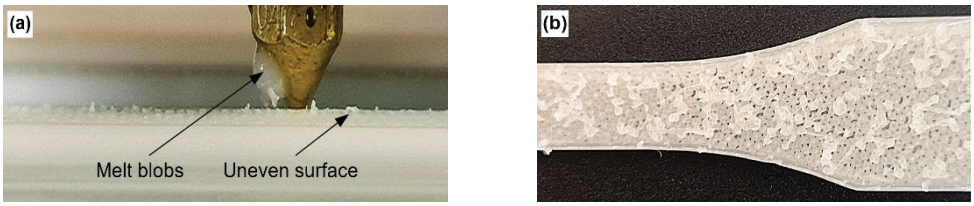

Fig. 25. Example of print issues due to: (a) over-extrusion (formation of melt burrs on the nozzle due to excessive flowrate causing poor surface finish), (b) due to under-extrusion (formation of residual polymer deposits) [200] (Reproduced with permission from Springer Nature)

The speed of nozzle traversing as material is deposited along the XY plane on the platform, is the printing speed in FFF. The speed and the extrusion temperature are interconnected as FFF process parameters. The printing time of the part is dependent upon the speed of printing. The speed also has a dominant effect on the structural part deformation [206]. This is due to the large number of residual stresses formed during the deposition of the material, which in turn is caused by high-speed extrusion process. Nonetheless, the influence of printing speed when fabricating thinner layers is considered insignificant [207]. At higher speed (>50 m/s), PVDF is very problematic to print as it widens the possibility of excessive warpage and detachment from the platform, especially with PVDF-H. Hence, FFF was performed at a lower speed of 20 mm/s in order to maintain stable adhesion to the platform and ensure better printing consistency overall.

3.3. Identification of the means to improve print/platform adhesion

PVDF being partially fluorinated polymer with inherently low surface energy, is favourable owing to ability to repel water [192], but this weakens print/platform bonding strength, particularly in the case of PVDF-H. As it acts as the basis for the subsequent print layers, strong adhesion between the 1st layer and platform is crucial. PVDF-HFP is less problematic to print compared to the homopolymer since sufficiently robust adhesion is typically maintained the entire FFF process. In the meantime, PVDF-H is susceptible to warping and disengagement from the platform. It is difficult to obtain full prints reliably without the use of a proper solution to increase the adhesiveness between the first layer and the platform. Using roughened surface for the platform, covering it with painter's or Kapton tapes and implementing adhesive sticks or sprays are the most widespread adhesion enhancing approaches [208, 209]. In practice, the Kapton or painter's films failed to solve issues with adhesion for PVDF. Instead, to get sufficient adhesion, a uniform dispersion of a solid or aerosol FFF-adapted Dimafix® adhesive was applied on the build platform. The aerosol spray was initially used within the printer housing to cover the glass platform. It contributed, however, to a gradual accumulation of adhesive residues on the moving components of the printer, eventually disrupting the activity of the drive operation. Therefore, adhesive stick was preferred in order to prevent printer contaminations.

However, PVDF-H prints still occasionally detached during fabrication. The implementation of set of supplementary layers extending from the border of the print (called "the brim") was an additional solution to counteract such recurrent warping-induced detachment problems. It increased the surface interaction area to the build podium, with preventing the disengagement of the exterior edges that were printed. The brim was preferred over the raft because without causing any harm, it is easier to remove from the printed portion. In addition, the brim has no effect on the bottom layer surface finish and yields less PVDF waste. The brim layers of PVDF-H often get detached from the printing podium while printing brim layers with widths of less than 6 mm. Fig. 26(a) reveals disconnected brim segments adjacent to the specimen, while the platform is adhered to by the more distant segments. The 8 mm brim was found to be sufficient for proper print by providing adequate PVDF-H layer adhesion (Fig. 26(b)).

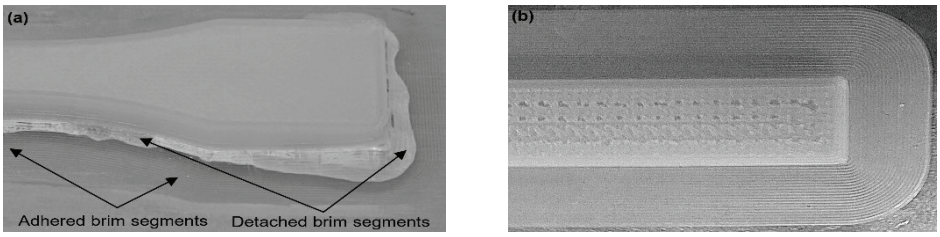

Fig. 26. Usage of brim when printing specimens: (a) tensile specimen with partly detached brim, (b) flexural specimen with strongly adhered 8 mm brim [200] (Reproduced with permission from Springer Nature)

The temperature of the build platform stands out as an essential processing parameter affecting the microstructure as it affects the cooling rate and thermal gradient during printing. Setting the build platform temperature higher than room temperature is usually very important for obtaining high quality prints since it keeps the extruded material warm [210]. The build platform used in Ultimaker 2+ is glass plate. The advantage of using heated glass build platform is that is very easy to remove the print. The usual and the most recommended procedure for the use of build platform is by cleaning it after every print with water or isopropanol. This is contradictory to the rectification method for adhesion of print. Roughening up the build platform is a recommended method for improving the adhesion. Therefore, it was observed that by keeping the applied glue of the previous print on the build platform, improved the adhesion for the subsequent prints.

Table 2. Summary of FFF printing parameters and conditions

Print materials and settings	Value, description
Nozzle diameter	0.4 mm
Adhesion-enhancing layer	Brim (min. width of 8 mm)
Adhesive layer	Dimafix® spray/stick
Fan use (cooling)	No
Extrusion temperature	230 °C
Build platform temperature	90 °C
Printing speed	20 mm/s
Extrusion multiplier	1
Layer thickness	0.1 mm
Print orientation	Flat
Raster orientation	Longitudinal (at 100% infill)
Raster (infill line) width	~0.35 mm
Shell thickness	0.8 mm
Raster-to-raster gap (air gap)	0 (at 100 % infill)
Build orientation	XX

From the literature it was concluded that the build orientation affects the mechanical properties, and in particular the ductility of the samples. Moreover, it is one of the widely researched print parameters. PVDF was also subjected to the three build orientations (XX, XY and XZ), by keeping the rest of the parameter constant. The tested designed was the ISO 527 dumbbell shaped sample. It was observed that it is impossible to print PVDF in XY and XZ direction, as the printed layers deviated from the intended design due to uneven stress release. Table 2 lists main FF process parameters and conditions that were identified to be the most favourable for obtaining full prints with PVDF homopolymer, copolymer and composite filaments.

3.4. Analysis of Infill Density Impact on Mechanical Properties[3]

Using triangular lattice patterns, which are among the most common due to the combination of part strength and process performance, test specimens with partial infill were printed. For sections that have different, pointed corners, triangular infill is more fitting. Compared to the rectangular pattern, it creates stronger parts and is quicker to print compared to the hexagonal infill [211]. Infill densities of 25%, 50%, 75%, and 100% were taken into account in this study (Fig. 27). The infill was encircled by a 0.8 mm thick shell. It is small enough to conclude that with regard to the effect of variable density of infill, the influence of the shell layers on the evaluated mechanical properties is negligible. Using micrometre screw gauges to ensure repeatability of the FFF operation, printed specimens were subjected to dimensional control. The weight of the specimens was determined using laboratory scales.

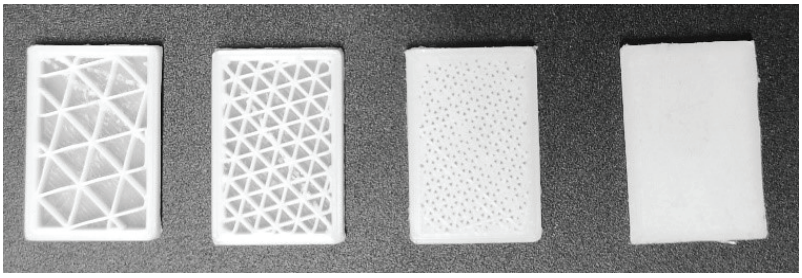

Fig. 27. Examples of PVDF-C prints (20×30 mm^2) with different densities of triangular infill (from left to right – 25%, 50%, 75%, 100%)

Tensile properties

It could be noted in Fig. 28(a) the ductility behaviour with the absence of clearly defined yield point in the nominal stress-strain diagrams for the fully filled PVDF-H specimens (100% infill density), which was also previously observed in the diagrams of PVDF specimens manufactured by other methods [212–214]. Compared to these tests, the 100% filled 3D printed PVDF-H achieves either comparable strains for failure [213, 214] or lower strains [215]. Meanwhile, the 35.7 MPa tensile strength obtained (Fig. 29) is below the previously recorded 40–50 MPa values for the specimens formed through the non-AM process at room temperature. The elastoplastic responses of the 100% filled ones, unlike the partially filled PVDF-H specimens (25%–75% infill), involve an almost constant plateau tension region with low strain softening (Fig. 28(a)).

[3] Material in this chapter was first published in [200] by Springer Nature

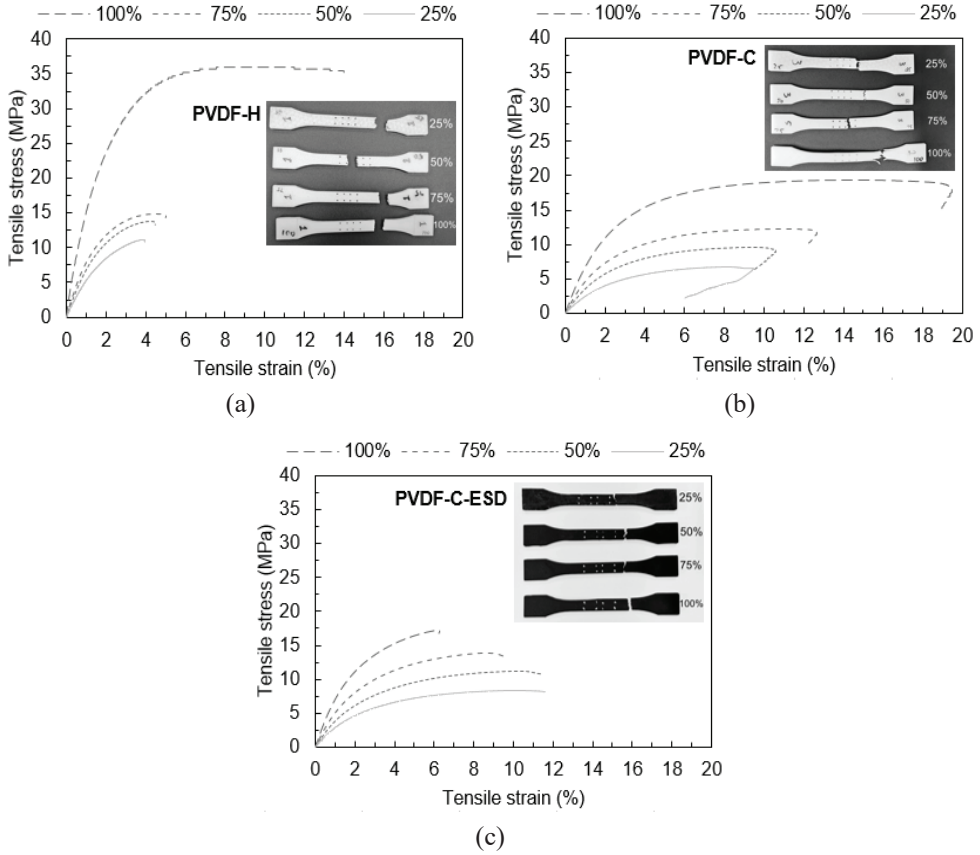

Fig. 28. Tensile stress-strain diagrams of the ISO 527-2/1B specimens 3D printed with different triangular infill densities using (a) PVDF homopolymer, (b) PVDF-HFP copolymer and (c) graphene-filled PVDF-HFP composite

The tensile strength and tensile modulus of the test specimens are presented in Fig. 29 and Fig. 30. It could be seen that tensile strength decreases when the material is less dense, however, a substantial decrease can be seen when material density changes from 100% to 75%. The tensile strength of PVDF-C material decreases from 35.7 MPa to 15.3 MPa and from 20.8 MPa to 10.8 MPa for PVDF-H material, respectively. Meanwhile when density decreases from 75% to 25% a gradual decrease in tensile strength of both materials could be observed. Similar tendencies can be seen where tensile modulus decreases sharply when density changes from 100% to 75% and later a gradual decrease can be observed when density shifts from 75% to 25%.

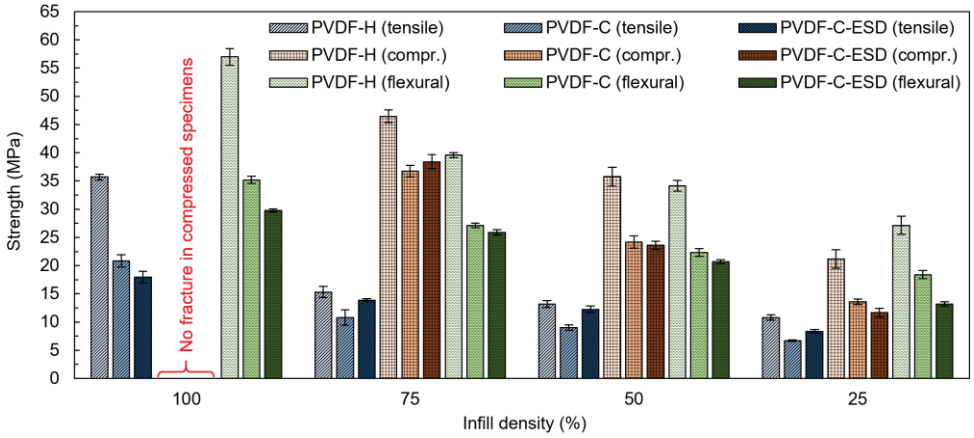

Fig. 29. Tensile, compressive, and flexural strengths of specimens printed with triangular different infill densities using PVDF homopolymer (PVDF-H), PVDF-HFP copolymer (PVDF-C) and graphene-filled PVDF-HFP composite (PVDF-C-ESD)

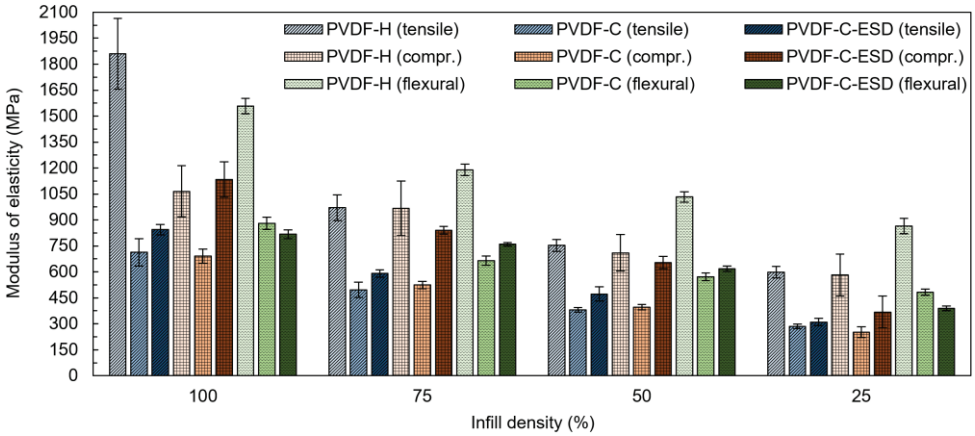

Fig. 30. Tensile, compressive and flexural moduli of specimens printed with different triangular infill densities using PVDF homopolymer (PVDF-H), PVDF-HFP copolymer (PVDF-C) and graphene-filled PVDF-HFP composite (PVDF-C-ESD)

The true stress-strain diagrams of PVDF mentioned in literature, show strain hardening behaviour [212, 216]. Inspection of the failure pattern of the 100% filled PVDF-H in Fig. 31(a) indicates an uneven path of crack propagation along a roughly transverse plane which is perpendicular to the direction of the force applied. Minimal necking and roughened fracture surface indicate moderately ductile failure mode in PVDF-H. Damage mechanisms are considered to be relatively complex in deformed PVDF [217], which is also evidenced by the observation that few of the failed samples contain an indication of stress whitening due to micro void (crazing) growth [214]. In PVDF-C samples, where they are observed more frequently than in homopolymer

ones, the whitened (craze) bands are formed perpendicular to the loading direction and are more abundant. The craze bands are uniformly distributed along the gauge length in PVDF-C specimens (Fig. 31(b)), although they appear to have more cluster around the fracture zone in PVDF-H (Fig. 31(c)).

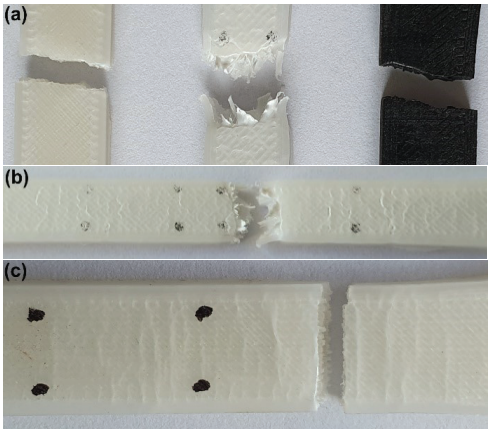

Fig. 31. (a) Fracture zones of PVDF-H, PVDF-C and PVDF-C-ESD specimens (from left to right), (b) examples of craze bands in PVDF-C, (c) PVDF-H [200] (Reproduced with permission from Springer Nature)

It's clear from Fig. 29 and Fig. 30 that stiffness and strength of PVDF-H greatly exceeds the values of PVDF-C (by 71%) and PVDF-C-ESD (by 99%) specimens at 100% infill. However, between the completely and the partially filled cases, the homopolymer experience a significant improvement in tensile properties. For example, PVDF-H with 75% infill have the largest relative decrease in tensile modulus (~48%) and strength (~57%), compared to 100% infill, followed by PVDF-C (~31% and ~48%) and PVDF-C-ESD (~30% and ~23%), respectively. In addition, the plastic deformation area in PVDF-H tensile responses is observed to decrease abruptly with declining infill densities (Fig. 28(a)). Overall, with respect to the other two PVDF variants, the incorporation of partial infill into the PVDF-H specimens causes a greater loss of toughness.

Lower PVDF-C crystallinity favours FFF structural stability and printability, which could be verified by the lowest tensile modulus values of the materials tested (e.g. 285 MPa and 713 MPa at 25% and100% infills, respectively). It is apparent in Fig. 28(b) that the copolymer specimens demonstrate the greatest ductility as shown before failure by the pronounced plastic yield. The zones of fracture presented in Fig. 31 shows the apparent variations in the failure mechanism between the PVDF-C and the other two materials. PVDF-C ductility manifests in the fracture zone by visible necking and fibrous torn surface, which suggests severe plastic deformations before breakup (Fig. 31). However, with respect to the more crystalline homopolymer equivalent, the tensile strength of the pristine copolymer is lower by ~40% on average. It is noted that the decrease in ductility of PVDF-C with a decreased density of infill

is not as extreme as the homopolymer situation. It could be observed that when infill density is reduced from 75% to 25%, ductility shifts moderately in all tested materials.

The tensile properties of the PVDF-C-ESD tend to be less affected by the decreasing infill density among all tested materials. The results of the graphene-filled counterpart suggest more brittle behaviour of material, in comparison to the 100% filled PVDF-H and PVDF-C. In Fig. 28, linear elastic and nonlinear ascending zones devoid of plateau are present, with failure following immediately after the tensile stress point at yield. It is also observed that 100% infill PVDF-C and PVDF-C-ESD samples adopt identical stress-strain evolution up to a strain value of ~5%, though only up to ~0.1% infill at 75% infill. The absence of the neck and the jagged profile of the rupture in Fig. 31 indicates that the fracture of the graphene-filled specimens is almost brittle.

Fig. 30 shows that tensile modulus of all PVDF-C-ESD specimens is greater by ~18% when compared to the PVDF-C material. Whereas it could be seen in Fig. 29 that the average strength of the 100% filled PVDF-C-ESD is lower by ~50% and ~14% with respect to the homopolymer and pristine PVDF copolymer, respectively. Due to lower ductility and strength of the 100% filled PVDF-C-ESD samples, it could be speculated that the Fluorinar- ESD™ filament is made with the same Kynar Flex® PVDF-HFP grade used for Fluorinar-C™ [86, 218]. Due to inadequate interfacial adhesion between the fluoropolymer and graphene, the dominant one may be correlated with matrix/filler debonding. PVDF is intrinsically hydrophobic, while PVDF-C is even more hydrophobic than homopolymer with a higher fluorine content (due to the addition of HFP) [219]. In addition, there is a possibility of certain inhomogeneities of graphene dispersion in the composite filament, i.e. agglomerations that lead to microstructural defects that concentrate stress that can encourage brittle failure. Which graphene derivative is used in Fluorinar-ESD™ filament is not known but it has been previously stated that compounding PVDF with carbonate nanofillers (graphene nanoplatelets, (reduced) graphene oxide, etc.) can result in improvement or deterioration of the strength and/or ductility of the nanocomposite, depending on the concentration of the filler, properties, method of dispersion, etc. [220, 221].

It is important to note that PVDF-C-ESD samples retain greater strains at low densities for failure (Fig. 31(c)), which is contrary to the pattern observed in PVDF-C and PVDF-H. The influence of infill lattice displacements (structural deformations of the struts) caused under stress could arguably be due to such a positive effect of partial infill on ductility. It is understood that the triangular lattice is characterized by stretching-dominated conduct [222]. Therefore, in the case of material that naturally exhibits near-brittle behaviour, these additional stretching displacements may significantly contribute to specimen elongation (i.e. 100% filled PVDF-C-ESD). Similar findings have been reported previously for ABS-based composites [112], which exhibit failure strains comparable to those of PVDF-C-ESD (~5%–6%). Comparison of outcomes given in Fig. 29 shows that in terms of average power, the

partially filled PVDF-C-ESD specimens outperform the PVDF-C ones, which contrasts with the outcomes in the 100% infill case.

Description of outcomes of experiments in Fig. 29 and Fig. 30 reveals that there is a substantial difference in terms of measured tensile strength and modulus between the 100% filled PVDF-H and the copolymer specimens as well as in terms of ductility between the 100% filled PVDF-C-ESD and PVDF homo-/copolymer specimens. The structural integrity of load bearing ESD-safe components printed not only with PVDF-H/C but also with PVDF-C-ESD for the dissipation of electrostatic charges could be adversely affected by these dissimilarities in mechanical properties. It was noted, however, that the introduction of partial infills into the samples leads to more comparable mechanical properties of the PVDF-based materials tested, particularly in terms of tensile strengths which are gradually reduced when infill densities drop from 75% to 25%. Results in Fig. 28(b)-(c) also reveal comparable toughness of the partially filled PVDF-C and PVDF-C-ESD specimens.

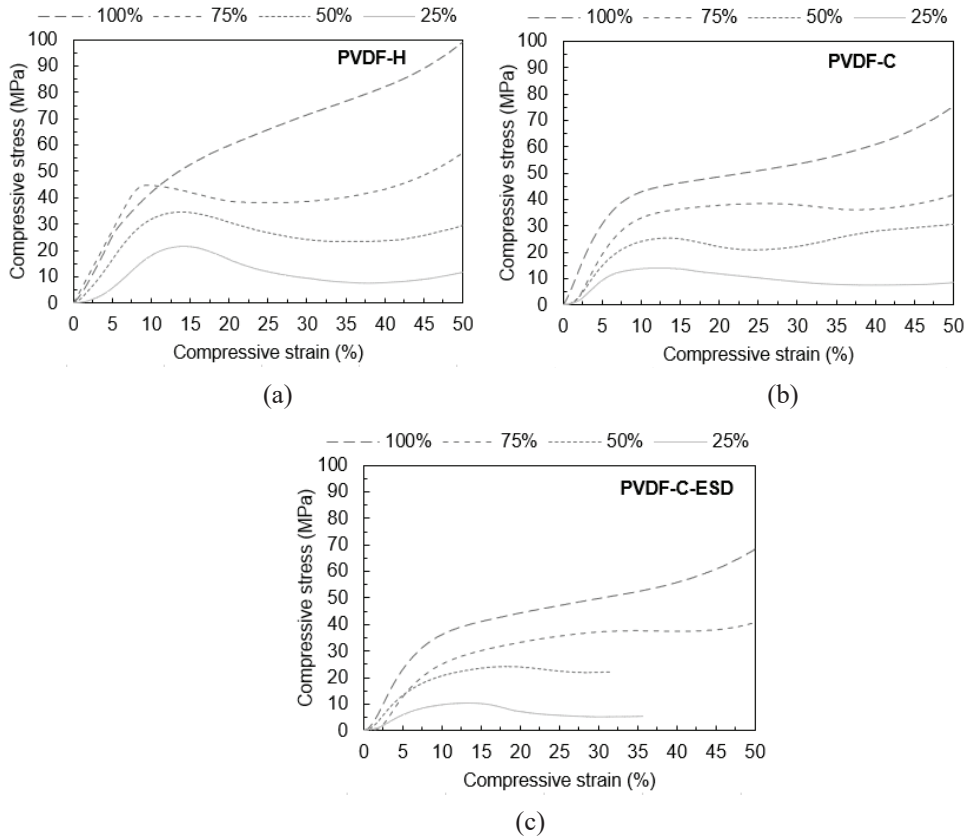

Fig. 32. Compressive stress-strain diagrams of ISO 604 Type B specimens printed with different triangular infill densities

Compressive properties

Fig. 32 shows representative compressive stress-strain diagrams. It is noted that there was no definite fracture in 100% filled specimens (they were merely flattened), so the corresponding diagrams are discarded as not relevant and are not analyzed. Results given in Fig. 32, unlike the tensile example in Fig. 29 indicate similar compressive strength values for the partially filled PVDF-C and PVDF-C-ESD. Similar to the tensile case, partially filled PVDF-H specimens are found to outperform PVDF-C and PVDF-C-ESD specimens on average by ~43% and ~51%, respectively, in terms of compressive strength (the corresponding increase in tensile strength was ~50% and ~16% in excess). The disparity in compressive strength between the homopolymer and its copolymer equivalents is observed to increase with an infill density that decreases from 75% to 25%.

Comparing the tensile and compressive responses of the partially filled specimens and examining the differences (Fig. 28 and Fig. 32), it can be observed that the compressive specimens respond to uniaxial loading in a much more ductile way. Responses from PVDF-H in Fig. 32 with regard to the copolymeric equivalents demonstrate more pronounced strain-softening activity as well as more clearly defined yield points. Overall, by comparing elastic and plastic regions of the corresponding tensile and compressive responses, no symmetry is observed. Such material behaviour is expected because ductile thermoplastics usually exhibit tension-compression asymmetry [223]. This means that the compressive yield strength is higher than the tensile strength (Fig. 29). In terms of the structural integrity of 3D printed load-bearing parts, this means that the mechanical properties derived from tensile testing are not capable to reflect accurately the mechanical compression behaviour. The ratio of compressive to tensile strength (strength differential D_s) can quantify the degree of such asymmetry. In terms of load-bearing 3D printed parts structural integrity, it means that the mechanical properties derived from tensile tests cannot accurately represent mechanical behaviour under compression. The degree of asymmetry may be quantified by the ratio of compressive to tensile strengths, referred to as strength differential D_s. Results of the partially filled PVDF samples given in Fig. 33 indicate major tension-compression asymmetry, which for lower infill densities is found to decrease. At 75% infill, Ds for the specimens ranges from approx. 2.8 to 3.4, which, relative to non-printed solid thermoplastics, indicates more significant asymmetry ($D_s \approx 1.0–1.8$ [223]). The partially filled PVDF-C-ESD specimens are found to have the lowest strength differential. The discrepancy in D_s between the PVDF-C and PVDF-H disappears with lowering of infill density, while D_s for the PVDF-C-ESD diverges from the other two materials by achieving the lowest value of 1.4 at 25% infill.

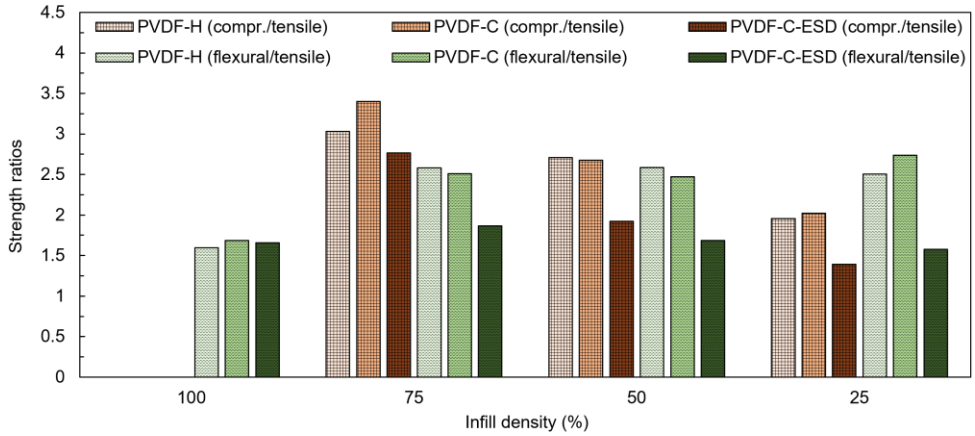

Fig. 33. Ratios of means values of compressive to tensile strengths and flexural to tensile strengths vs. infill density

The compressive modulus is also observed to steadily decrease with lower infill densities as in the case of the tensile modulus (Fig. 30). The compressive module of the 100% filled PVDF-H is obviously smaller than the tensile modulus (by ~43%) but in partially filled situations, the gap (elastic anisotropy) effectively disappears. There are also fewer variations between PVDF-H and PVDF-C-ESD in compressive modules at all infill densities compared to the respective modules obtained in stress (here PVDF-C and PVDF-C-ESD presented close values of the tensile modulus). Unfortunately, the treatment of these findings is exacerbated by the relatively low accuracy of the compressive module PVDF-H values as demonstrated by broad dispersion. It is noted that at a given infill density, highly ductile PVDF-C specimens show comparable tensile and compressive moduli. PVDF-C-ESD specimens, on the other hand, are found to exhibit elastic anisotropy as tensile modules are ~28% lower than compressive at 50%–100 % and ~16% at 25% infills.

Flexural properties

In order to provide additional insights into the strength performance of 3D printed PVDF specimens under the combined impact of compressive, tensile, and shear stresses, flexural testing was performed. The failure of the bending specimens is largely determined by the tensile strength since it is substantially lower than the compressive strength [202]. In contrast to the PVDF-C and PVDF-C-ESD nominal stress-strain curves, the partially filled PVDF-H specimens show different bending behaviours (Fig. 29). The introduction of the partial infill into flexural specimens substantially modifies the responses, consistent with the tensile responses of PVDF-H (Fig. 34(a)). In contrast to the test results of copolymer equivalents, it manifests as a more dynamic stress-strain evolution during fracture and a more significant reduction of flexural strength.

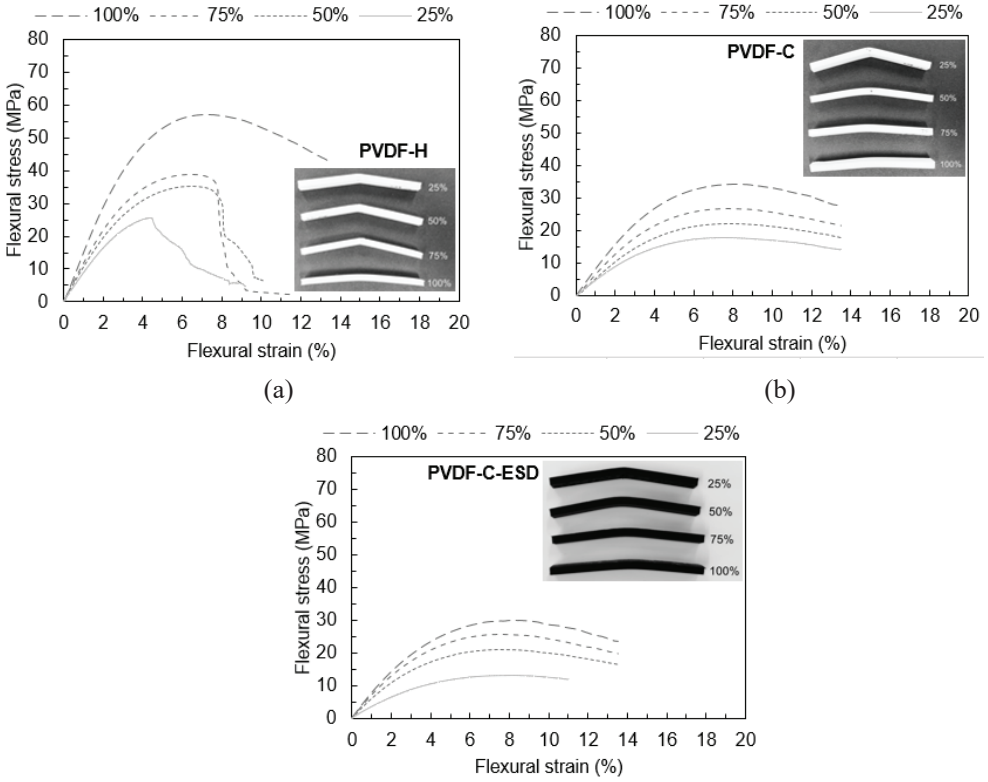

Fig. 34. Flexural stress-strain diagrams of ISO 178 specimens printed with different triangular infill densities

As in the case of tensile and compressive measures, PVDF-H substantially outperforms PVDF-C and PVDF-C-ESD in terms of flexural strength (on average ~52% and ~79%, respectively) at all infill densities. Overall, the review of findings at all infill densities from all types of quasi-static tests suggests that PVDF-H exceeds PVDF-C in strength to a comparable extent (by ~43%–55% on average). At 100% infill, the flexural strength of PVDF-C is found to be superior to that of PVDF-C-ESD even in partially filled situations, unlike the results of tensile testing. The effect of the external shell (100% filled outermost print layers) that is present in the printed specimens, may be the probable deciding factor for the observed disparity. More specifically, these external layers have a greater effect on strength efficiency during the flexural one, compared to the tensile test as they are subjected to the highest tensile stresses during bending.

It is apparent in Fig. 29 that the flexural strength efficiency of the printed materials at all infill densities is higher than the tensile one. In almost all 3D printed materials, this variation in strength is anticipated and correlates with the presence of internal defects. More precisely, only half of the specimen is under strain during

bending, while the entire specimen is exposed to tension during tensile testing, which means an increased risk of internal defects (i.e. stress concentrators) and, therefore, a greater likelihood of failure, thus a lower tensile strength. Consequently, for all the tested components, the tensile strength constitutes about 3/5th of the flexural one in the 100% filled case. Meanwhile, the tensile strength is on average between 2/5th and 3/5th of the flexural strength for PVDF-H/C and PVDF-C-ESD in partially filled situations. Comparison of flexural to tensile strength ratios shows comparable values at all infill densities for the PVDF-C-ESD samples (Fig. 33). By contrast, the introduction of partial infill into more ductile specimens of PVDF-H and PVDF-C raises the ratio, which remains largely indifferent to the difference in density within the 25%–75% range. Contrary to this finding, in the case of compressive to tensile strength ratios which are decreased by infill density, the corresponding sensitivity is present (Fig. 34). In addition, a comparison of strength output under bending and compression in the 25%–75% infill range shows that the compressive strength is substantially greater than the flexural strength for all three PVDF-based materials at 75%, at 50% they become comparable, and at 25% the situation reverses and the flexural strength exceeds the compressive one.

As in the tensile test case, PVDF-H flexural modulus greatly exceeds that of its copolymer counterparts. With infill density, flexural modulus is reduced, although the shift is not as pronounced for PVDF-C-ESD specimens. It is noted that relative to the tensile one the presence of infill has a low impact on flexural modulus. This is especially obvious for PVDF-H because its tensile module is greater than the flexural one at 100% infill but the relationship reverses at 75% and lower infill densities and the flexural module substantially exceeds the tensile one. Furthermore, the flexural moduli are superior to the tension and compression for the partially filled PVDF-H and PVDF-C specimens, while for PVDF-C-ESD, they are higher compared to the tension ones. The latter material shows comparable flexural and tensile moduli at 100% infill.

3.5. Analysis of Standard Infill Pattern Impact on Mechanical Properties[4]

In this study standard (i.e. strut-based) 3D printing patterns are investigated. These patterns are considered to be the most common patterns that are available in almost every print slicing software. The pattern studied here are: lines, concentric, cross, cubic, octet, zigzag and triangles.

Tensile properties

The strength and stiffness are the main parameter that determine the behavior of cellular or voided materials for use in various lightweight applications. Representative tensile stress-strain relationships of different patterns of PVDF C and PVDF H tensile specimens are shown in Fig. 35 with the strain directly derived from the extensometer. The stress-strain behaviours indicate the variations in ultimate tensile strength and

[4] Material in this chapter was first published in [228] by Elsevier

stiffness of different pattern effects on PVDF material. The average tensile modulus, strength, and elongation are shown in Fig. 36, Fig. 37, and Fig. 38. PVDF C samples showed high levels of elongation compared to PVDF H. In general, the concentric pattern showed a large linear elastic region until reaching peak stress value and the cross pattern showed the lowest linear elastic region

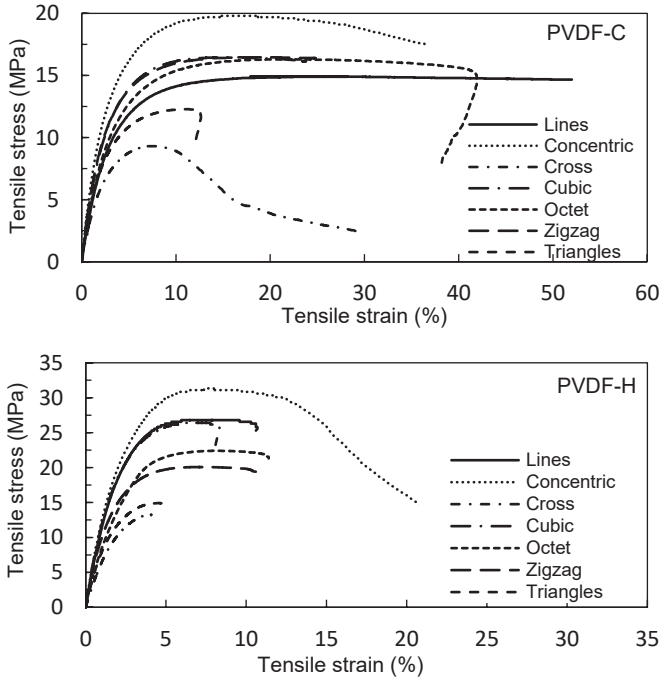

Fig. 35. Tensile stress-strain diagrams for PVDF-C and PVDF-H specimens printed with different strut-based infills at 75% density

During the tensile testing, it could be seen that PVDF-C line pattern showed very high elongation, and, in all cases, the maximum load is observed followed by the initiation of plastic region leading to a necking phase. Once the necking is initiated, fracture propagates at the centre of the specimen and extends along the loading direction resulting to the familiar cup and cone fracture. The displacement measured by the longitudinal extensometer is no longer valid as the measuring strain point went out of frame. During this phase, crack propagation could be visible on the layers and the effect of load gradually decreased leading to the beginning of strain softening phase. The higher elongation behaviour is due to the combined effect of the ductility of the PVDF-C material, the alignment of layers in the pattern and the relation between the print direction and the loading direction. Comparing to other pattern PVDF-C Line pattern is summarized as the highest ductile print with plastic region. PVDF-C line pattern recorded an average ultimate strength of 15.3 MPa and an average modulus of 522.5 MPa whereas PVDF-H recorded a maximum strength of 27.4 MPa and a modulus of 1306.4 MPa.

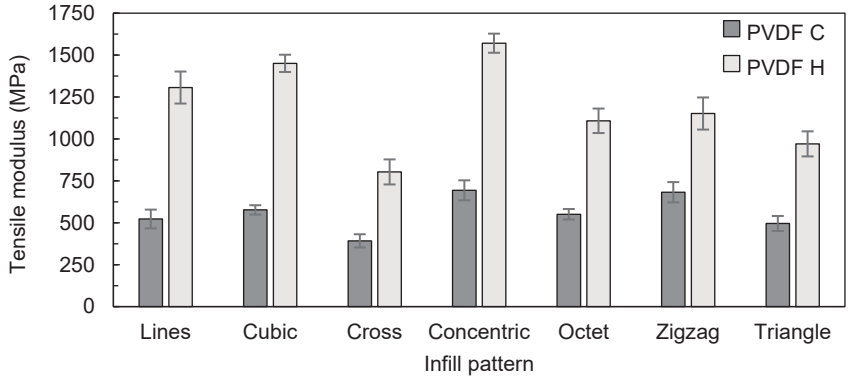

Fig. 36. Tensile modulus of the printed specimens vs infill pattern

Concentric pattern showed the highest tensile strength and modulus in both the materials. From the stress-strain diagrams of PVDF-C concentric pattern, it is noted that a higher proportional region is observed followed by the ultimate stress point causing to beginning of strain softening phase. Few of the samples showed the initiation of necking phase after the maximum load is achieved. This effect could be neglected as the break or rupture point was formed before the necking formation. Concentric PVDF-H is also describing a point of interest diagram as it is the only pattern among other tested pattern that showed an elevated strain-softening phase before gradual break, leading to a quasi-brittle fracture. These types of fractures are observed in polycrystalline ceramics and cementitious materials as they show a measurable deformation prior to failure. This directly show the influence of the circular pattern on brittle PVDF-H material. PVDF-C concentric pattern reported an average ultimate strength of 19.9 MPa and an average modulus of 693.5 MPa whereas PVDF-H reported a maximum strength of 32.2 MPa and a modulus of 1570.8 MPa.

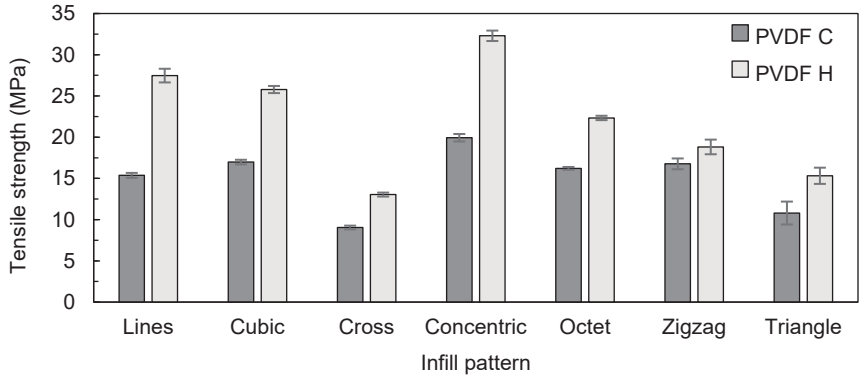

Fig. 37. Tensile strength of the printed specimens vs infill pattern

The cubic and zigzag PVDF-C pattern shows almost identical stress-strain diagrams exhibiting the same failure trend, modulus and strength whereas in the case

of PVDF-H, the cubic pattern showed higher strength than zigzag along with an elastic brittle state in the softening region. This shows that these patterns give more effective influence on brittle materials. PVDF-C cubic and zigzag pattern documented an average ultimate strength of 16.9 MPa and 16.7MPa respectively and an average modulus of 576.5 MPa and 725 MPa whereas PVDF-H cubic and zigzag pattern documented a maximum strength of 25.7 MPa and 18.8 MPa and an average modulus of 1450.7 MPa and 1151.6 MPa respectively.

Once the ultimate strength is reached, the PVDF-C octet pattern developed a plastic phase before the complete break. The formation of cubes in the pattern could cause this ductility in the material. Octet PVDF-H showed a semi brittle nature with a narrow strain softening region. PVDF-C octet pattern reported an average ultimate strength of 16.2 MPa and an average modulus of 550.7 MPa whereas PVDF H reported a maximum strength of 22.3 MPa and a modulus of 1108.1 MPa.

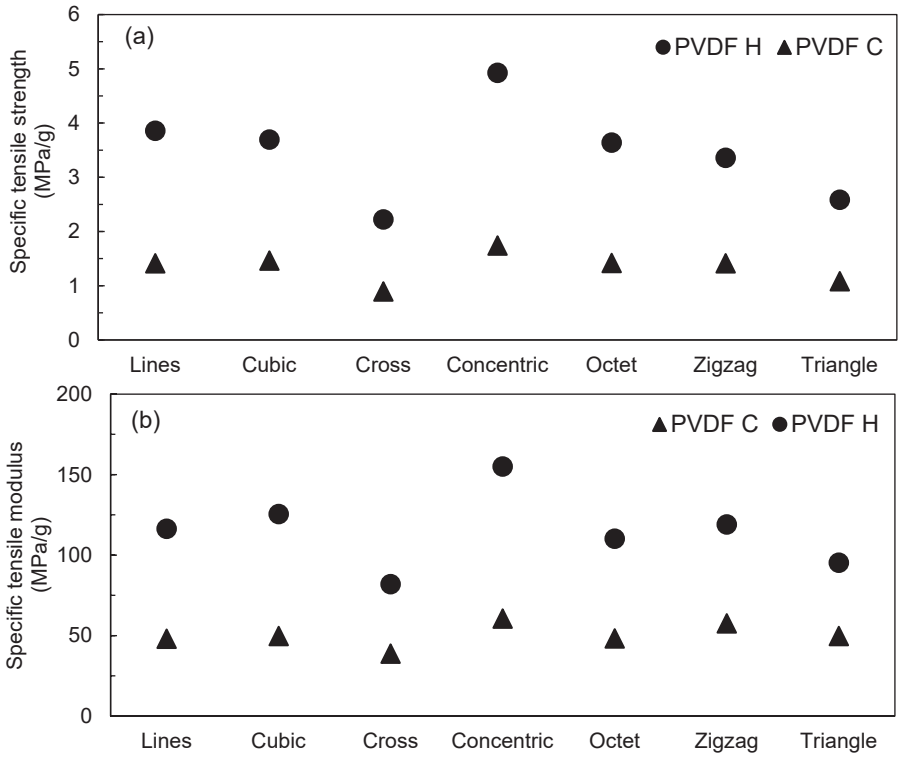

Fig. 38. (a) Specific tensile strength and (b) specific tensile modulus of the printed specimens vs infill pattern

The cubic and zigzag PVDF-C pattern shows almost identical stress-strain diagrams exhibiting the same failure trend, modulus and strength whereas in the case of PVDF-H, the cubic pattern showed higher strength than zigzag along with an elastic brittle state in the softening region. This shows that these patterns give more effective influence on brittle materials. PVDF-C cubic and zigzag pattern documented an

average ultimate strength of 16.9 MPa and 16.7MPa respectively and an average modulus of 576.5 MPa and 725 MPa whereas PVDF-H cubic and zigzag pattern documented a maximum strength of 25.7 MPa and 18.8 MPa and an average modulus of 1450.7 MPa and 1151.6 MPa respectively.

For further evaluation of the effect of patterns on PVDF materials, specific strength (strength/weight ratio) and modulus (modulus/weight ratio) are depicted in Fig. 38. As shown in the figure, the largest specific strength values belong to concentric pattern in both materials and cross pattern portrayed inferior specific strength. The specific tensile modulus depicted a similar diagram to that of specific strength as seen. It is interesting to note that line pattern showed higher specific strength compared to cubic pattern whereas it showed an opposite behaviour in specific modulus. Similar variation can be seen in octet and zigzag pattern.

Fig. 39 shows the tensile elongation at peak stress for different infill patterns. The elongation values were calculated by the increase in gripping distance to the original distance. The average of analysed infill pattern elongation is formulated in the graph. The factors that affect the tensile elongation are the velocity of testing, loading direction, and temperature. They are kept uniform for all test specimens. The different patterns improved/reduced the stiffness of the samples due to enhanced bonding between layers printed, and thus increased/decreased the elongation.

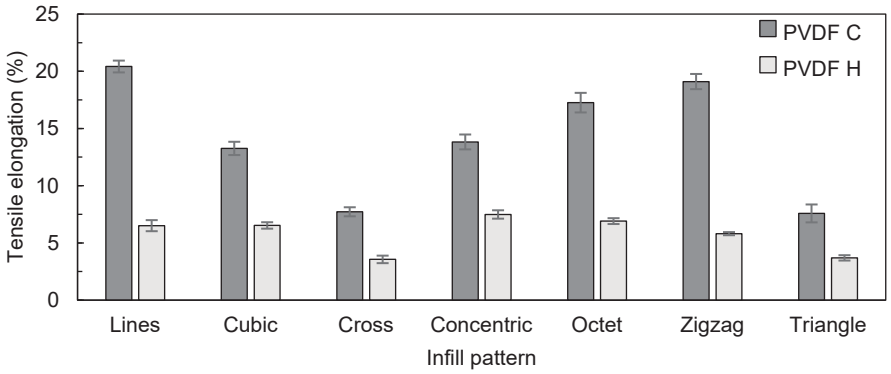

Fig. 39. Tensile elongation of the printed specimen vs infill pattern

It is evident from Fig. 39 that the ductility is higher in PVDF-C material with significant changes in elongation when printed in different pattern. The higher elongation is caused by the elastic behaviour of the PVDF-C material. In PVDF-C, lines and zigzag pattern showed the most elongation with 20.4% and 19.1% followed by octet with 17.2 %. The tensile elongation for cubic and concentric pattern showed a similar elongation with 13.2% and 13.8%, respectively. The lowest elongation was reported by triangles and cross pattern with 7.5% and 7.7%, respectively.

The effect of pattern on PVDF-H is almost insignificant. Concentric pattern reported the highest elongation with 7.4% and the lowest by cross and triangle pattern with 3.5% and 3.6% respectively. Lines and cubic patterns showed similar elongations with 6.5% and octet with 6.9%.

Flexural properties

Flexural behaviour is determined by 3-point bending. The samples are subjected to loading until failure is formed on the surface. The flexural stress experienced by the sample is concentrated at the spot at the loading end where the maximum bending of the sample cross-section is experienced. The maximum flexural stress is a combination of compressive stress at the top surface which is in contact with the loading end and tensile stress at the bottom surface. The flexural stress strain is presented in Fig. 40. For flexural loading on PVDF-H, the diagrams showed a linear regime with a brittle failure mode. For PVDF-C, cross, cubic, octet and zigzag pattern, the diagrams displayed a linear regime with a staircase effect caused due to subsequent strut (pattern connecting line) failure along with crack propagation on the outer layer.

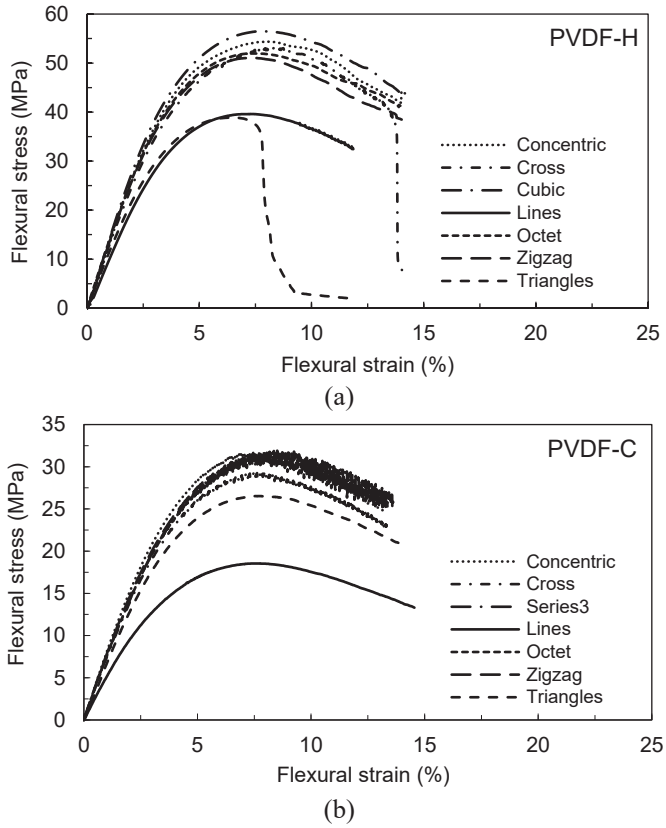

Fig. 40. Flexural stress-strain diagrams for (a) PVDF-H and (b) PVDF-C specimens printed with different strut-based infills at 75%

Fig. 41 and Fig. 42 present the average flexural strength and modulus with respect to different patterns. For the three-point bending tests pertaining to the loading direction applied, the stress in the specimen is more complicated than in the tensile test since the specimens are subjected to both tensile and compressive stress during

bending. The flexural strengths for each pattern in both materials were also found to be greater than the tensile strengths. Concentric, octet, cubic, and zigzag showed the highest strength in ~31 MPa for PVDF C material. PVDF C cross and triangle reported 29.4 MPa and 27.1 MPa, respectively. PVDF-C lines presented the lowest strength with 18.2 MPa.

PVDF-H cubic and concentric reported the highest flexural strength with 55.3 MPa and 54.4 MPa respectively. Octet, cross and zigzag PVDF-H showed a similar flexural strength with 51.7 MPa, 51.5 MPa and 50.3 MPa while lines and triangles pattern showed the lowest strength with 40.7 MPa and 39.5 MPa.

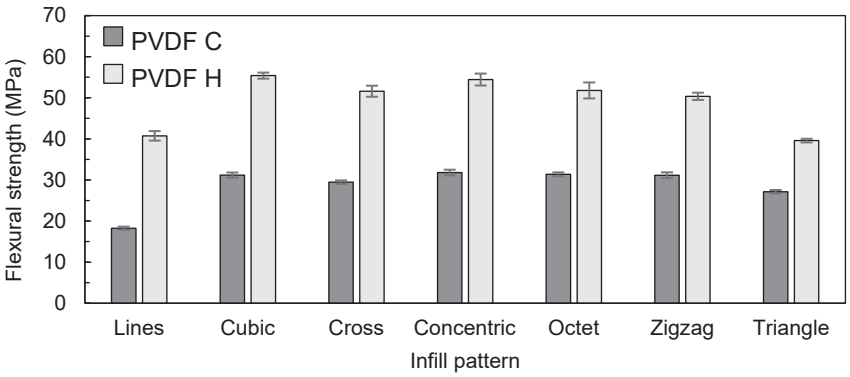

Fig. 41. Flexural strength of the printed specimens vs infill pattern

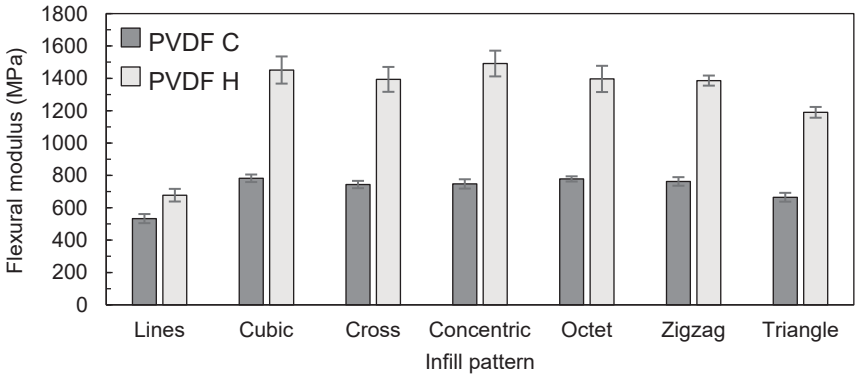

Fig. 42. Flexural modulus of the printed specimens vs infill pattern

The flexural modulus is calculated as the ratio of stress to strain and is depicted in Fig. 42. Due to the brittle nature of PVDF-H, the materials resistance to bending is higher than ductile PVDF-C. The lines pattern showed the lowest modulus value with 532.9 MPa and 677.6 MPa for PVDF-C and PVDF-H respectively. The remaining pattern showed almost the same modulus values in both materials. The flexural loading is done perpendicular to the print direction. Due to the formation of the pattern, this particular factor is vital in influencing flexural behaviour. From the design, it is possible to observe the formation of the pattern. As the layer progresses,

the patterns are stacked in a direction parallel to the loading direction. The cross pattern is claimed to have very flexible features based on its layer alignment, which is shown to be accurate from the flexural results in comparison to the tensile test results, resulting in the conclusion that the cross pattern withstands higher strength in the vertical direction. The line pattern has been observed to be weaker in vertical loading conditions as it showed higher strength in horizontal loading. The cubic and concentric pattern were recorded to have the highest stiffness value with 782.1 MPa and 747.2 MPa in PVDF-C and 1451.2 MPa and 1491.4 MPa in PVDF-H respectively, making these patterns stronger in both loading conditions. The octet and zigzag patterns showed similar values 778.2MPa and 762.6 MPa in PVDF-C and 1396.3 MPa and 1385.9 MPa in PVDF-H respectively. Triangle pattern showed an intermediate behaviour in vertical loading condition similar to the tensile loading, with 664.9 MPa in PVDF-C and 1189.7 MPa in PVDF-H.

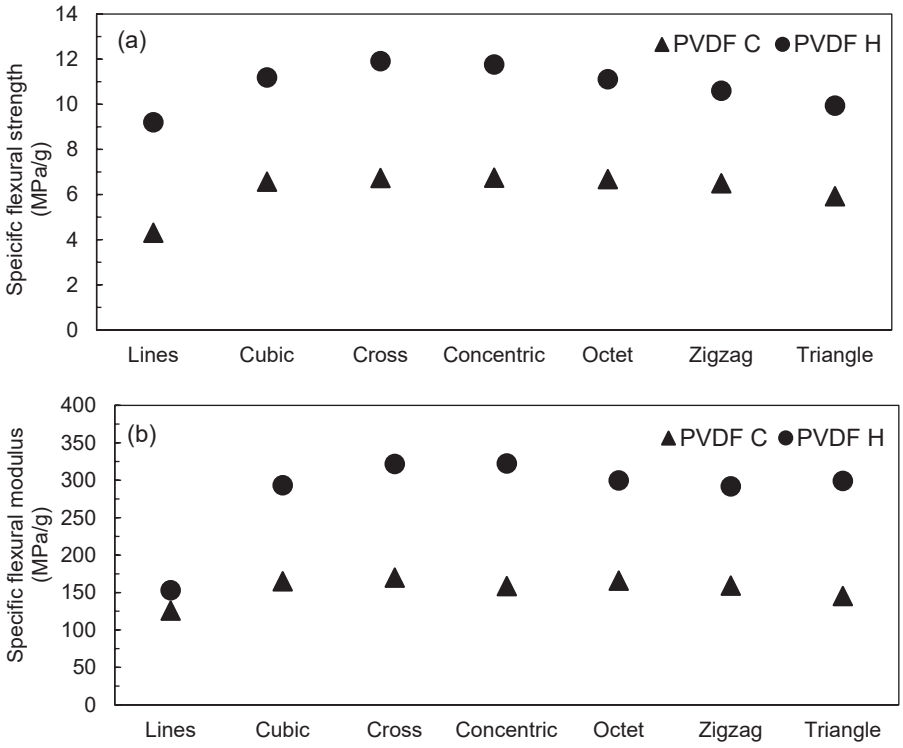

Fig. 43. (a) Specific flexural strength, (b) specific flexural modulus of the printed specimens vs infill pattern

The computed values of specific flexural strength (strength/weight ratio) and specific modulus (modulus/weight ratio) are shown in Fig. 43. The graph affirms that cross and concentric patterns exhibited highest specific flexural strength and line pattern displayed lower specific strength in PVDF-H material. The difference in the

specific flexural strength in regard to filling pattern is irrelevant in PVDF-C material, except line pattern which showed lowest specific strength and all other patterns showed a similar value. With regard to flexural specific modulus, PVDF-H shows a diagram similar to specific strength with the exception of specific modulus in triangle pattern which showed a similar value to zigzag pattern and higher specific modulus difference in line pattern in comparison to another pattern. The specific modulus variation in PVDF-C is almost insignificant with cubic, cross, octet and zigzag showing a similar value. Line pattern showed the lowest without significant steep variation to other patterns and cross pattern recorded the highest specific modulus.

3.6. Analysis of TPMS Infill Pattern Impact on Mechanical Properties

TPMS structures are major ongoing research in the field of AM industry. The section presents the evaluation of Gyroid, Schwarz Primitive and Schwarz Diamond (Fig. 44) structures under tensile and flexural loading conditions. The patterns are printed with 75 % infill density with 3 layers of shell layers and in XYZ build orientation. The STL file is generated by implementing the equations (1–3) and the slicing parameters are set in order to achieve a stable print model without any layers collapsing at any point in printing.

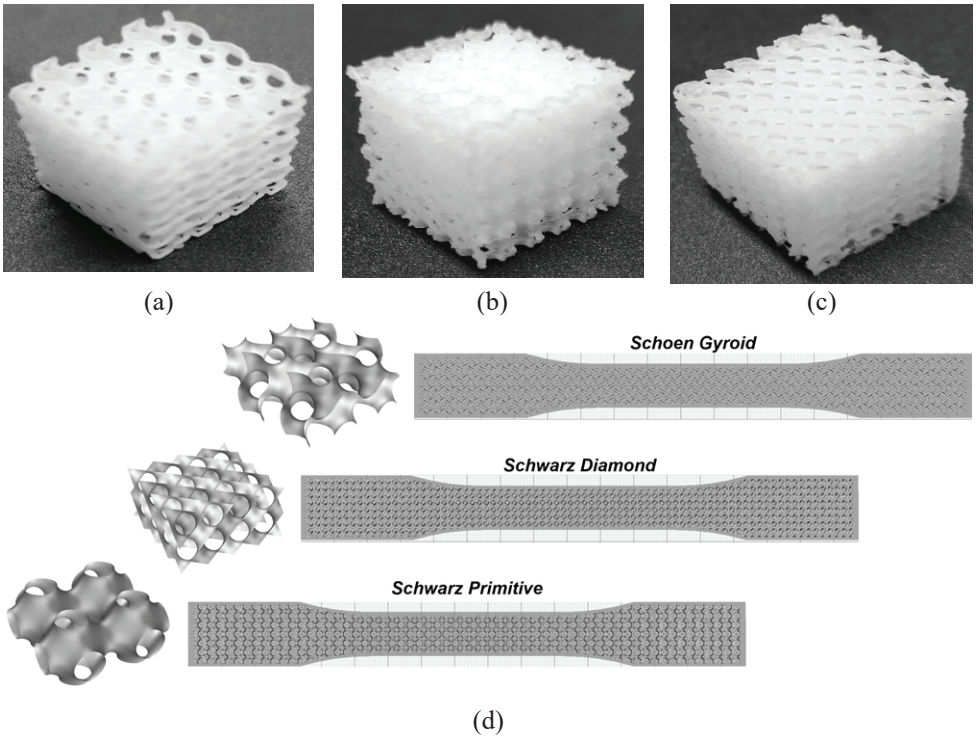

Fig. 44. Printed TPMS patterns: (a) Gyroid, (b) Schwarz Primitive, (c) Schwarz Diamond. (d) Tensile specimens filled with TPMS patterns in Ultimaker Cura software

Tensile Properties

Tensile stress-strain relationships of TPMS patterns of PVDF-C and PVDF-H tensile specimens are shown in Fig. 45 with the strain directly recorded from the extensometer. The displacement measured by the longitudinal extensometer is valid for all the specimens as the measuring strain point did not go out of frame. The stress-strain behaviours indicate the variations in ultimate tensile strength and stiffness on PVDF TPMS pattern materials. The average tensile modulus, strength, and elongation are shown in Fig. 46. PVDF-C samples showed high levels of elongation compared to PVDF-H.

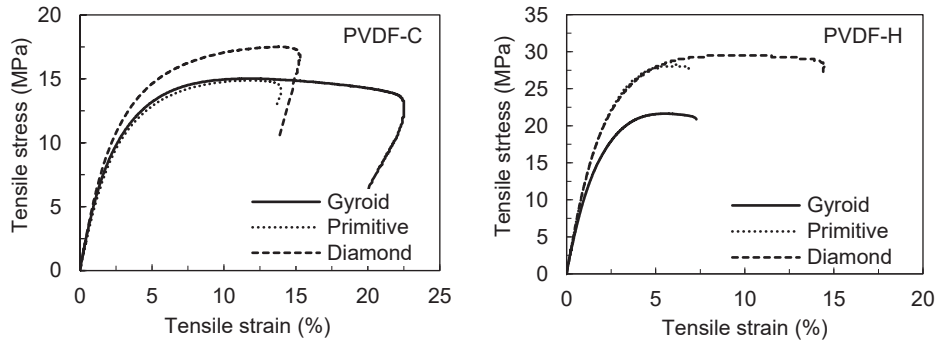

Fig. 45. Tensile stress-strain diagrams for PVDF-C and PVDF-H specimens filled with different TPMS lattice patterns

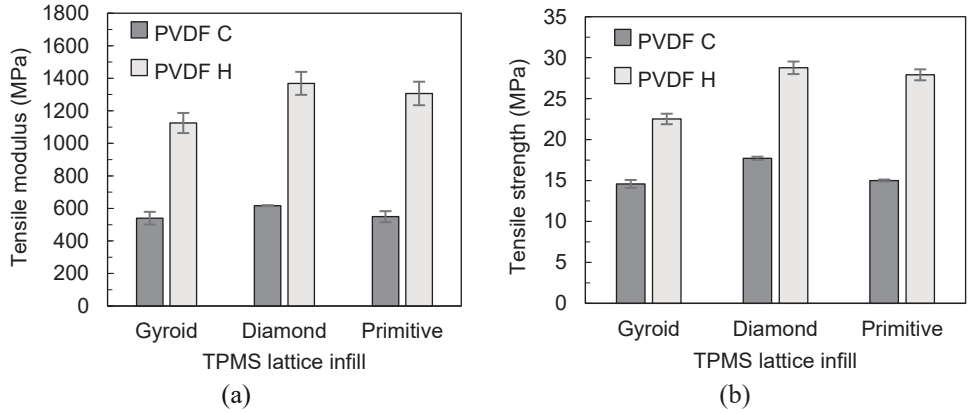

Fig. 46. Average tensile modulus and tensile strength of the specimens filled with different TPMS lattice patterns

Once the ultimate strength is reached, PVDF-C Gyroid pattern developed a plastic phase before complete break. Gyroid PVDF-H showed a semi brittle nature with narrow strain softening region. CP Gyroid pattern reported an average ultimate strength of 14.5 MPa and an average modulus of 539.8 MPa whereas Gyroid PVDF-

H reported a maximum strength of 22.5 MPa and a modulus of 1125.1 MPa. In both materials, Diamond pattern showed the highest tensile strength with 17.7 MPa and modulus with 617 MPa for PVDF-C and tensile strength with 28.7 MPa and modulus with 1368.7 MPa for PVDF-H. From the stress-strain diagrams of PVDF-C Diamond pattern, it is noted that a higher proportional region is observed followed by the ultimate stress point causing to beginning of rupture phase. None of the samples showed neck formation during any phase. In both materials, Diamond pattern showed a large linear elastic region until reaching peak stress value before rupture. PVDF-C Diamond pattern showed an elevated plastic region before fracture comparing to other patterns. The ultimate tensile strength was recorded at 17.7 MPa and a modulus of 617 MPa for PVDF-C and a strength of 28.7 MPa and 1368.7 MPa for PVDF-H.

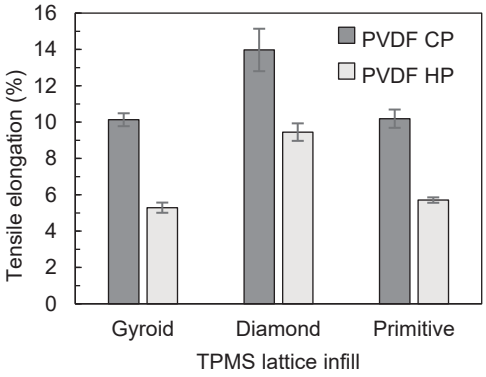

Fig. 47. Average tensile elongation of the specimens filled with TPMS lattices

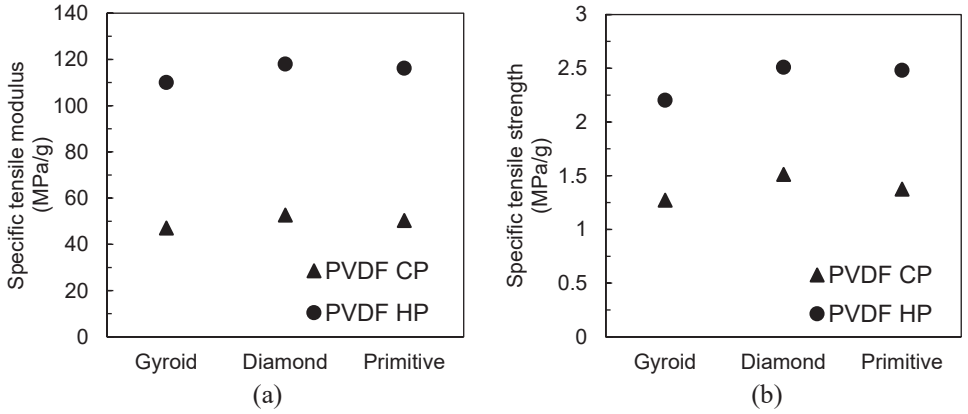

Fig. 48. (a) Specific tensile modulus, (b) specific tensile strength of the printed specimen vs TPMS lattice infill

Fig. 47 shows the tensile elongation for different TPMS patterns at maximum stress. The elongation values were determined by the gripping distance increase to the initial gripping point. The average elongation for each TPMS pattern is formulated in the graph. For all test specimens, the factors that influence the tensile elongation, such

as test velocity, load direction, and temperature, are kept uniform. Owing to better bonding between printed layers, the different patterns improved/reduced the sample stiffness and thus increased/reduced the elongation. It is evident from the graph that the ductility is higher in PVDF-C material with significant changes in elongation when printed at different TPMS pattern. The higher elongation is caused by the elastic nature of the PVDF-C material. In the case of PVDF-C, Gyroid and Primitive pattern showed a similar elongation of 10.1%. The tensile elongation of PVDF-H for Gyroid and Primitive pattern also showed a similar elongation of 5.2% and 5.7% respectively. The highest elongation was reported by Diamond pattern of 13.9% and 9.4% for PVDF-C and HP respectively.

For wider analysis of the effect of patterns on TPMS PVDF materials, specific tensile strength and modulus are evaluated and shown in Fig. 48. As seen from the graph, the largest specific tensile strength values belong to Diamond pattern in both materials and Gyroid pattern portrayed inferior specific strength. The specific tensile modulus depicted an identical diagram to that of specific strength as evident.

Flexural Properties

Flexural properties are evaluated by 3-point bending in the vertical (Y-axis) direction. The specimens are deformed until fracture and the flexural stress strain is presented in Fig. 49. The diagrams showed a linear proportional regime followed by the achievement of ultimate flexural strength followed by the crack propagation on the shell layer leading to a ductile failure behaviour. Unlike other PVDF-C patterns evaluated (Fig. 40(b)), PVDF-C TPMS patterns did not show a visible staircase effect during failure phase.

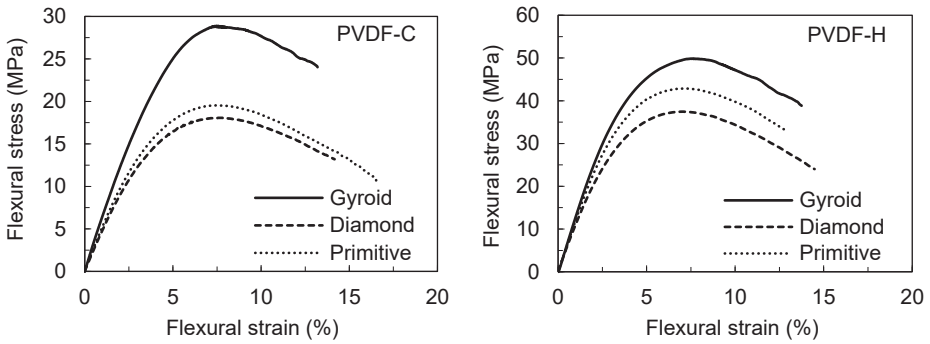

Fig. 49. Flexural stress-strain diagrams for PVDF-C and PVDF-H specimens filled with different TPMS lattice patterns

Fig. 50 presents the average flexural strength and modulus with respect to different TPMS patterns. The flexural strengths in both materials for all patterns were found to be greater than the strengths recorded in tensile loading. Gyroid pattern showed highest strength and modulus in both PVDF material. PVDF-C Diamond and Primitive pattern reported a similar strength value of 18.7 MPa and 18.6 MPa and a modulus of 503.7 MPa and 514.6 MPa respectively. PVDF-H Diamond pattern

showed a superior modulus of 1202 MPa in comparison to Primitive modulus of 892.8 MPa whereas it showed an inferior strength of 37.9 MPa comparing to 42.7 MPa strength of Primitive pattern.

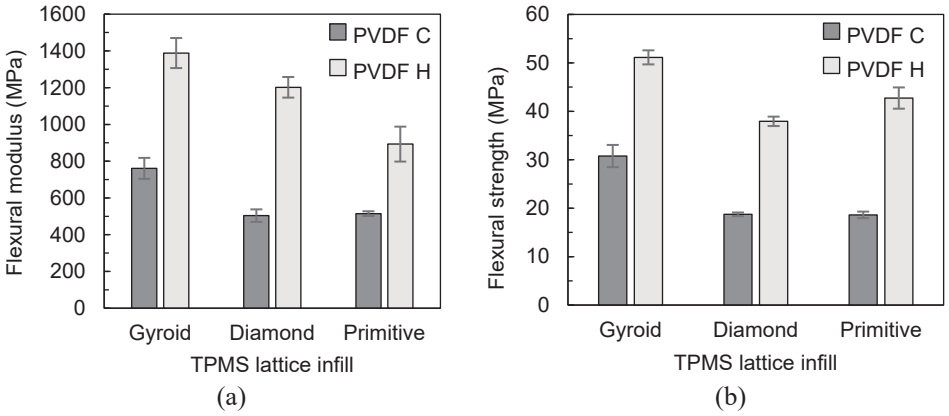

Fig. 50. (a) Average flexural modulus and (b) strength for PVDF-C and PVDF-H for different TPMS lattice infills

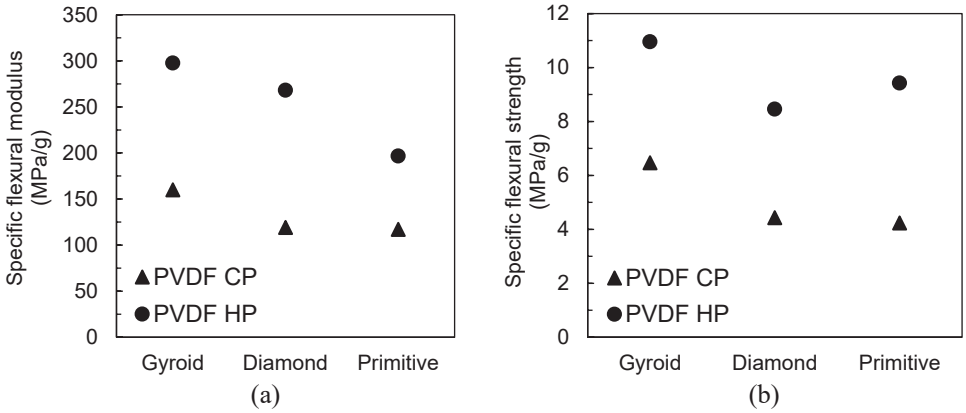

Fig. 51. (a) Specific flexural modulus, (b) specific flexural strength of the printed specimens vs TPMS lattice infill

The formulated values of specific flexural modulus and strength are depicted in Fig. 51. The results confirm that Gyroid pattern exhibited highest specific flexural strength and modulus. The difference in the specific flexural strength and modulus in regard to filling pattern shows significance in PVDF-C material.

3.7. Analysis of Raster Orientation Impact on Mechanical Properties

The strength of the components produced using FFF is known to be most influenced by the strength of the bonds between adjacent raster and layers made of these rasters. Three raster orientations were considered for the study: 0°, 45° and 90° (Fig. 52). By default, the Ultimaker printer fills with alternate raster layers of −45°

and 45° relative to the printer axis system. Raster orientation is one of the most vital printing parameters that have a notable effect on dimensional accuracy [224]. The specimens were subjected to dimensional check with digital Vernier caliper, and it could be seen that the specimen increased in the longitudinal direction by 3.5%, 4.2% and 3.4% for 0°, 45° and 90° respectively, and an increase in latitudinal direction by 0.75% for 0° and shrinkage in latitudinal by 0.75% and 0.79% for 45° and 90° for PVDF-C. Analysing the case of PVDF-H, the longitudinal increase is constant and minimum at 1% for all three orientation and shrinkage by 4% at 0° and 5.25% at 45° and 90°.

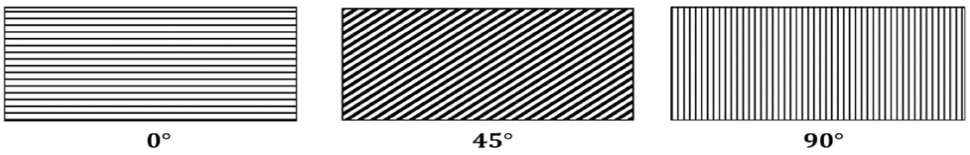

Fig. 52. Raster orientations [28]

Tensile Properties

For all three raster orientations, the specimens were 3D printed lying flat (XY) on the build platform. From the tensile stress-strain relationships shown in Fig. 53, it is observed that the PVDF-C at 0° raster orientation showed a maximum load, followed by the initiation of the plastic region before break point whereas in the case of PVDF-H, 45° orientation showed the highest elastic phase. In both materials 0° orientation described the lowest elongation. The average modulus of elasticity and tensile strength is shown in Fig. 54.

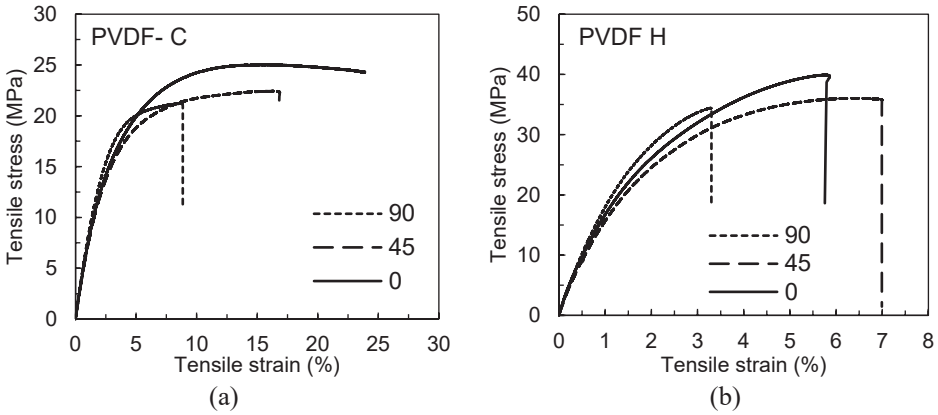

Fig. 53. Tensile stress-strain diagrams for (a) PVDF-C and (b) PVDF-H specimens printed with different raster orientation

The graph indicates that the value of tensile strength is increased at raster orientation 0° with 25.13 MPa for PVDF-C and 38.59 MPa for PVDF-H, compared with raster orientation at 90° and 45° that found the lower increment with 20.16 MPa

and 21.84 MPa, respectively, for PVDF-C and 34.20 MPa and 34.16 MPa, respectively, for PVDF-H. The behaviour of the tensile properties can be explained by the anisotropic effect of printing the specimen along with the tensile load applied during the test. Ziemian et al. [225] has reported that raster notably influence the tensile properties of the FFF specimens and their results showed that the mean of the longitudinal raster and that of the transverse raster was the most essential. The tensile strength is observed to be influenced by the subsequent directionality and directional processing of polymer molecules, suggesting an anisotropic property. Thus, the longitudinal specimens profit from the lining of molecules lengthwise the stress axis. In the case of both PVDF, 0° showed the highest strength, which is due to the alignment of layers perpendicular to the direction of loading direction. The modulus of elasticity is portrayed to be slightly higher for 90° (880.56 MPa) than 0° (821 MPa) for PVDF-C, and in the case of PVDF H, it is observed to be almost similar for 90° (2131.71 MPa) and 0° (2145.51 MPa).

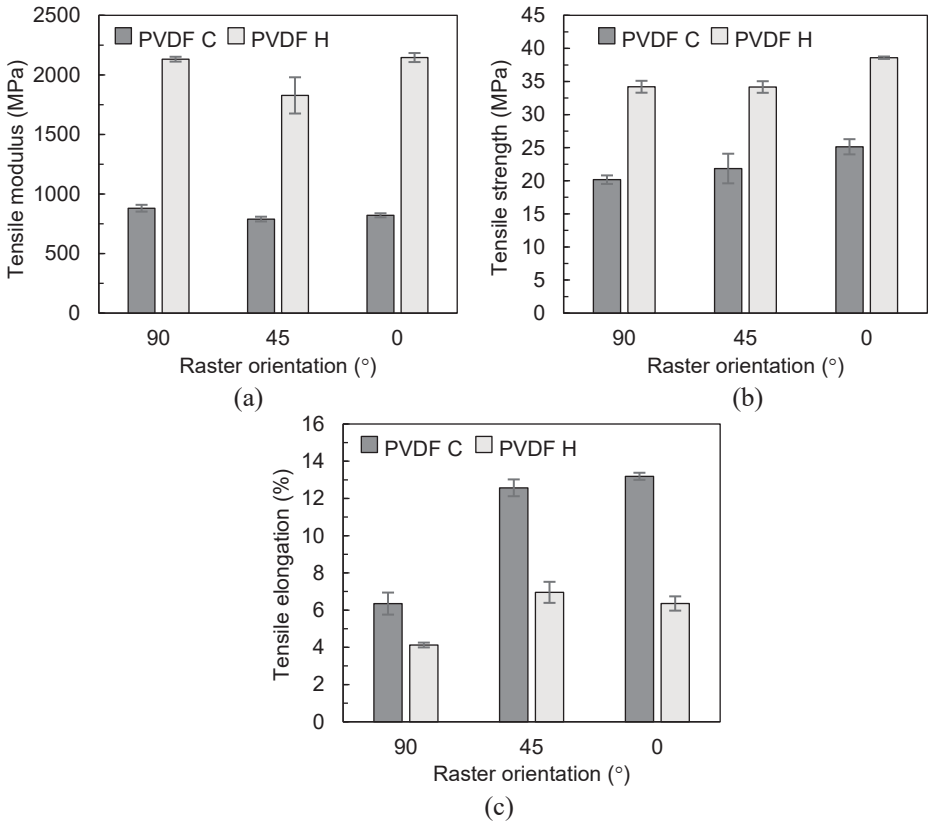

Fig. 54. Average tensile modulus (a) strength (b) and elongation (c) for PVDF-C and PVDF-H specimens printed with different raster orientations

Flexural properties

The flexural stress-strain relationships are shown in Fig. 55. It could be seen that PVDF-H at 90° attained break phase without reaching the initial elastic region. This is due to the actions of the loading force perpendicular to the raster alignment. PVDF-C at 0° showed staircase effect in reaching the ultimate value, which indicates that the raster collapsing was occurring in a nonuniform manner. This type of breaking phase is reported in the pattern of cross, cubic, concentric, and zigzag PVDF-C. At 90° raster orientation, both materials recorded the highest modulus of elasticity. The maximum flexural strength in both materials was reported at 0° (48.58 MPa for PVDF C and 79.80 MPa for PVDF-H) as shown in Fig. 56.

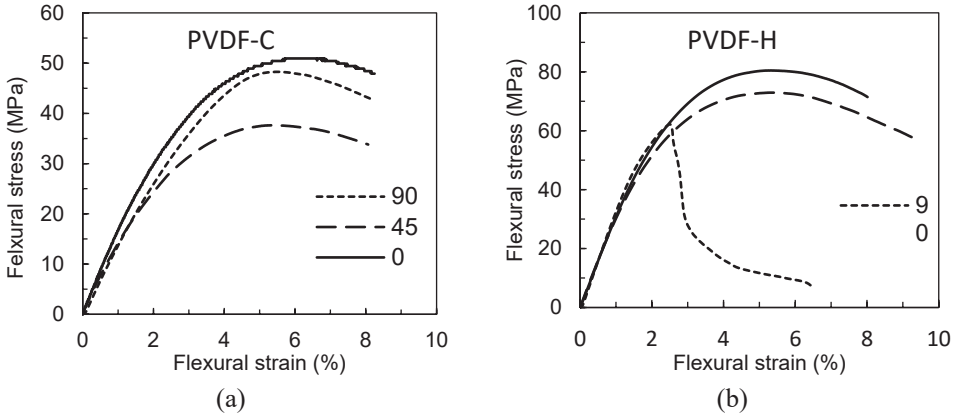

Fig. 55. Flexural stress-strain diagrams for (a) PVDF-C and (b) PVDF-H specimens printed with different raster orientation

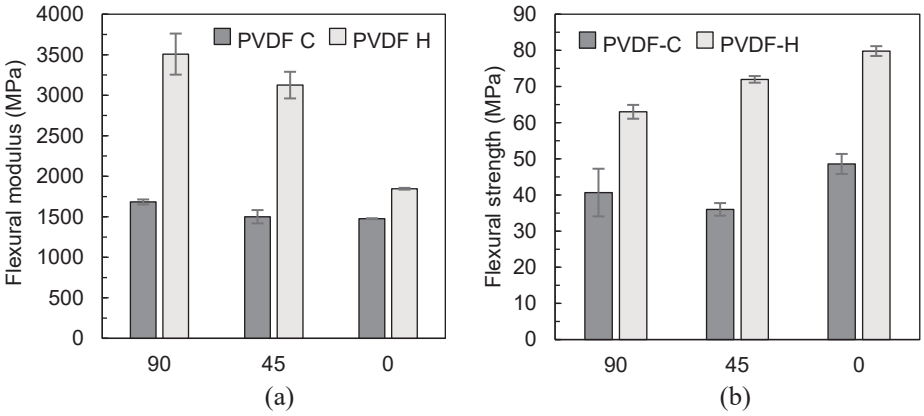

Fig. 56. Average (a) tensile modulus and (b) strength for PVDF-C and PVDF-H specimens printed with different raster orientations

3.8. Characterization of Warpage-induced Dimensional Deviations[5]

Compared to other semi-crystalline materials with higher crystallinity, FFF printed PVDF samples are highly exposed to heat shrinkage (dimensionally) and warpage. The reason for the warpage in FFF is the accumulation and relaxation of internal residual stresses when the molten filament is being deposited, its immediate cool-down and fixing. The primary reasons for deformation in FFF are unequal cooling from the melted material and heterogeneous compression [226]. It was seen that PVDF-C-ESD and PVDF-C parts were mostly deprived of warpage, whereas it was found to be fairly pronounced in PVDF-H (Fig. 57(a)). This is due to its higher crystallinity and coefficient of thermal expansion. Generally, warpage and shrinkage are regulated by a multitude of multi-aspect process-property behaviour that incorporates material properties (molecular weight, crystallization level, orientation and rate, the permeability of heat, fillers existence, etc.), part's geometry and various printing parameters. Specifically, thermal settings of the FFF process including its non-isothermal nature (defined by extrusion, platform, and chamber temperatures) have a profound effect, significantly on crystallization and ensuring shrinkage and warpage. According to PVDF grade, warpage issues may place restrictions on the form and size of parts that could be successfully built. The FFF testing detects that even if suitable adhesion of the first sedimented layers of PVDF-H is arranged, the following printing may still lead to curling of the corners and separation of the unfinished print from the printing base. Specifically, thicker PVDF homopolymer parts containing corners are prone to excessive warpage. Higher crystallinity implies higher responsiveness to shrinkage [226], while unsteady cooling at sharp edges results in differential thermal deformation that could lead to the observed distortions at the corners (Fig. 57(a)).

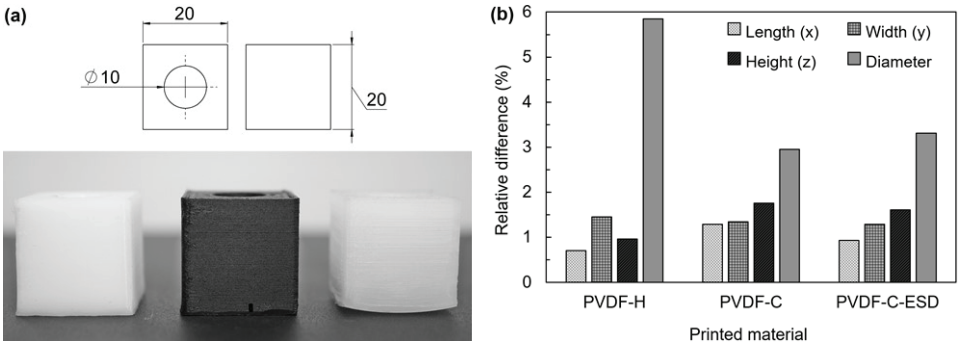

Fig. 57. (a) Design drawing of test sample (dimensions in mm) with the images of printed PVDF-C, PVDF-C-ESD and PVDF-H samples (from left to right), (b) Difference between the actual and the nominal dimensions of the samples

A study was conducted to examine the degree of shrinkage in cubic samples (3 samples) containing a clearance hole (Fig. 57(a)). The length of the sample

[5] Material in this chapter was first published in [200] by Springer Nature

corresponds to the *x*-axis of the build platform (along the direction of extrusion), width – *y*-axis, height – *z*-axis. The samples were printed bulky since, as a rule, shrinkage is maximum with higher thickness. Fig. 57(b) provides the comparison of percentage deviations from nominal dimensions, which were determined by means of coordinate measurements with Mitutoyo CRYSTA-Apex S 9106. It was found that shrinkage occurred in all the samples and all the inspected parameters indicate dimensional contraction with respect to the design specification. On average, the deviations constitute ~0.7–1.5% for the length and width, ~1–2% for the height and ~3.0–5.9% for the hole diameter. Fig. 57(b) reveals that PVDF-C-ESD and PVDF-C demonstrate comparable deviations. Meanwhile, in comparison to the copolymeric samples, the dimensional accuracy of the homopolymer sample is inferior in the case of diameter, comparable – in the case of width and slightly superior – in length and height. It is noted that among the tested materials the homopolymer exhibits the most inconsistent shrinkage results with respect to inspected dimensional parameters. Specifically, PVDF-H sample demonstrates the lowest deviation of ~0.7% (lengthwise contraction) and the highest one of ~5.9% (diametric contraction). Furthermore, the largest discrepancy between lengthwise and widthwise contractions is observed for PVDF-H, while the smallest one – for PVDF-C. Overall, such anisotropic shrinkage is expected to manifest to a lesser or greater degree in all FFF printed samples since the shrinkage in the polymer acts differently through the transverse and longitudinal directions with regards to the orientation of deposited melt strands [226].

3.9. Analysis of Piezo-signals Generated by Printed PVDF Transducers

PVDF as ferroelectric polymer may be processed (via electrical poling, mechanical stretching, etc.) to exhibit piezoelectric effect. In this chapter, direct piezoelectric effect (sensor mode) of printed PVDF transducers is evaluated and tested by measuring voltage outputs generated by 2D thin-layer and 3D bioinspired scaffold structures of PVDF and PVDF-HFP, respectively, under the applied harmonic deformation (bending or compression).

Therefore, the analysis performed in this chapter is divided into two parts. The initial poling work and piezoelectric testing was performed on thin-layer transducers based on printed and contact-poled PVDF thin films. Later, the piezoelectric testing was done on the unpoled biocompatible PVDF-HFP TPMS lattice-based cubic structures (scaffolds) subjected to cyclic compression.

Piezo-signals generated by printed thin-layer PVDF transducers

PVDF thin films (70×30 mm^2) were printed to serve as a flexible piezoelectric layer in a thin-layer piezopolymeric transducer (sensor), which was fabricated by attaching to both sides of printed PVDF thin adhesive copper films to act as electrode layers (Fig. 58). By harmonically deflecting (bending) a piezopolymeric sensor, the output voltage is measured in a mV range (Fig. 59). More specifically, the printed piezopolymeric sensor is deformed so that the mechanical stresses are induced perpendicularly to the polarization direction of PVDF film, i.e., the sensor is tested in the transverse piezoelectric operating mode (so called “d31 mode”).

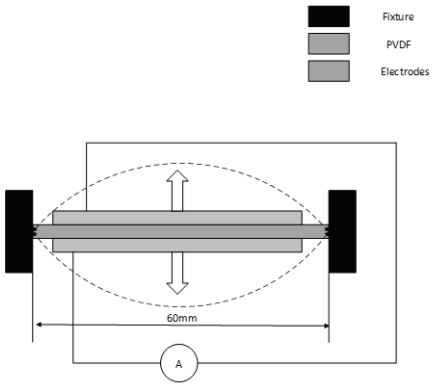

Fig. 58. Principle of piezoelectric testing method for thin-layer PVDF transducer

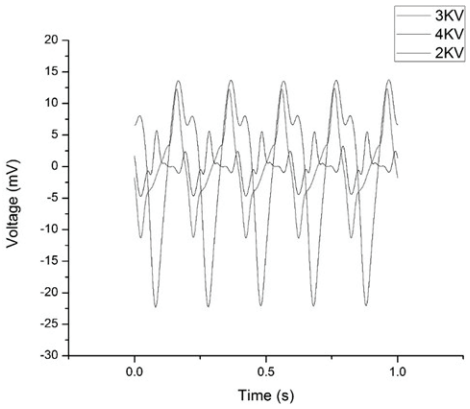

Fig. 59. Transient piezo-signals generated by printed piezopolymeric transducer (PVDF poled at different voltages)

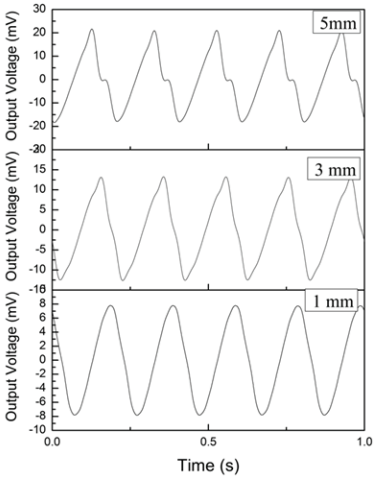

Fig. 60. Transient piezo-signals generated by printed piezopolymeric transducer at different deflection levels (PVDF film poled at 3kV)

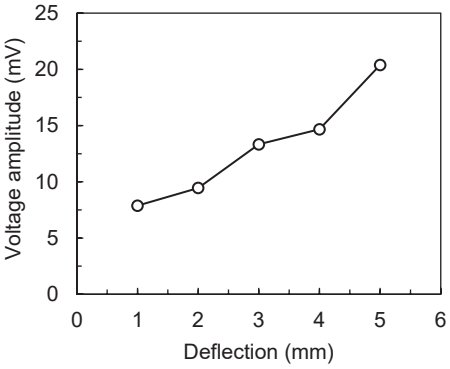

Fig. 61. Piezo-signal generated by 3D printed piezopolymeric PVDF transducer (operating in sensor mode) as a function of dynamic excitation displacement (deflection at the mid-point of the transducer)

The measurement results in Fig. 59 indicate that the higher output voltage of ~16 mV, is provided by PVDF films poled under higher electric field obtained with voltage of 4 kV. The next series of piezoelectric signal measurements was carried out by deflecting the piezopolymeric sensor within a mid-point deflection range of 1 to 5 mm (i.e., stroke of the Instron testing machine was in this range). The output voltages were recorded, and results are shown in Fig. 60 and Fig. 61. From the graphs it is evident that the higher the deflection of the sensor the higher is the piezoelectric voltage signal. For example, a piezopolymeric sensor with PVDF thin films poled (via contact poling method) at 3 kV for 60 seconds showed a 20 mV voltage at 5 mm deflection. Transient piezo-signal waveforms for 1 Hz, 10 Hz and 15 Hz are presented

in Fig. 62. As expected, increase in sensor deformation frequency (i.e. strain rate in PVDF film) leads to higher piezo-signal, which is evident in Fig. 63 showing peak voltage amplitudes recorded during harmonic deformation within a 1-15 Hz range. As the loading frequency increases, a maximum piezo-signal of 37 mV is recorded at 15 Hz (PVDF film poled at 3 kV).

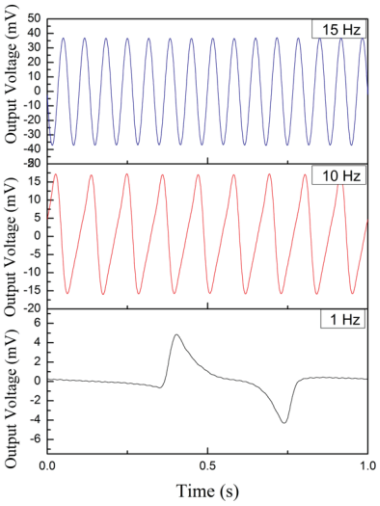

Fig. 62. Transient piezo-signals generated by printed PVDF transducer at different excitation frequencies (deflection – 3 mm)

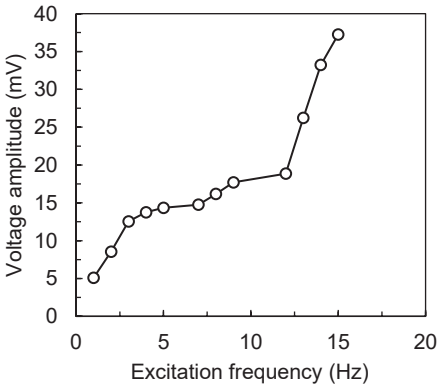

Fig. 63. Piezo-signals generated by 3D printed piezopolymeric PVDF transducer (operating in sensor mode) as a function of excitation frequency

These piezoelectric tests results indicate that by applying post-printing electrical poling in printed PVDF films, conversion from nonpolar α crystalline phase to polar β crystalline phase occurs partially, hence PVDF film starts exhibiting relatively weak piezoelectric effect. From the experiments it is observed that the stronger the applied poling electric field, the stronger the piezoelectric response is. To make these low-amplitude piezoelectric measurements more reliable, a custom transimpedance amplifier was developed at the Institute of Mechatronics.

Experimental trials with higher contact poling voltages and different poling durations were made in attempt to enhance piezoelectric response in printed PVDF films. Unfortunately, due to occurrence of dielectric breakdowns in printed thin layers it was not possible to further enhance piezoelectric properties by applying higher poling voltage (it is required to exceed very strong coercive field of PVDF). The probability of dielectric breakdowns in thin layers is further increased in the case of FFF technology since 3D printed structures intrinsically do not have a fully uniform cross section with equal thickness and, moreover, usually contain various microstructural defects – inter/intra-layer inhomogeneities (e.g. air micro-gaps), which, in turn, significantly complicate electrical poling of 3D printed structures.

Piezo-signals generated by printed PVDF-HFP bioinspired TPMS scaffolds

By using the same FFF process parameters discussed in chapter 3, the piezoelectric testing progressed with 3D printed TPMS lattice-based cubes (scaffolds) with dimensions of 20×20×20 mm^3. TPMS scaffolds were printed using in-vitro cytocompatible PVDF-HFP copolymer Fluorinar-C™ filament (Fig. 64).

(a)

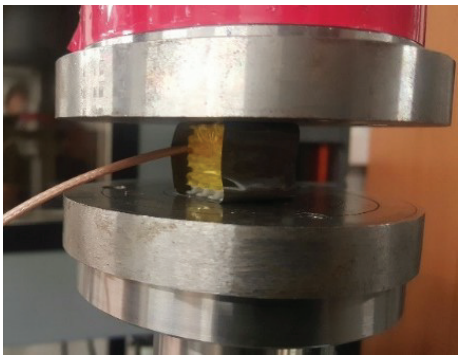

(b)

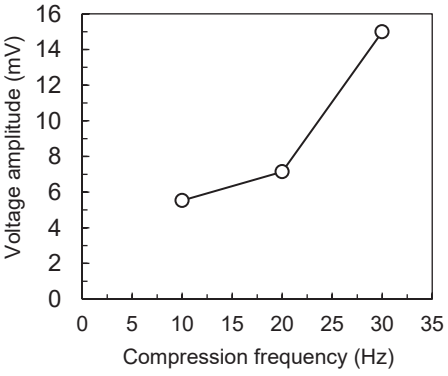

(c)

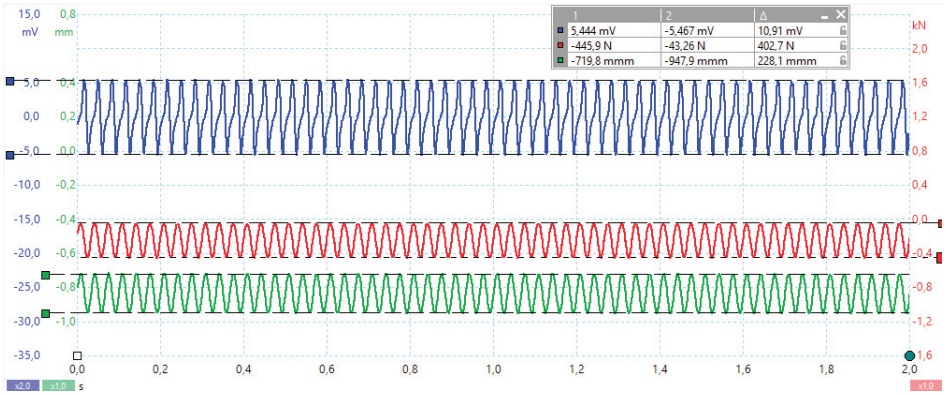

(d)

Fig. 64. (a) Examples of printed TPMS scaffolds using biocompatible PVDF-HFP. (b) TPMS scaffold with electrodes during compression testing. (c) Piezo-signals generated by 3D printed unpoled TPMS scaffold harmonically deformed at different frequencies. (d) Harmonic piezo-voltage signal (blue waveform at the top) of the TPMS scaffold during applied compression at 30 Hz (green waveform at the bottom)

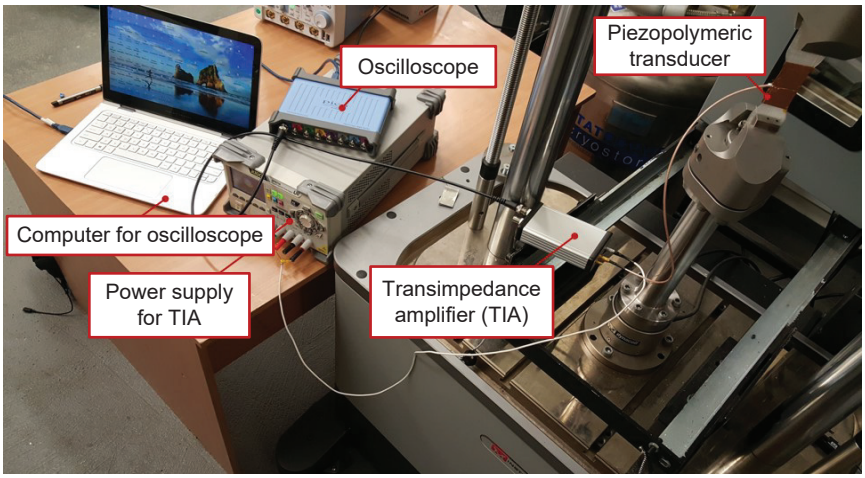

Fig. 65. Electromechanical testing setup for measuring piezo-signals generated by 3D printed piezopolymeric transducers under cyclic uniaxial loading

Initially Gyroid architecture was chosen because it is widely used pattern for biomedical applications. To assess the effect of porosity, the structures are printed at 20% infill density. These dimensions are chosen to satisfy the critical lattice condition [227]. The pattern is printed by removing the shell/wall layers, to test the influence of the pattern directly. From the slicing point of view, the concern was focused on the build-up of layers without collapsing, therefore, the layers were printed with a thin brim layer which corresponds to the thickness of the first layer (Fig. 64(a)). The purpose of implementing this method is to have a base layer for proper adhesion and could be removed along with brim layer. The surface of the sample was treated with an alcohol to remove grease. The electrode was implemented using two types of conductive tapes: one of them electrically conductive double-sided tape from 3M Electronic Specialty, another one was copper tape with double coated electrically conductive adhesive from Agar Scientific. The electrode was shielded with the one side adhesive coper tape which was connected to signal ground. The electrodes are placed in the form of copper tapes and soldered to the coaxial cable. A shielding layer is implemented to the part and connected to the ground of the coaxial cable for avoiding unwanted noise signals.

Gyroid scaffolds were subjected to a harmonic compressive loading (Fig. 64(b)) and the generated piezo-voltage signals were recorded by the digital oscilloscope via the transimpedance amplifier (Fig. 65). The excitation was done at three levels of frequency in a 10–30 Hz range. At 10 Hz excitation, a voltage signal of ~6 mV peak-to-peak amplitude was recorded, while at 30 Hz the signal of ~15 mV was recorded. During this electromechanical testing a pre-stress of 0.25 kN was used (the pre-stress influences the generated piezo-signals).

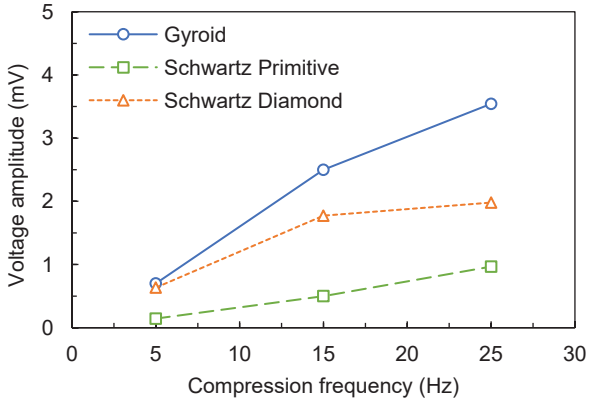

Fig. 66. Piezo-signal generated by 3D printed unpoled PVDF-HFP bioinspired TPMS scaffold structures vs cyclic compression frequency

Furthermore, a study was conducted to compare the electrical response of three well-known TPMS lattice types – Schwarz Primitive, Schwarz Diamond and Gyroid. All the samples were printed with 30% infill satisfying the critical lattice condition. The samples were subjected to a prestress of 0.25 kN and the excitation was done at 5 Hz, 15 Hz and 25 Hz. From the Fig. 66, it is evident that the Gyroid demonstrates the highest electrical response at 25 Hz (3.5 mV), followed by Schwarz Primitive (1.98 mV) and Schwarz Diamond (0.96 mV). The presence of piezoelectric effect in these bioinspired scaffolds is a novel and interesting result of this research work since it suggests that the biocompatible PVDF-HFP copolymer could be potentially used to fabricate electroactive (electrostimulating) bioscaffolds with predefined favourable TPMS-based topology for tissue engineering applications.

3.10. Chapter Conclusions

The printability study was done in an open-chamber FFF printer and revealed that pristine and composite PVDF-C components can be successfully printed in different geometries with a common readily available 3D printer. Meanwhile, PVDF-H printing is followed by issues of adhesion and warpage, which creates limitations in terms of printable part designs and resulting dimensional accuracy. The use of slightly lower extrusion temperatures (~230°C), lower printing speeds (~20 mm/s), inclusion of wider brims into prints and covering the platform with FFF-adapted specialized adhesive are general recommendations for raising the chance of obtaining complete and less distorted PVDF prints.

The mechanical test results show discernible variations in strength and elastic performance between tension, compression, and bending of the printed PVDF-based materials. Moderately ductile, ductile and near-brittle material responses are exhibited in the 100% filled PVDF-H, PVDF-C, and PVDF-C-ESD specimens. In terms of tensile, compressive, and flexural strengths, the homopolymer is found to outperform the copolymeric equivalents at all infill densities. Concentric, cross, cubic, lines, octet, triangle, and zigzag are the patterns evaluated for PVDF-H and PVDF-C. The latter

showed high levels of elongation compared to PVDF-H and concentric pattern showed a higher linear elastic region until reaching peak stress value, and cross pattern showed the lowest linear elastic region. For tensile case, the concentric pattern provided the highest strength which could be related to strut aligning with the load direction. The specimens with the cross pattern resulted in inferior properties in tensile loading and showed a superior strength under flexural loading. This shows that the cross pattern exhibits resistance to deformation in the vertical direction.

Printed PVDF thin films were successfully poled in contact mode under moderately strong kV-level voltage to impart piezoelectric response, thereby producing piezopolymeric transducers. The electromechanical experiments indicate that the higher the poling voltage, the stronger mV-level piezo-signals are generated when the piezopolymeric transducer is dynamically deformed under mm-level displacements and low frequencies in 1–15 Hz range. It was found that increasing harmonic deformation amplitudes and frequency leads to higher piezo-signals in tested piezopolymeric transducers. Furthermore, unpoled TPMS scaffolds printed with biocompatible Fluorinar-C™ PVDF-HFP were subjected to dynamic 5–25 Hz compression and it was observed that Gyroid scaffold exhibited the highest piezo-signal of several mV, while the Schwarz Primitive – the lowest one.

4. CONCLUSIONS

1. A detailed analysis of the study area identified that it is very difficult to print in open-chamber 3D printers geometrically accurate parts with semi-crystalline hydrophobic thermoplastics having high CTE. PVDF filaments were commercially introduced very recently and there is a lack of published data on the most suitable manufacturing conditions to counteract PVDF tendency to warp and detach from the build platform in open-air FFF environment. It was found that there are no published works on the strength and elastic properties of lightweight PVDF cellular structures subjected to different deformation regimes, e.g. tension, compression and bending. Limited published results indicate that it is difficult to adapt FFF process to print PVDF and PVDF-HFP transducers having strong piezoelectric properties.
2. Numerous PVDF printing tests were performed with different FFF process conditions which revealed strong print warpage and weak adhesion when printing PVDF in an open-chamber environment. More significant warpage is observed in thicker angular homopolymer prints where deviations from nominal dimensions reach ~6%. The dimensional accuracy of the copolymeric prints is better with deviations below ~3.5%. It was determined that warpage and adhesion issues are minimized by: i) using lower printing speeds (not higher than ~20 mm/s); ii) using lower extrusion temperatures (~230°C) within the melt processing temperature range that is typical for PVDF (~200°C–260°C). In addition, it was found that incomplete prints due to detachment may be prevented more effectively by: i) using brim layers of at least ~6–8 mm for increasing print/platform contact area; ii) applying on the platform a specialized FFF-adapted adhesive layer.
3. CAD/CAM process workflow, based on the use of SolidWorks and Ultimaker Cura print slicing software, was effectively applied to design and pre-process cellular PVDF specimens for consistent 3D printing in order to obtain reliable experimental results regarding the influence of lightweight on mechanical properties. In total, no less than 500 specimens were pre-processed in Cura and successfully printed in Ultimaker 2+ by using 7 standard strut-type infills and 3 bioinspired sheet-type infills based on minimal surfaces (TPMS), including variable density (25%–75%) configurations. The most popular TPMS infill patterns (Gyroid, Schwarz Diamond, and Primitive) were integrated into the Cura slicer and pre-processed in order to print lightweight PVDF homopolymer and cytocompatible copolymer parts with bioinspired infills, which are important for biomedical structural applications (e.g. orthopaedic implants, bioscaffolds, etc.).
4. Mechanical tests based on ISO 527-2, ISO 604, and ISO 178 standards were performed to determine dependences of strength and elastic properties of cellular PVDF specimens on variable infill density and pattern under quasi-static tension, compression, and bending, respectively. Tensile experiments demonstrate moderately ductile, ductile and near-brittle material response in

the 100% filled PVDF, PVDF-HFP, and PVDF-HFP/graphene composite specimens, respectively. There is a large difference in ductility between the 100% filled PVDF-HFP and the composite, which means that the design of multi-material ESD-safe part (PVDF-HFP with static-dissipative composite layers) should be approached with care to prevent failure. It is found that the triangular infill reduces tensile strength and ductility in the homopolymer specimens more significantly than in the copolymeric ones. It is noted that tension-compression asymmetry in the 3D printed specimens is larger (strength differential up to ~3.4 at 75% infill) as compared to common (e.g. moulded) thermoplastics (up to ~1.8). The presence of the asymmetry (i.e. anisotropic behaviour) justifies the importance of testing printed parts not only in tension as it is commonly done in the FFF community. Fortunately, the asymmetry in cellular PVDF parts is found to decrease with lower infill density (below 2 at 25% infill). Lower infill density also leads to a decrease in tension-compression elastic anisotropy, which is found to be larger in the PVDF/graphene composite. The influence of different standard infill patterns on mechanical properties is more significant in tension than in bending. Specimens printed with concentric infill have the highest tensile strength of ~33 MPa and ~20 MPa for PVDF and PVDF-HFP, respectively. For PVDF, the tensile strength of a part with the concentric infill may be ~30%–140% larger than for other infill patterns. PVDF specimens printed with the bioinspired Schwarz Diamond and Primitive infills at 75% density have the highest tensile strength of ~28–29 MPa, respectively, while parts with Gyroid infill – the highest flexural strength of 51 MPa. For PVDF-HFP, the tensile strength values are comparable (~15–18 MPa), while flexural strength is the highest for the Gyroid infill (~31 MPa) and comparable for the Schwarz Diamond and Primitive (~19 MPa).

5. 3D printed PVDF structures were subjected to contact poling at 3–4 kV to produce piezoelectric PVDF films. An experimental dynamic test setup with an in-house built transimpedance amplifier was created for more reliable measurements of small piezo-signals (voltage outputs) of printed PVDF transducers. Printed and poled thin-layer PVDF sensors generate up to ~30 mV piezo-signals under harmonic excitation at 15 Hz and the output increases with excitation frequency and amplitude. At ultra-low excitations of several Hz, the printed sensors generate several mV, which could be possibly adapted for biomechanical sensing applications. Due to dielectric breakdowns in printed PVDF layers, it was not possible to further enhance piezoelectric properties by applying higher poling voltage that is required to exceed the very strong coercive field of PVDF. It is noted that unpoled TPMS scaffolds printed with cytocompatible PVDF-HFP can generate small mV-level piezo-signals under 5–25 Hz cyclic compression. It confirms that this PVDF copolymer could be possibly adapted for rapid fabrication of electrostimulating bioscaffolds with predefined cellular design for tissue engineering applications.

5. REFERENCES

1. CHAPIRO, Michael. Current achievements and future outlook for composites in 3D printing. *Reinforced Plastics*. 2016.
2. NIAKI, Mojtaba Khorram, TORABI, S. Ali and NONINO, Fabio. Why manufacturers adopt additive manufacturing technologies: The role of sustainability. *Journal of Cleaner Production*. 2019.
3. GONZÁLEZ-HENRÍQUEZ, Carmen M., SARABIA-VALLEJOS, Mauricio A. and RODRIGUEZ-HERNANDEZ, Juan. *Polymers for additive manufacturing and 4D-printing: Materials, methodologies, and biomedical applications*. 2019.
4. OLIVEIRA, J., CORREIA, V., CASTRO, H., MARTINS, P. and LANCEROS-MENDEZ, S. *Polymer-based smart materials by printing technologies: Improving application and integration*. 2018.
5. TOFAIL, Syed A.M., KOUMOULOS, Elias P., BANDYOPADHYAY, Amit, BOSE, Susmita, O'DONOGHUE, Lisa and CHARITIDIS, Costas. *Additive manufacturing: scientific and technological challenges, market uptake and opportunities*. 2018.
6. GORDELIER, Tessa Jane, THIES, Philipp Rudolf, TURNER, Louis and JOHANNING, Lars. Optimising the FDM additive manufacturing process to achieve maximum tensile strength: a state-of-the-art review. *Rapid Prototyping Journal*. 2019. Vol. 25, no. 6, p. 953–971.
7. BANDYOPADHYAY, Amit and HEER, Bryan. *Additive manufacturing of multi-material structures*. 2018.
8. GORDELIER, Tessa Jane, THIES, Philipp Rudolf, TURNER, Louis and JOHANNING, Lars. *Optimising the FDM additive manufacturing process to achieve maximum tensile strength: a state-of-the-art review*. 2019.
9. DE LEON, Al C., CHEN, Qiyi, PALAGANAS, Napolabel B., PALAGANAS, Jerome O., MANAPAT, Jill and ADVINCULA, Rigoberto C. *High performance polymer nanocomposites for additive manufacturing applications*. 2016.
10. WANG, Xin, JIANG, Man, ZHOU, Zuowan, GOU, Jihua and HUI, David. *3D printing of polymer matrix composites: A review and prospective*. 2017.
11. The Ultimate Guide to Stereolithography (SLA) 3D Printing (Updated for 2019). *Formlabs*. 2020.
12. MACDONALD, Eric, SALAS, Rudy, ESPALIN, David, PEREZ, Mireya, AGUILERA, Efrain, MUSE, Dan and WICKER, Ryan B. 3D printing for the rapid prototyping of structural electronics. *IEEE Access*. 2014.
13. FORD, Sharon L N. Additive Manufacturing Technology : Potential Implications for U.S. Manufacturing Competitiveness. *Journal of International Commerce and Economics (USA)*. 2014.
14. STANSBURY, Jeffrey W. and IDACAVAGE, Mike J. 3D printing with polymers: Challenges among expanding options and opportunities. In : *Dental Materials*. 2016.
15. SACCO, Enea and MOON, Seung Ki. Additive manufacturing for space: status and promises. *International Journal of Advanced Manufacturing Technology*. 2019.
16. JUDY CEULEMANS, YANN MÉNIÈRE, ALIKI NICHOGIANNOPOULOU, JAVIER POSE RODRÍGUEZ, Ilja Rudyk (EPO)European Patent Office. Patents and additive manufacturing. 2020.
17. WOHLERS, T, (FIRM), Wohlers Associates, CAMPBELL, I, DIEGEL, O, HUFF, R and KOWEN, J. *Wohlers Report 2020: 3D Printing and Additive Manufacturing State of the Industry* [online]. Wohlers Associates, 2020. ISBN 9780991333264. Available from: https://books.google.lt/books?id=sRG7zQEACAAJ

18. KENNETH WONG. Wohlers 2017 Report on 3D Printing Industry Points to Softened Growth - Rapid Ready Technology. *Wohlers Associates*. 2017.

19. ISO/ASTM. ISO/ASTM 52900: Additive manufacturing - General principles - Terminology. *International Standard*. 2015. ISBN 0580919374; 9780580919374

20. SANDRINE TRANCHARD, Vivienne Rojas. MANUFACTURING OUR 3D FUTURE. *ISO* [online]. 5 May 2015. Available from: https://www.iso.org/news/2015/05/Ref1956.html

21. L. WILLIAMS. *Additive Manufacturing or 3D Scanning and Printing Manufacturing Engineering Handbook*. 2nd. McGraw-Hill Education, 2016.

22. GAO, Wei, ZHANG, Yunbo, RAMANUJAN, Devarajan, RAMANI, Karthik, CHEN, Yong, WILLIAMS, Christopher B., WANG, Charlie C.L., SHIN, Yung C., ZHANG, Song and ZAVATTIERI, Pablo D. The status, challenges, and future of additive manufacturing in engineering. *CAD Computer Aided Design*. 2015.

23. KAZMER, David. Three-Dimensional Printing of Plastics. In : *Applied Plastics Engineering Handbook: Processing, Materials, and Applications: Second Edition*. 2017. ISBN 9780323390408.

24. LEE, Jian Yuan, AN, Jia and CHUA, Chee Kai. *Fundamentals and applications of 3D printing for novel materials*. 2017.

25. ZAMAN, Uzair Khaleeq uz, BOESCH, Emilien, SIADAT, Ali, RIVETTE, Mickael and BAQAI, Aamer Ahmed. Impact of fused deposition modeling (FDM) process parameters on strength of built parts using Taguchi's design of experiments. *International Journal of Advanced Manufacturing Technology*. 2019.

26. DIZON, John Ryan C., ESPERA, Alejandro H., CHEN, Qiyi and ADVINCULA, Rigoberto C. Mechanical characterization of 3D-printed polymers. *Additive Manufacturing* [online]. 2018. Vol. 20, p. 44–67.

27. COOGAN, Timothy J. and KAZMER, David O. Healing simulation for bond strength prediction of FDM. *Rapid Prototyping Journal*. 2017.

28. DEY, Arup and YODO, Nita. A systematic survey of FDM process parameter optimization and their influence on part characteristics. *Journal of Manufacturing and Materials Processing*. 2019. Vol. 3, no. 3.

29. LETCHER, Todd, RANKOUHI, Behzad and JAVADPOUR, Sina. Experimental study of mechanical properties of additively manufactured abs plastic as a function of layer parameters. *ASME International Mechanical Engineering Congress and Exposition, Proceedings (IMECE)*. 2015. Vol. 2A-2015, no. November. ISBN 9780791857359

30. DURGUN, Ismail and ERTAN, Rukiye. Experimental investigation of FDM process for improvement of mechanical properties and production cost. *Rapid Prototyping Journal*. 2014. Vol. 20, no. 3, p. 228–235.

31. RANEY, Kyle, LANI, Eric and KALLA, Devi K. Experimental characterization of the tensile strength of ABS parts manufactured by fused deposition modeling process. *Materials Today: Proceedings*. 2017. Vol. 4, no. 8, p. 7956–7961.

32. NANCHARAIAH, Tata, RAJU, D Ranga and RAJU, V Ramachandra. An experimental investigation on surface quality and dimensional accuracy of FDM components. *International Journal on Emerging Technologies*. 2010.

33. NIDAGUNDI, Vijay B., KESHAVAMURTHY, R. and PRAKASH, C. P.S. Studies on Parametric Optimization for Fused Deposition Modelling Process. *Materials Today: Proceedings*. 2015. Vol. 2, no. 4–5, p. 1691–1699.

34. SOOD, Anoop K., OHDAR, Raj K. and MAHAPATRA, Siba S. Experimental investigation and empirical modelling of FDM process for compressive strength improvement. *Journal of Advanced Research* [online]. 2012. Vol. 3, no. 1, p. 81–90.

35. NANCHARAIAH, T. Optimization of Process Parameters in FDM Process Using Design of Experiments. *International Journal on Emerging Technologies 2(1):* 2011.

36. RAYEGANI, Farzad and ONWUBOLU, Godfrey C. Fused deposition modelling (fdm) process parameter prediction and optimization using group method for data handling (gmdh) and differential evolution (de). *International Journal of Advanced Manufacturing Technology*. 2014. Vol. 73, no. 1–4, p. 509–519.

37. RAO, R. Venkata and RAI, Dhiraj P. Optimization of fused deposition modeling process using teaching-learning-based optimization algorithm. *Engineering Science and Technology, an International Journal*. 2016.

38. HARSHITHA, V. and RAO, Seeram Srinivasa. Design and analysis of ISO standard bolt and nut in FDM 3D printer using PLA and ABS materials. In : *Materials Today: Proceedings*. Elsevier Ltd, 1 January 2019. p. 583–588.

39. HARSHITHA, V. and RAO, Seeram Srinivasa. Design and analysis of ISO standard bolt and nut in FDM 3D printer using PLA and ABS materials. In : *Materials Today: Proceedings*. 2019.

40. ROHDE, S., CANTRELL, J., JEREZ, A., KROESE, C., DAMIANI, D., GURNANI, R., DISANDRO, L., ANTON, J., YOUNG, A., STEINBACH, D. and IFJU, P. Experimental Characterization of the Shear Properties of 3D–Printed ABS and Polycarbonate Parts. *Experimental Mechanics*. 2018.

41. PAVAN KUMAR, G. and REGALLA, Srinivasa Prakash. Optimization of support material and build time in fused deposition modeling (FDM). In : *Applied Mechanics and Materials*. 2012.

42. ANG, Ker Chin, LEONG, Kah Fai, CHUA, Chee Kai and CHANDRASEKARAN, Margam. Investigation of the mechanical properties and porosity relationships in fused deposition modelling-fabricated porous structures. *Rapid Prototyping Journal*. 2006.

43. JAMI, Hesamodin, MASOOD, S. H. and SONG, W. Q. Dynamic response of FDM made ABS parts in different part orientations. In : *Advanced Materials Research*. 2013.

44. FERNANDES, Joao, DEUS, Augusto M., REIS, Luis, VAZ, Maria Fatima and LEITE, Marco. Study of the influence of 3D printing parameters on the mechanical properties of PLA. In : *Proceedings of the International Conference on Progress in Additive Manufacturing*. 2018.

45. TORRES, Jonathan, COTELO, José, KARL, Justin and GORDON, Ali P. Mechanical property optimization of FDM PLA in shear with multiple objectives. *JOM*. 2015.

46. PENG, Anhua, XIAO, Xingming and YUE, Rui. Process parameter optimization for fused deposition modeling using response surface methodology combined with fuzzy inference system. *International Journal of Advanced Manufacturing Technology*. 2014.

47. WU, Junhui. Study on optimization of 3D printing parameters. In : *IOP Conference Series: Materials Science and Engineering*. 2018.

48. NIDAGUNDI, Vijay B., KESHAVAMURTHY, R. and PRAKASH, C. P.S. Studies on Parametric Optimization for Fused Deposition Modelling Process. *Materials Today: Proceedings* [online]. 2015. Vol. 2, no. 4–5, p. 1691–1699.

49. AHN, Daekeon, KWEON, Jin Hwe, KWON, Soonman, SONG, Jungil and LEE, Seokhee. Representation of surface roughness in fused deposition modeling. *Journal of Materials Processing Technology*. 2009.

50. CHACÓN, J. M., CAMINERO, M. A., GARCÍA-PLAZA, E. and NÚÑEZ, P. J. Additive manufacturing of PLA structures using fused deposition modelling: Effect of process parameters on mechanical properties and their optimal selection. *Materials and Design*. 2017. Vol. 124, p. 143–157.

51. LUCAS CAROLO. 3D Printer Nozzle Guide: What to Know & Which to Buy. . 2020.

52. DEZAKI, Mohammadreza Lalegani and MOHD ARIFFIN, Mohd Khairol Anuar. The effects of combined infill patterns on mechanical properties in fdm process. *Polymers*. 2020.

53. DAVE, Harshit K., PATADIYA, Naushil H., PRAJAPATI, Ashish R. and RAJPUROHIT, Shilpesh R. Effect of infill pattern and infill density at varying part orientation on tensile properties of fused deposition modeling-printed poly-lactic acid part. *Proceedings of the Institution of Mechanical Engineers, Part C: Journal of Mechanical Engineering Science*. 2019.

54. POPESCU, Diana, ZAPCIU, Aurelian, AMZA, Catalin, BACIU, Florin and MARINESCU, Rodica. FDM process parameters influence over the mechanical properties of polymer specimens: A review. *Polymer Testing*. 2018. Vol. 69, no. May, p. 157–166.

55. SHIRKE, Aniket, CHOUDHARI, Chandrashekhar and RUKHANDE, Sanjay. Parametric Optimization of Fused Deposition Modelling (FDM) Process Using PSO Algorithm. *SSRN Electronic Journal*. 2018.

56. SIN, Lee Tin, RAHMAT, Razak Rahmat and RAHMAN, Wan Azian Wan Abdul. *Polylactic Acid: PLA Biopolymer Technology and Applications*. 2012. ISBN 9781437744590.

57. LIGON, Samuel Clark, LISKA, Robert, STAMPFL, Jürgen, GURR, Matthias and MÜLHAUPT, Rolf. *Polymers for 3D Printing and Customized Additive Manufacturing*. 2017.

58. SINGH, Sunpreet, PRAKASH, Chander and RAMAKRISHNA, Seeram. *3D printing of polyether-ether-ketone for biomedical applications*. 2019.

59. BRUNO AMEDURI, Hideo Sawada. PVDF Resins for porous membranes. In : *Fluorinated Polymers: Applications– Volume 2*. 2016. p. 139.

60. BURNHAM-FAY, Ethan D., LE, Tue, TARBUTTON, Joshua A. and ELLIS, Jonathan D. Strain characteristics of additive manufactured polyvinylidene fluoride (PVDF) actuators. *Sensors and Actuators, A: Physical* [online]. 2017. Vol. 266, p. 85–92.

61. ESPALIN, David, MACDONALD, Eric, MUSE, Danny W, WICKER, Ryan B, MUSE, D W, MACDONALD, E, ESPALIN, D, WICKER, R B, KECK, W M, ADV, Int J and TECHNOL, Manuf. 3D Printing multifunctionality: Structures with electronics Antenna Design View project IOT for Casting View project 3D Printing multifunctionality: structures with electronics. *Article in International Journal of Advanced Manufacturing Technology*. 2014. ISBN 0017001457177

62. LAROCHE, Gaétan, MAROIS, Yves, GUIDOIN, Robert, KING, Martin W., MARTIN, Louisette, HOW, Thien and DOUVILLE, Yvan. Polyvinylidene fluoride (PVDF) as a biomaterial: From polymeric raw material to monofilament vascular suture. *Journal of Biomedical Materials Research*. 1995.

63. KANG, Guo dong and CAO, Yi ming. *Application and modification of poly(vinylidene fluoride) (PVDF) membranes - A review*. 2014.

64. RATHOD, V. T., MAHAPATRA, D. Roy, JAIN, Anjana and GAYATHRI, A. Characterization of a large-area PVDF thin film for electro-mechanical and ultrasonic sensing applications. *Sensors and Actuators, A: Physical*. 2010.

65. JEON, Jin Han, KANG, Seong Pal, LEE, Sunwoo and OH, Il Kwon. Novel biomimetic actuator based on SPEEK and PVDF. *Sensors and Actuators, B: Chemical*. 2009.

66. JIANG, Yonggang, SHIONO, Syohei and HAMADA, Hiroyuki. Low-frequency energy harvesting using a laminated PVDF cantilever with a magnetic mass. *Proc. PowerMEMS*. 2010.

67. ARKEMA. Kynar® PVDF Fluoropolymer Family. . 2014.
68. KIRKPATRICK, Max B., TARBUTTON, Joshua A., LE, Tue and LEE, Chabum. Characterization of 3D printed piezoelectric sensors: Determiniation of d33 piezoelectric coefficient for 3D printed polyvinylidene fluoride sensors. In : *Proceedings of IEEE Sensors*. 2017.
69. CARDOSO, Vanessa F., CORREIA, Daniela M., RIBEIRO, Clarisse, FERNANDES, Margarida M. and LANCEROS-MÉNDEZ, Senentxu. *Fluorinated polymers as smart materials for advanced biomedical applications*. 2018.
70. TANDON, Biranche, BLAKER, Jonny J. and CARTMELL, Sarah H. Piezoelectric materials as stimulatory biomedical materials and scaffolds for bone repair. *Acta Biomaterialia* [online]. 2018. Vol. 73, p. 1–20.
71. NUNES-PEREIRA, J., RIBEIRO, S., RIBEIRO, C., GOMBEK, C. J., GAMA, F. M., GOMES, A. C., PATTERSON, D. A. and LANCEROS-MÉNDEZ, S. Poly(vinylidene fluoride) and copolymers as porous membranes for tissue engineering applications. *Polymer Testing*. 2015. Vol. 44, p. 234–241.
72. SHEPELIN, Nick A., GLUSHENKOV, Alexey M., LUSSINI, Vanessa C., FOX, Phillip J., DICINOSKI, Greg W., SHAPTER, Joseph G. and ELLIS, Amanda V. New developments in composites, copolymer technologies and processing techniques for flexible fluoropolymer piezoelectric generators for efficient energy harvesting. *Energy and Environmental Science* [online]. 2019. Vol. 12, no. 4, p. 1143–1176.
73. RIBEIRO, Clarisse, COSTA, Carlos M., CORREIA, Daniela M., NUNES-PEREIRA, João, OLIVEIRA, Juliana, MARTINS, Pedro, GONÇALVES, Renato, CARDOSO, Vanessa F. and LANCEROS-MÉNDEZ, Senentxu. Electroactive poly(vinylidene fluoride)-based structures for advanced applications. *Nature Protocols* [online]. 2018. Vol. 13, no. 4, p. 681–704.
74. CARDOSO, V. F., KNOLL, T., VELTEN, T., REBOUTA, L., MENDES, P. M., LANCEROS-MÉNDEZ, S. and MINAS, G. Polymer-based acoustic streaming for improving mixing and reaction times in microfluidic applications. *RSC Advances*. 2014.
75. ASMAALMAZROUEI. Robust Surface-Engineered TapeCast and Extrusion Methods to Fabricate Electrically-Conductive Poly(vinylidene fuoride)/Carbon Nanotube Filaments for CorrosionResistant 3D Printing Applications. *Nature*. 2019.
76. KIM, Hoejin, JOHNSON, Jeffrey, CHAVEZ, Luis A., GARCIA ROSALES, Carlos A., TSENG, Tzu Liang Bill and LIN, Yirong. Enhanced dielectric properties of three phase dielectric MWCNTs/BaTiO3/PVDF nanocomposites for energy storage using fused deposition modeling 3D printing. *Ceramics International*. 2018. Vol. 44, no. 8, p. 9037–9044.
77. KIM, Hoejin, FERNANDO, Torres, LI, Mingyue, LIN, Yirong and TSENG, Tzu Liang Bill. Fabrication and characterization of 3D printed BaTiO3/PVDF nanocomposites. *Journal of Composite Materials*. 2018. Vol. 52, no. 2, p. 197–206.
78. CHANG, Peng, MEI, Hui, ZHOU, Shixiang, DASSIOS, Konstantinos G. and CHENG, Laifei. *3D printed electrochemical energy storage devices*. 2019.
79. FLECK, Trevor J., MURRAY, Allison K., GUNDUZ, I. Emre, SON, Steven F., CHIU, George T.C. and RHOADS, Jeffrey F. Additive manufacturing of multifunctional reactive materials. *Additive Manufacturing* [online]. 2017. Vol. 17, p. 176–182.
80. LEE, Chabum and TARBUTTON, Joshua A. Electric poling-assisted additive manufacturing process for PVDF polymer-based piezoelectric device applications. *Smart Materials and Structures*. 2014. Vol. 23, no. 9.
81. PORTER, Daniel A., HOANG, Trung V.T. and BERFIELD, Thomas A. Effects of in-situ poling and process parameters on fused filament fabrication printed PVDF sheet

mechanical and electrical properties. *Additive Manufacturing* [online]. 2017. Vol. 13, p. 81–92.

82. KIM, Hoejin, TORRES, Fernando, WU, Yanyu, VILLAGRAN, Dino, LIN, Yirong and TSENG, Tzu-Liang(Bill). Integrated 3D printing and corona poling process of PVDF piezoelectric films for pressure sensor application. *Smart Materials and Structures*. 2017.

83. CHANG, Chieh, TRAN, Van H., WANG, Junbo, FUH, Yiin Kuen and LIN, Liwei. Direct-write piezoelectric polymeric nanogenerator with high energy conversion efficiency. *Nano Letters*. 2010. Vol. 10, no. 2, p. 726–731.

84. CHEN, Zeyu, SONG, Xuan, LEI, Liwen, CHEN, Xiaoyang, FEI, Chunlong, CHIU, Chi Tat, QIAN, Xuejun, MA, Teng, YANG, Yang, SHUNG, Kirk, CHEN, Yong and ZHOU, Qifa. 3D printing of piezoelectric element for energy focusing and ultrasonic sensing. *Nano Energy*. 2016.

85. BENCOMO, Jose A., IACONO, Scott T. and MCCOLLUM, Jena. 3D printing multifunctional fluorinated nanocomposites: Tuning electroactivity, rheology and chemical reactivity. *Journal of Materials Chemistry A*. 2018. Vol. 6, no. 26, p. 12308–12315.

86. MOMENZADEH, Niknam, MIYANAJI, Hadi and BERFIELD, Thomas A. Influences of zirconium tungstate additives on characteristics of polyvinylidene fluoride (PVDF) components fabricated via material extrusion additive manufacturing process. *International Journal of Advanced Manufacturing Technology*. 2019. Vol. 103, no. 9–12, p. 4713–4720.

87. KAWAI, Heiji. The Piezoelectricity of Poly (vinylidene Fluoride). *Japanese Journal of Applied Physics*. 1969.

88. CELINA, Mathew, DARGAVILLE, Tim R., ASSINK, Roger A. and MARTIN, Jeffrey W. Selection and optimization of piezoelectric polyvinylidene fluoride polymers for adaptive optics in space environments. *High Performance Polymers*. 2005.

89. DUAN, X. H., WANG, H. Q., LI, Z. B., ZHU, L. K., CHEN, R., KONG, D. Y. and ZHAO, Z. Sound absorption of a flexible micro-perforated panel absorber based on PVDF piezoelectric film. *Applied Acoustics*. 2015.

90. WANG, Xiaomei, SUN, Fazhe, YIN, Guangchao, WANG, Yuting, LIU, Bo and DONG, Mingdong. *Tactile-sensing based on flexible PVDF nanofibers via electrospinning: A review*. 2018.

91. CHANG, Jiyoung, DOMMER, Michael, CHANG, Chieh and LIN, Liwei. *Piezoelectric nanofibers for energy scavenging applications*. 2012.

92. JONES, Gary D, ASSINK, Roger Alan, DARGAVILLE, Tim Richard, CHAPLYA, Pavel Mikhail, CLOUGH, Roger Lee, ELLIOTT, Julie M, MARTIN, Jeffrey W, MOWERY, Daniel Michael and CELINA, Mathew Christopher. Characterization, performance and optimization of PVDF as a piezoelectric film for advanced space mirror concepts. *Optimization* [online]. 2005. No. November.

93. LANG, S. B. and MUENSIT, S. *Review of some lesser-known applications of piezoelectric and pyroelectric polymers*. 2006.

94. MARTINS, P., LOPES, A. C. and LANCEROS-MENDEZ, S. Electroactive phases of poly(vinylidene fluoride): Determination, processing and applications. *Progress in Polymer Science* [online]. 2014. Vol. 39, no. 4, p. 683–706.

95. SATYANARAYANA, Kavitha Chelakara and BOLTON, Kim. Molecular dynamics simulations of α- To β-poly(vinylidene fluoride) phase change by stretching and poling. *Polymer*. 2012.

96. SATAPATHY, S., PAWAR, Santosh, GUPTA, P. K. and RVARMA, K. B. Effect of annealing on phase transition in poly(vinylidene fluoride) films prepared using polar solvent. *Bulletin of Materials Science*. 2011.

97. TARBUTTONA, Joshua, LEB, Tue, HELFRICHB, Greg and KIRKPATRICKB, Max. Phase Transformation and Shock Sensor Response of Additively Manufactured Piezoelectric PVDF. *Procedia Manufacturing* [online]. 2017. Vol. 10, p. 982–989. ISBN 1704687721

98. BODKHE, Sampada, TURCOT, Gabrielle, GOSSELIN, Frederick P. and THERRIAULT, Daniel. One-Step Solvent Evaporation-Assisted 3D Printing of Piezoelectric PVDF Nanocomposite Structures. *ACS Applied Materials and Interfaces*. 2017.

99. MAHADEVA, Suresha K., BERRING, John, WALUS, Konrad and STOEBER, Boris. Effect of poling time and grid voltage on phase transition and piezoelectricity of poly(vinyledene fluoride) thin films using corona poling. *Journal of Physics D: Applied Physics*. 2013. Vol. 46, no. 28.

100. KIM, Hoejin, TORRES, Fernando, WU, Yanyu, VILLAGRAN, Dino, LIN, Yirong and TSENG, Tzu-Liang(Bill). Integrated 3D printing and corona poling process of PVDF piezoelectric films for pressure sensor application. *Smart Materials and Structures* [online]. 2017. Vol. 26, no. 8, p. 085027.

101. DICKENS, B., BALIZER, E., DEREGGI, A. S. and ROTH, S. C. Hysteresis measurements of remanent polarization and coercive field in polymers. *Journal of Applied Physics*. 1992.

102. HUNDAHL, Jasbir S. and NATH, R. The piezoelectric effect and stored polarization in corona charged ABS films. *Journal of Physics D: Applied Physics*. 1998. Vol. 31, no. 5, p. 482–487.

103. RIBEIRO, P. A., BALOGH, D. T. and GIACOMETTI, J. A. Corona poling and electroactivity in a side-chain methacrylate copolymer. *IEEE Transactions on Dielectrics and Electrical Insulation*. 2000.

104. MONTERO, Michael, ROUNDY, Shad and ODELL, Dan. Material characterization of fused deposition modeling (FDM) ABS by designed experiments. *Proceedings of Rapid Prototyping & Manufacturing Conference* [online]. 2001. P. 1–21.

105. WANG, Che Chung, LIN, Ta Wei and HU, Shr Shiung. Optimizing the rapid prototyping process by integrating the Taguchi method with the Gray relational analysis. *Rapid Prototyping Journal*. 2007.

106. FATIMATUZAHRAA, A. W., FARAHAINA, B. and YUSOFF, W. A.Y. The effect of employing different raster orientations on the mechanical properties and microstructure of Fused Deposition Modeling parts. In : *ISBEIA 2011 - 2011 IEEE Symposium on Business, Engineering and Industrial Applications*. 2011.

107. CROCCOLO, Dario, DE AGOSTINIS, Massimiliano and OLMI, Giorgio. Experimental characterization and analytical modelling of the mechanical behaviour of fused deposition processed parts made of ABS-M30. *Computational Materials Science* [online]. 2013. Vol. 79, p. 506–518.

108. TORRES, Jonathan, COLE, Matthew, OWJI, Allen, DEMASTRY, Zachary and GORDON, Ali P. An approach for mechanical property optimization of fused deposition modeling with polylactic acid via design of experiments. *Rapid Prototyping Journal*. 2016. Vol. 22, no. 2, p. 387–404.

109. CHACÓN, J. M., CAMINERO, M. A., GARCÍA-PLAZA, E. and NÚÑEZ, P. J. Additive manufacturing of PLA structures using fused deposition modelling: Effect of process parameters on mechanical properties and their optimal selection. *Materials and Design* [online]. 2017. Vol. 124, p. 143–157.

110. LIU, Xinhua, ZHANG, Mingshan, LI, Shengpeng, SI, Lei, PENG, Junquan and HU, Yuan. Mechanical property parametric appraisal of fused deposition modeling parts based on the gray Taguchi method. *International Journal of Advanced Manufacturing Technology*.

2017.

111. MAHMOOD, Shahrain, QURESHI, A. J., GOH, Kheng Lim and TALAMONA, Didier. Tensile strength of partially filled FFF printed parts: Meta modelling. *Rapid Prototyping Journal*. 2017.

112. AW, Yah Yun, YEOH, Cheow Keat, IDRIS, Muhammad Asri, TEH, Pei Leng, HAMZAH, Khairul Amali and SAZALI, Shulizawati Aqzna. Effect of printing parameters on tensile, dynamic mechanical, and thermoelectric properties of FDM 3D printed CABS/ZnO composites. *Materials*. 2018. Vol. 11, no. 4.

113. KUNG, Chieh, KUAN, Hsu Chiang and KUAN, Chen Feng. Evaluation of tensile strength of 3D printed objects with FDM process on RepRap platform. In : *1st IEEE International Conference on Knowledge Innovation and Invention, ICKII 2018*. 2018.

114. DEY, Arup and YODO, Nita. *A systematic survey of FDM process parameter optimization and their influence on part characteristics*. 2019.

115. HERNANDEZ, R., SLAUGHTER, D., WHALEY, D., TATE, J. and ASIABANPOUR, B. Analyzing the tensile, compressive, and flexural properties of 3D printed ABS P430 plastic based on printing orientation using fused deposition modeling. *Solid Freeform Fabrication 2016: Proceedings of the 27th Annual International Solid Freeform Fabrication Symposium - An Additive Manufacturing Conference, SFF 2016*. 2016. P. 939–950.

116. PANDA, Samir Kumar, PADHEE, Saumyakant, SOOD, Anoop Kumar and MAHAPATRA, S. S. Optimization of Fused Deposition Modelling (FDM) Process Parameters Using Bacterial Foraging Technique. *Intelligent Information Management*. 2009. Vol. 01, no. 02, p. 89–97.

117. LUŽANIN, Ognjan, MOVRIN, Dejan and PLAN, Miroslav. Effect of Layer Thickness , Deposition Angle , and Infill on Maximum Flexural Force in Fdm-Built Specimens. [online]. 2014. Vol. 39, no. 1.

118. WU, Wenzheng, GENG, Peng, LI, Guiwei, ZHAO, Di, ZHANG, Haibo and ZHAO, Ji. Influence of layer thickness and raster angle on the mechanical properties of 3D-printed PEEK and a comparative mechanical study between PEEK and ABS. *Materials*. 2015. Vol. 8, no. 9, p. 5834–5846.

119. ABBAS, DrTahseenFadhil, MOHAMMAD OTHMAN, DrFarhad, BASIL ALI, Hind and AUTHOR, Corresponding. Effect of infill Parameter on compression property in FDM Process. *Int. Journal of Engineering Research andApplication www.ijera.com*. 2017.

120. FERNANDEZ-VICENTE, Miguel, CALLE, Wilson, FERRANDIZ, Santiago and CONEJERO, Andres. Effect of Infill Parameters on Tensile Mechanical Behavior in Desktop 3D Printing. *3D Printing and Additive Manufacturing*. 2016.

121. SOOD, Anoop Kumar, OHDAR, R. K. and MAHAPATRA, S. S. Parametric appraisal of mechanical property of fused deposition modelling processed parts. *Materials and Design*. 2010.

122. NUÑEZ, P. J., RIVAS, A., GARCÍA-PLAZA, E., BEAMUD, E. and SANZ-LOBERA, A. Dimensional and Surface Texture Characterization in Fused Deposition Modelling (FDM) with ABS plus. In : *Procedia Engineering*. 2015.

123. BAICH, Liseli, MANOGHARAN, Guha and MARIE, Hazel. Study of infill print design on production cost-time of 3D printed ABS parts. *International Journal of Rapid Manufacturing*. 2015. Vol. 5, no. 3/4, p. 308.

124. HARPOOL, Tanner David. Observing the Effects of Infill Shapes on the Tensile Characteristics of 3D Printed Plastic Parts. [online]. 2016. No. December, p. 88.

125. DUDESCU, Cristian and RACZ, Laszlo. Effects of Raster Orientation, Infill Rate and Infill Pattern on the Mechanical Properties of 3D Printed Materials. *ACTA Universitatis*

Cibiniensis. 2018. Vol. 69, no. 1, p. 23–30.

126. ABEYKOON, Chamil, SRI-AMPHORN, Pimpisut and FERNANDO, Anura. Optimization of fused deposition modeling parameters for improved PLA and ABS 3D printed structures. *International Journal of Lightweight Materials and Manufacture*. 2020.

127. TANVEER, Md. Qamar, HALEEM, Abid and SUHAIB, Mohd. Effect of variable infill density on mechanical behaviour of 3-D printed PLA specimen: an experimental investigation. *SN Applied Sciences*. 2019.

128. MISHRA, Pradeep Kumar, SENTHIL, P., ADARSH, S. and ANOOP, M.S. An investigation to study the combined effect of different infill pattern and infill density on the impact strength of 3D printed polylactic acid parts. *Composites Communications* [online]. 1 April 2021. Vol. 24, p. 100605.

129. GOPSILL, James A., SHINDLER, Jonathan and HICKS, Ben J. Using finite element analysis to influence the infill design of fused deposition modelled parts. *Progress in Additive Manufacturing*. 2018.

130. AKHOUNDI, B. and BEHRAVESH, A. H. Effect of Filling Pattern on the Tensile and Flexural Mechanical Properties of FDM 3D Printed Products. *Experimental Mechanics*. 2019. Vol. 59, no. 6, p. 883–897. ISBN 1134001800

131. MADAMESILA, Joseph, MCGEACHY, Philip, VILLARREAL BARAJAS, J. Eduardo and KHAN, Rao. Characterizing 3D printing in the fabrication of variable density phantoms for quality assurance of radiotherapy. *Physica Medica*. 2016.

132. PRASHANTH, Konda, SCUDINO, Sergio, CHATTERJEE, Riddhi, SALMAN, Omar and ECKERT, Jürgen. Additive Manufacturing: Reproducibility of Metallic Parts. *Technologies*. 2017.

133. ZHANG, Lai Chang, LIU, Yujing, LI, Shujun and HAO, Yulin. *Additive Manufacturing of Titanium Alloys by Electron Beam Melting: A Review*. 2018.

134. HERNÁNDEZ-NAVA, E., SMITH, C. J., DERGUTI, F., TAMMAS-WILLIAMS, S., LEONARD, F., WITHERS, P. J., TODD, I. and GOODALL, R. The effect of defects on the mechanical response of Ti-6Al-4V cubic lattice structures fabricated by electron beam melting. *Acta Materialia*. 2016.

135. WU, Y. C., KUO, C. N., SHIE, M. Y., SU, Y. L., WEI, L. J., CHEN, S. Y. and HUANG, J. C. Structural design and mechanical response of gradient porous Ti-6Al-4V fabricated by electron beam additive manufacturing. *Materials and Design*. 2018.

136. JETTÉ, Bruno, BRAILOVSKI, Vladimir, DUMAS, Mathieu, SIMONEAU, Charles and TERRIAULT, Patrick. Femoral stem incorporating a diamond cubic lattice structure: Design, manufacture and testing. *Journal of the Mechanical Behavior of Biomedical Materials*. 2018.

137. MURR, Lawrence E. and LI, Shujun. *Electron-beam additive manufacturing of high-temperature metals*. 2016.

138. VYATSKIKH, Andrey, KUDO, Akira, DELALANDE, Stéphane and GREER, Julia R. Additive manufacturing of polymer-derived titania for one-step solar water purification. *Materials Today Communications*. 2018.

139. CHENG, Lin, ZHANG, Pu, BIYIKLI, Emre, BAI, Jiaxi, PILZ, Steve and TO, Albert C. Integration of topology optimization with efficient design of additive manufactured cellular structures. In : *Proceedings - 26th Annual International Solid Freeform Fabrication Symposium - An Additive Manufacturing Conference, SFF 2015*. 2020.

140. VAIDYA, Rohan and ANAND, Sam. Optimum Support Structure Generation for Additive Manufacturing Using Unit Cell Structures and Support Removal Constraint. *Procedia Manufacturing*. 2016.

141. KENEL, Christoph, CASATI, Nicola P.M. and DUNAND, David C. 3D ink-

extrusion additive manufacturing of CoCrFeNi high-entropy alloy micro-lattices. *Nature Communications*. 2019.

142. SRIVATSAN, T. S., SUDARSHAN, T. S., MANIGANDAN, K., DING, Yaoyu, AKBARI, Meysam, GAO, Xin-Lin, AI, Li and KOVACEVIC, Radovan. Use of a Robotized Laser Powder-Feed Metal Additive Manufacturing System for Fabricating Metallic Metamaterials. In : *Manufacturing Techniques for Materials*. 2019.

143. RAI, Abha, HELMER, Harald and KÖRNER, Carolin. Simulation of grain structure evolution during powder bed based additive manufacturing. *Additive Manufacturing*. 2017.

144. DU, WEI, QIAN BAI, and Bi Zhang. A novel method for additive/subtractive hybrid manufacturing of metallic parts. *Procedia Manufacturing*. 2016. Vol. 5, p. 1018–1030.

145. GAYTAN, S. M., CADENA, M. A., KARIM, H., DELFIN, D., LIN, Y., ESPALIN, D., MACDONALD, E. and WICKER, R. B. Fabrication of barium titanate by binder jetting additive manufacturing technology. *Ceramics International*. 2015.

146. DALLAGO, M., FONTANARI, V., TORRESANI, E., LEONI, M., PEDERZOLLI, C., POTRICH, C. and BENEDETTI, M. Fatigue and biological properties of Ti-6Al-4V ELI cellular structures with variously arranged cubic cells made by selective laser melting. *Journal of the Mechanical Behavior of Biomedical Materials*. 2018.

147. LIVERANI, Erica, LUTEY, Adrian H.A., FORTUNATO, Alessandro and ASCARI, Alessandro. Characterization of lattice structures for additive manufacturing of lightweight mechanical components. In : *ASME 2017 12th International Manufacturing Science and Engineering Conference, MSEC 2017 collocated with the JSME/ASME 2017 6th International Conference on Materials and Processing*. 2017.

148. SHIVA, S., PALANI, I. A., PAUL, C. P., MISHRA, S. K. and SINGH, B. Investigations on phase transformation and mechanical characteristics of laser additive manufactured TiNiCu shape memory alloy structures. *Journal of Materials Processing Technology*. 2016.

149. VASILESCU, Mircea Dorin and FLESER, Traian. Influence of technological parametrs on the dimension of threaded parts generated with PLA matherial by FDM 3D printing. *Materiale Plastice*. 2018.

150. K. I. GIANNAKOPOULOS , V. D. SAGIAS, E. D. Pasiou and C. Stergiou. *COMPARATIVE STUDY OF PRINTING PATTERNS ON ADDITIVE MANUFACTURING*. Athens, 2020.

151. BAGHERI, Ali, BUJ-CORRAL, Irene, FERRER, Miquel, PASTOR, Maria Magdalena and ROURE, Francesc. Determination of the elasticity modulus of 3D printed octet-truss structures for use in porous prosthesis implants. *Materials*. 2018.

152. ALVAREZ, Kenny L.C., LAGOS, Rodrigo F.C. and AIZPUN, Miguel. Influence of infill parameter on the mechanical resistance in 3d printing, using the fused deposition modeling method. *Ingeniare. Revista chilena de ingeniería*. 2016.

153. POLONIO-ALCALÁ, Emma, RABIONET, Marc, GUERRA, Antonio J., YESTE, Marc, CIURANA, Joaquim and PUIG, Teresa. Screening of additive manufactured scaffolds designs for triple negative breast cancer 3D cell culture and stem-like expansion. *International Journal of Molecular Sciences*. 2018.

154. TSOUKNIDAS, A., PANTAZOPOULOS, M., KATSOULIS, I., FASNAKIS, D., MAROPOULOS, S. and MICHAILIDIS, N. Impact absorption capacity of 3D-printed components fabricated by fused deposition modelling. *Materials and Design*. 2016.

155. TALATAISONG, Wanvisa, ISMAEEL, Rand, MARQUES, Thiago H.R., ABOKHAMIS MOUSAVI, Seyedmohammad, BERESNA, Martynas, GOUVEIA, M. A., SANDOGHCHI, Seyed Reza, LEE, Timothy, CORDEIRO, Cristiano M.B. and

BRAMBILLA, Gilberto. Mid-IR Hollow-core microstructured fiber drawn from a 3D printed PETG preform. *Scientific Reports*. 2018.

156. HAMIDI, Armita and TADESSE, Yonas. Single step 3D printing of bioinspired structures via metal reinforced thermoplastic and highly stretchable elastomer. *Composite Structures*. 2019.

157. VIGNESHWARAN, K. and VENKATESHWARAN, N. Statistical analysis of mechanical properties of wood-PLA composites prepared via additive manufacturing. *International Journal of Polymer Analysis and Characterization*. 2019.

158. CLAUSEN, Anders, AAGE, Niels and SIGMUND, Ole. Exploiting Additive Manufacturing Infill in Topology Optimization for Improved Buckling Load. *Engineering*. 2016.

159. SUNNY, Sumair F., GLEASON, Glenn H. and MALIK, Arif S. Comparison of numerical methods for fluid-structure interaction simulation of fused deposition modeled nylon components. In : *Procedia Manufacturing*. 2019.

160. AL-KETAN, Oraib and ABU AL-RUB, Rashid K. *Multifunctional Mechanical Metamaterials Based on Triply Periodic Minimal Surface Lattices*. 2019.

161. SYCHOV, M. M., LEBEDEV, L. A., DYACHENKO, S. V. and NEFEDOVA, L. A. Mechanical properties of energy-absorbing structures with triply periodic minimal surface topology. *Acta Astronautica*. 2018.

162. YOO, Dong J. Porous scaffold design using the distance field and triply periodic minimal surface models. *Biomaterials*. 2011.

163. ABUEIDDA, Diab W., BAKIR, Mete, ABU AL-RUB, Rashid K., BERGSTRÖM, Jörgen S., SOBH, Nahil A. and JASIUK, Iwona. Mechanical properties of 3D printed polymeric cellular materials with triply periodic minimal surface architectures. *Materials and Design*. 2017.

164. YUAN, Li, DING, Songlin and WEN, Cuie. *Additive manufacturing technology for porous metal implant applications and triple minimal surface structures: A review*. 2019.

165. FEE, Conan. *3D-printed porous bed structures*. 2017.

166. YÁNEZ, A., CUADRADO, A., MARTEL, O., AFONSO, H. and MONOPOLI, D. Gyroid porous titanium structures: A versatile solution to be used as scaffolds in bone defect reconstruction. *Materials and Design*. 2018.

167. LI, Dawei, LIAO, Wenhe, DAI, Ning, DONG, Guoying, TANG, Yunlong and XIE, Yi Min. Optimal design and modeling of gyroid-based functionally graded cellular structures for additive manufacturing. *CAD Computer Aided Design*. 2018.

168. SPEIRS, M., VAN HOOREWEDER, B., VAN HUMBEECK, J. and KRUTH, J. P. Fatigue behaviour of NiTi shape memory alloy scaffolds produced by SLM, a unit cell design comparison. *Journal of the Mechanical Behavior of Biomedical Materials*. 2017.

169. BOBBERT, F. S.L., LIETAERT, K., EFTEKHARI, A. A., POURAN, B., AHMADI, S. M., WEINANS, H. and ZADPOOR, A. A. Additively manufactured metallic porous biomaterials based on minimal surfaces: A unique combination of topological, mechanical, and mass transport properties. *Acta Biomaterialia*. 2017.

170. NGUYEN, Ban Dang, HAN, Seung Chul, JUNG, Yoon Chang and KANG, Kiju. Design of the P-surfaced shellular, an ultra-low density material with micro-architecture. *Computational Materials Science*. 2017.

171. ATAEE, Arash, LI, Yuncang, BRANDT, Milan and WEN, Cuie. Ultrahigh-strength titanium gyroid scaffolds manufactured by selective laser melting (SLM) for bone implant applications. *Acta Materialia*. 2018.

172. YAN, Chunze, HAO, Liang, HUSSEIN, Ahmed and YOUNG, Philippe. Ti-6Al-4V triply periodic minimal surface structures for bone implants fabricated via selective laser

melting. *Journal of the Mechanical Behavior of Biomedical Materials*. 2015.

173. RAJAGOPALAN, Srinivasan and ROBB, Richard A. Schwarz meets Schwann: Design and fabrication of biomorphic and durataxic tissue engineering scaffolds. *Medical Image Analysis*. 2006.

174. FEMMER, Tim, KUEHNE, Alexander J.C. and WESSLING, Matthias. Estimation of the structure dependent performance of 3-D rapid prototyped membranes. *Chemical Engineering Journal*. 2015.

175. YOO, Dong Jin and KIM, Kwang Hyuk. An advanced multi-morphology porous scaffold design method using volumetric distance field and beta growth function. *International Journal of Precision Engineering and Manufacturing*. 2015.

176. YAN, Chunze, HAO, Liang, HUSSEIN, Ahmed and RAYMONT, David. Evaluations of cellular lattice structures manufactured using selective laser melting. *International Journal of Machine Tools and Manufacture*. 2012.

177. AFSHAR, M., ANARAKI, A. Pourkamali, MONTAZERIAN, H. and KADKHODAPOUR, J. Additive manufacturing and mechanical characterization of graded porosity scaffolds designed based on triply periodic minimal surface architectures. *Journal of the Mechanical Behavior of Biomedical Materials*. 2016.

178. MONTAZERIAN, H., DAVOODI, E., ASADI-EYDIVAND, M., KADKHODAPOUR, J. and SOLATI-HASHJIN, M. Porous scaffold internal architecture design based on minimal surfaces: A compromise between permeability and elastic properties. *Materials and Design*. 2017.

179. ABUEIDDA, Diab W., DALAQ, Ahmed S., ABU AL-RUB, Rashid K. and YOUNES, Hammad A. Finite element predictions of effective multifunctional properties of interpenetrating phase composites with novel triply periodic solid shell architectured reinforcements. *International Journal of Mechanical Sciences*. 2015.

180. WANG, Lifeng, LAU, Jacky, THOMAS, Edwin L. and BOYCE, Mary C. Co-continuous composite materials for stiffness, strength, and energy dissipation. *Advanced Materials*. 2011.

181. KAPFER, Sebastian C., HYDE, Stephen T., MECKE, Klaus, ARNS, Christoph H. and SCHRÖDER-TURK, Gerd E. Minimal surface scaffold designs for tissue engineering. *Biomaterials*. 2011.

182. ABUEIDDA, Diab W., ABU AL-RUB, Rashid K., DALAQ, Ahmed S., LEE, Dong Wook, KHAN, Kamran A. and JASIUK, Iwona. Effective conductivities and elastic moduli of novel foams with triply periodic minimal surfaces. *Mechanics of Materials*. 2016.

183. SCHOEN, Alan H. Reflections concerning triply-periodic minimal surfaces. *Interface Focus*. 2012.

184. SCHOEN, Alan H. Infinite periodic minimal surfaces without self-intersections. *Nasa Technical Note D-5541*. 1970.

185. AL-KETAN, Oraib, ROWSHAN, Reza and ABU AL-RUB, Rashid K. Topology-mechanical property relationship of 3D printed strut, skeletal, and sheet based periodic metallic cellular materials. *Additive Manufacturing*. 2018.

186. CHEN, Hao, HAN, Qing, WANG, Chenyu, LIU, Yang, CHEN, Bingpeng and WANG, Jincheng. Porous Scaffold Design for Additive Manufacturing in Orthopedics: A Review. *Frontiers in Bioengineering and Biotechnology*. 2020. Vol. 8, no. June, p. 1–20.

187. BARBA, D., ALABORT, E. and REED, R. C. Synthetic bone: Design by additive manufacturing. *Acta Biomaterialia*. 2019.

188. SHI, Jianping, ZHU, Liya, LI, Lan, LI, Zongan, YANG, Jiquan and WANG, Xingsong. A TPMS-based method for modeling porous scaffolds for bionic bone tissue engineering. *Scientific Reports*. 2018.

189. YANG, Lei, MERTENS, Raya, FERRUCCI, Massimiliano, YAN, Chunze, SHI, Yusheng and YANG, Shoufeng. Continuous graded Gyroid cellular structures fabricated by selective laser melting: Design, manufacturing and mechanical properties. *Materials and Design*. 2019.

190. CASTRO, A. P.G., RUBEN, R. B., GONÇALVES, S. B., PINHEIRO, J., GUEDES, J. M. and FERNANDES, P. R. Numerical and experimental evaluation of TPMS Gyroid scaffolds for bone tissue engineering. *Computer Methods in Biomechanics and Biomedical Engineering*. 2019.

191. SORO, Nicolas, ATTAR, Hooyar, WU, Xinhua and DARGUSCH, Matthew S. Investigation of the structure and mechanical properties of additively manufactured Ti-6Al-4V biomedical scaffolds designed with a Schwartz primitive unit-cell. *Materials Science and Engineering A* [online]. 2019. Vol. 745, no. November 2018, p. 195–202.

192. AMEDURI, Bruno. From vinylidene fluoride (VDF) to the applications of VDF-Containing polymers and copolymers: Recent developments and future trends. *Chemical Reviews*. 2009. Vol. 109, no. 12, p. 6632–6686.

193. RYAN, John, DIZON, C, ESPERA, Alejandro H, CHEN, Qiyi and ADVINCULA, Rigoberto C. Mechanical characterization of 3D-printed polymers. . 2018. Vol. 20, p. 44–67.

194. ASTM-D638-14. Standard Test Method for Tensile Properties of Plastics. *ASTM Standards*. 2014. ISBN 0521298466

195. ISO. *ISO 527:2012 Plastics — Determination of tensile properties*. 2006.

196. ASTM D790. Standard Test Method for Flexural Properties of Unreinforced and Reinforced Plastics and Electrical Insulation Materials. *ASTM Standards*. 2015.

197. INTERNATIONAL STANDARDS ORGANIZATION. *ISO 178:2011 - Plastics - Determination of flexural properties*. 2011.

198. ISO. ISO 604:2002 Plastics — Determination of compressive properties. *ISO*. 2002.

199. ASTM STANDARD D695-15. Standard Test Method for Compressive Properties of Rigid Plastics. *ASTM International, West Conshohocken, PA*. 2015. ISBN 5969111007

200. MULLAVEETTIL, Farusil Najeeb, DAUKSEVICIUS, Rolanas, RIMASAUSKAS, Marius and GRIGALIUNAS, Valdas. Fused filament fabrication and mechanical performance of PVDF-based specialty thermoplastics. *International Journal of Advanced Manufacturing Technology*. 2021. P. 3267–3280.

201. PUGALENDHI, Arivazhagan, RANGANATHAN, Rajesh and CHANDRASEKARAN, Manivannan. Effect of process parameters on mechanical properties of VeroBlue material and their optimal selection in PolyJet technology. *The International Journal of Advanced Manufacturing Technology* [online]. 2020. Vol. 108, no. 4, p. 1049–1059.

202. GOH, G. D., YAP, Y. L., TAN, H. K.J., SING, S. L., GOH, G. L. and YEONG, W. Y. Process–Structure–Properties in Polymer Additive Manufacturing via Material Extrusion: A Review. *Critical Reviews in Solid State and Materials Sciences*. 2020. Vol. 45, no. 2, p. 113–133.

203. WANG, Tian Ming, XI, Jun Tong and JIN, Ye. A model research for prototype warp deformation in the FDM process. *International Journal of Advanced Manufacturing Technology*. 2007.

204. ALSOUFI, Mohammad S. and ELSAYED, Abdulrhman E. Warping deformation of desktop 3D printed parts manufactured by open source fused deposition modeling (FDM) system. *International Journal of Mechanical and Mechatronics Engineering*. 2017. Vol. 17, no. 4, p. 7–16.

205. NILE. PVDF Product Information. 2020.

206. KAČERGIS, Lukas, MITKUS, Rytis and SINAPIUS, Michael. Influence of fused

deposition modeling process parameters on the transformation of 4D printed morphing structures. *Smart Materials and Structures*. 2019. Vol. 28, no. 10.

207. VAN MANEN, Teunis, JANBAZ, Shahram and ZADPOOR, Amir A. Programming the shape-shifting of flat soft matter. *Materials Today* [online]. 2018. Vol. 21, no. 2, p. 144–163.

208. SUNG, Jaebum and SO, Hongyun. 3D printing-assisted fabrication of microgrid patterns for flexible antiadhesive polymer surfaces. *Surfaces and Interfaces*. 1 April 2021. Vol. 23, p. 100935.

209. ILYÉS, Kinga, KOVÁCS, Norbert Krisztián, BALOGH, Attila, BORBÁS, Enikő, FARKAS, Balázs, CASIAN, Tibor, MAROSI, György, TOMUȚĂ, Ioan and NAGY, Zsombor Kristóf. The applicability of pharmaceutical polymeric blends for the fused deposition modelling (FDM) 3D technique: Material considerations–printability–process modulation, with consecutive effects on in vitro release, stability and degradation. *European Journal of Pharmaceutical Sciences*. 1 March 2019. Vol. 129, p. 110–123.

210. SANTOS MACÍAS, Juan Guillermo, DOUILLARD, Thierry, ZHAO, Lv, MAIRE, Eric, PYKA, Grzegorz and SIMAR, Aude. Influence on microstructure, strength and ductility of build platform temperature during laser powder bed fusion of AlSi10Mg. *Acta Materialia*. 1 December 2020. Vol. 201, p. 231–243.

211. HARPREET SHARDA, Ashish Kumar. A View on Why Infill Ratio and Infill Type is the Backbone of the Strength of 3D Printing Models in Affordable Printing. *IJSRD - International Journal for Scientific Research & Development*. 2019.

212. ARIZA GOMEZ, Aynor J., CONTRERAS, Maria Marjorie, VAZ, Murilo Augusto, COSTA, Celio A. and COSTA, Marysilvia F. Temperature-time large strain mechanical model for Poly(vinylidene fluoride). *Polymer Testing*. 2020.

213. CHALLIER, Mélanie, BESSON, Jacques, LAIARINANDRASANA, Lucien and PIQUES, Roland. Damage and fracture of polyvinylidene fluoride (PVDF) at 20 °C: Experiments and modelling. *Engineering Fracture Mechanics*. 2006.

214. LAIARINANDRASANA, L., BESSON, J., LAFARGE, M. and HOCHSTETTER, G. Temperature dependent mechanical behaviour of PVDF: Experiments and numerical modelling. *International Journal of Plasticity*. 2009.

215. ARIZA GOMEZ, Aynor J., CONTRERAS, Maria Marjorie, VAZ, Murilo Augusto, COSTA, Celio A. and COSTA, Marysilvia F. Temperature-time large strain mechanical model for Poly(vinylidene fluoride). *Polymer Testing* [online]. 2020. Vol. 82, no. December 2019, p. 106312.

216. REIS, J. M.L., MOTTA, E. P. and DA COSTA MATTOS, H. S. Elasto-viscoplastic behaviour of a polyvinylidene fluoride (PVDF) in tension. *Polymer Testing*. 2015.

217. ARIZA GOMEZ, Aynor J., CONTRERAS, Maria Marjorie, VAZ, Murilo Augusto, COSTA, Celio A. and COSTA, Marysilvia F. Temperature-time large strain mechanical model for Poly(vinylidene fluoride). *Polymer Testing*. 2020. Vol. 82, no. December 2019, p. 106312.

218. WU, H., FAHY, W. P., KIM, S., KIM, H., ZHAO, N., PILATO, L., KAFI, A., BATEMAN, S. and KOO, J. H. *Recent developments in polymers/polymer nanocomposites for additive manufacturing*. 1 June 2020. Elsevier Ltd.

219. FONTANANOVA, E., BAHATTAB, M. A., ALJLIL, S. A., ALOWAIRDY, M., RINALDI, G., VUONO, D., NAGY, J. B., DRIOLI, E. and DI PROFIO, G. From hydrophobic to hydrophilic polyvinylidenefluoride (PVDF) membranes by gaining new insight into material's properties. *RSC Advances*. 2015.

220. COSTA, P., NUNES-PEREIRA, J., OLIVEIRA, J., SILVA, J., MOREIRA, J. Agostinho, CARABINEIRO, S. A.C., BUIJNSTERS, J. G. and LANCEROS-MENDEZ, S.

High-performance graphene-based carbon nanofiller/polymer composites for piezoresistive sensor applications. *Composites Science and Technology*. 2017. Vol. 153, no. January 2018, p. 241–252.

221. SIERADZKA, Marta, FRYCZKOWSKI, Ryszard, BINIAŚ, Dorota, BINIAŚ, Włodzimierz and JANICKI, Jarosław. A facile approach to obtaining PVDF/graphene fibers and the effect of nanoadditive on the structure and properties of nanocomposites. *Polymer Testing*. 2020. Vol. 81, no. July 2019.

222. BRUGGI, Matteo and TALIERCIO, Alberto. Hierarchical Infills for Additive Manufacturing Through a Multiscale Approach. *Journal of Optimization Theory and Applications*. 2020.

223. DONATO, Gustavo Henrique Bolognesi and BIANCHI, Marcos. Pressure dependent yield criteria applied for improving design practices and integrity assessments against yielding of engineering polymers. *Journal of Materials Research and Technology* [online]. 2012. Vol. 1, no. 1, p. 2–7.

224. A.E, Tontowi, L, Ramdani, R.V, Erdizon and D.K, Baroroh. Optimization of 3D-Printer Process Parameters for Improving Quality of Polylactic Acid Printed Part. *International Journal of Engineering and Technology*. 2017. Vol. 9, no. 2, p. 589–600.

225. ZIEMIAN, Constance, SHARMA, Mala and ZIEMI, Sophia. Anisotropic Mechanical Properties of ABS Parts Fabricated by Fused Deposition Modelling. In : *Mechanical Engineering*. 2012.

226. SPOERK, Martin, HOLZER, Clemens and GONZALEZ-GUTIERREZ, Joamin. *Material extrusion-based additive manufacturing of polypropylene: A review on how to improve dimensional inaccuracy and warpage*. 2020.

227. KHOGALIA, Elfaroug Hosham, CHOO, Hui Leng and YAP, Wei Hsum. Performance of triply periodic minimal surface lattice structures under compressive loading for tissue engineering applications. In : *AIP Conference Proceedings*. 2020.

228. MULLAVEETTIL, Farusil Najeeb, DAUKSEVICIUS, Rolanas and WAKJIRA, Yosef. Strength and elastic properties of 3D printed PVDF-based parts for lightweight biomedical applications. *Journal of the Mechanical Behavior of Biomedical Materials*. 2021. Vol. 120, May.

LIST OF AUTHOR'S PUBLICATIONS

ARTICLES IN PEER-REVIEWED SCIENTIFIC PUBLICATIONS

Indexed in the Web of Science with Impact Factor
International Publishers

1. Mullaveettil, Farusil Najeeb; Daukševičius, Rolanas; Rimašauskas, Marius; Grigaliūnas, Valdas. Fused filament fabrication and mechanical performance of PVDF-based specialty thermoplastics // International journal of advanced manufacturing technology. London: Springer. ISSN 0268-3768. eISSN 1433-3015. 2021, vol. 117, iss. 11-12, p. 3267-3280. DOI: 10.1007/s00170-021-07887-6. [Science Citation Index Expanded (Web of Science); Scopus] [IF: 3,226; AIF: 4,609; IF/AIF: 0,699; Q2 (2020, InCites JCR SCIE)] [FOR: T 009] [Input: 0,350].
2. Mullaveettil, Farusil Najeeb; Daukševičius, Rolanas; Wakjira, Yosef. Strength and elastic properties of 3D printed PVDF-based parts for lightweight biomedical applications // Journal of the mechanical behavior of biomedical materials. Amsterdam: Elsevier. ISSN 1751-6161. eISSN 1878-0180. 2021, vol. 120, art. no. 104603, p. 1-10. DOI: 10.1016/j.jmbbm.2021.104603. [Science Citation Index Expanded (Web of Science); Scopus; MEDLINE] [IF: 3,902; AIF: 5,315; IF/AIF: 0,734; Q2 (2020, InCites JCR SCIE)] [FOR: T 009] [Input: 0,450].

In peer-reviewed conference proceedings
National Publishers

1. Mullaveettil, Farusil Najeeb; Daukševičius, Rolanas; Rimašauskas, Marius; Grigaliūnas, Valdas; Griškevičius, Paulius. Development of electroactive PVDF films by using 3D printing and contact poling // Mechanika 2018: proceedings of the 23rd international scientific conference, 18 May 2018, Kaunas University of Technology, Lithuania / Kaunas University of Technology, Lithuanian Academy of Science, IFTOMM National Committee of Lithuania, Baltic Association of Mechanical Engineering. Kaunas: Kaunas University of Technology. ISSN 1822-2951. 2018, p. 113-117. [FOR: T 009] [Input: 0,200].
2. Mullaveettil, Farusil Najeeb; Daukševičius, Rolanas. Finite element modeling of cantilever-type transducer based on ionic electroactive polymer // Mechanika 2017: proceedings of the 22nd international scientific conference, 19 May 2017, Kaunas University of Technology, Lithuania / Kaunas University of Technology, Lithuanian Academy of Science, IFTOMM National Committee of Lithuania, Baltic Association of Mechanical Engineering. Kaunas: Kaunas University of Technology. ISSN 1822-2951. 2017, p. 276-280. [FOR: T 009] [Input: 0,500].

PRESENTATION OF RESEARCH RESULTS AT CONFERENCES
Other conference abstracts and non-peer reviewed conference papers

1. Mullaveettil, Farusil Najeeb; Dauksevicius, Rolanas. FDM printing of bioinspired triply periodic minimal surfaces based PVDF material for scaffold development in biomedical application // ICPTM 2020: international conference on 3D printing technologies and materials, Amsterdam, the Netherlands, November 5-6, 2020. Canakkale : WASET. 2020, p. 1. [FOR: T 009].

SL344. 2021-12-03, 12,5, leidyb. apsk. l. Tiražas 14 egz. Užsakymas 289.
Išleido Kauno technologijos universitetas, K. Donelaičio g. 73, 44249 Kaunas
Spausdino leidyklos „Technologija“ spaustuvė, Studentų g. 54, 51424 Kaunas